

Study on characteristics of liquid film in upward annular two-phase flow

張, 華誠

<https://hdl.handle.net/2324/7157347>

出版情報 : Kyushu University, 2023, 博士 (工学), 課程博士
バージョン :
権利関係 :



Study on characteristics of liquid film in upward annular two-phase flow

By

Huacheng, Zhang

Thesis submitted to Kyushu University for the degree of Doctor of Philosophy

Examiner: Prof. Shoji Mori

Co-examiner: Prof. Yasuyuki Takata

Prof. Satoshi Watanabe

Graduate School of Engineering

Kyushu University

Fukuoka, JAPAN

June 2023

Contents

Contents	I
List of figures	IV
List of tables	VIII
Nomenclature	IX
CHAPTER 1	1
Introduction	1
1.1 Role of annular flow in practical applications.....	1
1.2 Previous studies in annular flow	3
1.3 Current status and objectives of this study	7
1.4 Structure of the thesis	9
References	10
CHAPTER 2	15
Effect of density ratio and surface tension on liquid film thickness and disturbance wave height ...	15
2.1 Introduction	15
2.2 Experimental apparatus and procedures.....	17
2.2.1 Working fluids.....	17
2.2.2 Experimental apparatus.....	17
2.2.3 Test section.....	19
2.2.4 Film thickness measurement methods and measurement accuracy	20
2.2.5 Experimental conditions	22
2.2.6 Film thickness data processing	24
2.2.7 Uncertainty analysis.....	25
2.3 Results and discussion.....	25
2.3.1 Film thickness	25
2.3.2 Disturbance wave height.....	37

2.3.3 Comparison of the current model with previous databases	41
2.4 Conclusions	42
References	44
CHAPTER 3	48
Effect of density ratio and surface tension on characteristics of disturbance waves	48
3.1 Introduction	48
3.2 Experimental apparatus and procedures	50
3.3 Results and discussion	51
3.3.1 Wave velocity	51
3.3.2 Wavelength, wave pitch and intermittency	59
3.3.3 Wave frequency	65
3.4 Conclusion	71
References	72
CHAPTER 4	77
Effect of density ratio and surface tension on interfacial shear stress and pressure drop	77
4.1 Introduction	77
4.2 Experimental apparatus and procedures	78
4.3 Results and discussion	79
4.3.1 Pressure gradient and interfacial shear stress	79
4.3.2 Interfacial friction factor	82
4.3.3 Pressure drop prediction	89
4.4 Conclusion	92
References	94
CHAPTER 5	97
Summary and prospect	97
5.1 Summary	97
5.2 Prospect	99
References	101

Acknowledgement 102

Appendix A. Circuit design of film thickness measurement sensor 104

Appendix B. Preparation of working fluids 105

Appendix C. Dynamic performance of the film thickness measurement sensors 105

List of figures

Fig. 1.1	Flow patterns of gas-liquid two-phase flow in a vertical tube.	1
Fig. 1.2	Schematic illustration of annular flow.	2
Fig. 1.3	Simplified scheme of plant with boiling water reactor.	3
Fig. 1.4	Schematic illustration of liquid film configuration.	5
Fig. 2.1	Schematic illustration of the experimental facility.	18
Fig. 2.2	Schematic illustration of the test section.	19
Fig. 2.3	Cross-sectional view of the test section when filled with working liquid and (a) PTFE Rod and (b) working gas.	21
Fig. 2.4	Fig. 2.1 Static calibration by nonconductive rods.	21
Fig. 2.5	Test matrix represented on the (a) Hewitt–Roberts flow map and (b) Mishima–Ishii flow map.	22
Fig. 2.6	Snapshots of annular flow of Nitrogen–Water system under the pressure 0.2 MPa in the 5.0 mm inner diameter tube.	23
Fig. 2.7	The probability density function of film thickness when $j_L = 0.1$ m/s, $j_G = 18.6$ m/s with a density ratio of 434.	24
Fig. 2.8	Measurement of film thickness over time and the schematic illustration of the corresponding t_{Fbase} , t_{Fave} , and t_{Fmax} .	26
Fig. 2.9	Comparison of average film thickness under different experimental conditions when plotted against (a) j_G , (b) Re_G , (c) We_G ; the figures on the left side and right side correspond to the $j_L = 0.1$ and 0.8 m/s, respectively.	27
Fig. 2.10	Fig. 2.2 The comparison of normalized predicted average film thickness corresponding to the C_{fi} from the correlation of (a) Wallis, (b) Ju, and (c) Belt.	30
Fig. 2.11	Comparison of normalized measured average film thickness from different databases with normalized predicted average film thickness obtained from Eq. (2.24).	32
Fig. 2.12	Film thickness measurement results under the superficial liquid velocity of (a) 0.1, (b) 0.4, and (c) 0.8 m/s.	34

Fig. 2.13	Comparison of film thickness time trace under a superficial liquid velocity of 0.1 m/s and density ratios of 434 and 32 with the gas Weber numbers of 55, 275, 470, and 900.	36
Fig. 2.14	Disturbance wave height measurement results under the superficial liquid velocity of (a) 0.1, (b) 0.4, and (c) 0.8 m/s.	37
Fig. 2.15	Schematic illustration of force balance on disturbance wave.	38
Fig. 2.16	Effect of liquid Weber number and gas Weber number on wave height for different density ratios and superficial liquid velocity.	40
Fig. 2.17	Comparison of measured wave height with predicted wave height.	40
Fig. 2.18	Effect of liquid and gas Weber numbers on normalized wave height from different databases for different density ratios and superficial liquid velocity.	41
Fig. 2.19	Comparison of normalized measured wave height from different databases with normalized predicted wave height.	42
Fig. 3.1	Disturbance wave velocity at the superficial liquid velocities of (a) 0.1, (b) 0.4, and (c) 0.8 m/s.	51
Fig. 3.2	Schematic of wall and interfacial shear stresses acting on the liquid film.	54
Fig. 3.3	Comparison of the normalized measured average film thickness with the friction factor ratio C_{fw}/C_{fi} .	54
Fig. 3.4	Comparison of the measured wave velocity with the predicted wave velocity.	55
Fig. 3.5	Comparison of the measured wave velocity with the predicted wave velocity when previous databases were employed.	55
Fig.3.6	Comparison of measured wave velocities from the database of the current experiments of [35], [36], and [37] and with wave velocity predicted by the correlations of (a) Eqs. (3.3) and (3.5); (b) [38]; (c) [39]; (d) [25]; (e) [29]; and (f) [34].	57
Fig.3.7	Schematic illustration of the disturbance wave characteristics	59
Fig. 3.8	Wave pitch at the superficial liquid velocities of (a) 0.1, (b) 0.4, and (c) 0.8 m/s.	60
Fig. 3.9	Comparison of wave pitch with the disturbance wave height.	61

Fig. 3.10	Comparison of the ratio of wave pitch with $\rho_G/\rho_L \cdot Re_L/Re_G$.	61
Fig. 3.11	Comparison of measured L/H with predicted L/H from Eq. (3.8).	62
Fig. 3.12	Disturbance wave wavelength under the superficial liquid velocity of (a) 0.1, (b) 0.4, and (c) 0.8 m/s.	63
Fig. 3.13	Disturbance wave intermittency under the superficial liquid velocity of (a) 0.1, (b) 0.4, and (c) 0.8 m/s.	64
Fig. 3.14	Wave Comparison of the ratio of wave intermittency with average film thickness.	64
Fig. 3.15	Time trace of the measured film thickness for the water–nitrogen system at different j_L and j_G . The identified disturbance wave is indicated with the red circle.	65
Fig. 3.16	Disturbance wave frequency at the superficial liquid velocities of (a) 0.1, (b) 0.4, and (c) 0.8 m/s.	66
Fig. 3.17	Comparison of liquid Strouhal number with Lockhart–Martinelli parameter.	67
Fig. 3.18	Comparison of the measured Strouhal number from the databases of the current experiments of [35], [51], [49], [48], [37], and [50] with the wave velocity predicted by the correlations of (a) the present work, (b) [48], (c) [35], (d)[45], (e) [38], and (f)[47].	68
Fig.4.1	Schematic of the test section.	79
Fig. 4.2	Measured pressure gradient over 0.5 m.	80
Fig. 4.3	4.3. Comparison of the interfacial shear stress calculated by Eqs. (4.1) and (4.4).	81
Fig. 4.4	Interfacial shear stress calculated by Eq. (4.4).	82
Fig. 4.5	Comparison between Re_G and (a) H/D , and (b) C_{fi} .	83
Fig. 4.6	Comparison between k_S/D and (a) H/D ; (b) t_{Fave}/D	85
Fig. 4.7	Comparison between C_{fi} and (a) H/D ; (b) t_{Fave}/D .	86
Fig. 4.8	Comparison of measured and predicted interfacial friction factor by correlations of (a) present work; (b) Moeck [2]; (c) Fore et al. [4]; (d) Ju et al. [5]; (e) Belt et al. [8]; (f) Henstock and Hanratty [9].	88
Fig. 4.9	Comparison of measured and predicted pressure gradient by correlations of (a) present work; (b) Cicchitti [30]; (c) Awad and	91

Muzychka [31]; (d) Sun and Mishima [34]; (e) Kim and Mudwar [35].

Fig. A1	Circuit diagram of each sensor.	104
Fig. C1	Schematic illustration of printed calibration rod with dimensional information.	106
Fig. C2	Schematic illustration of printed calibration rod with dimensional information.	106

List of tables

Table 1.1	Summary of properties for working fluids of Steam–Water under BWR operating condition and Air–Water under low atmospheric pressure and room temperature	8
Table 1.2	Summary of properties for working fluids in current experiments	8
Table 2.1	Summary of experimental conditions of the databases employed in this study.	32
Table 3.1	Summary of the experimental conditions of the employed databases.	56
Table 3.2	Previous models of wave velocity.	57
Table 3.3	Summary of the experimental conditions of the databases employed.	69
Table 3.4	Previous models of wave frequency.	70
Table 4.1	Summary of the experimental conditions of the employed databases.	86
Table 4.2	Previous models of interfacial friction factor.	87
Table 4.3	Previous correlations for predicting two-phase pressure drop.	90

Nomenclature

Latin letters

<i>BWR</i>	boiling water reactor
<i>C</i>	Chisholm parameter
C_f	friction factor
<i>D</i>	tube diameter
<i>G</i>	mass flux
<i>E</i>	entrainment rate
<i>f</i>	wave frequency
<i>g</i>	acceleration due to gravity
<i>H</i>	wave height
<i>I</i>	electric current
<i>INT</i>	intermittency
<i>j</i>	volumetric flux
k_S	equivalent sand-grain roughness
<i>L</i>	wave pitch
N_μ	viscosity number
<i>P</i>	pressure
<i>R</i>	electrical resistance
R_D	deposition rate
<i>Re</i>	Reynolds number
<i>S</i>	sensor
<i>Sr</i>	Strouhal number
t_F	film thickness
<i>u</i>	velocity
<i>V</i>	voltage
<i>v</i>	velocity
<i>We</i>	Weber number
<i>X</i>	Lockhart-Martinelli parameter. Lockhart-Martinelli multiplied.

Greek symbols

α_d	droplet volume fraction
λ	wavelength
μ	dynamic viscosity
ρ	density; electrical conductivity
σ	surface tension
τ	shear stress
Φ	two-phase frictional multiplier

Subscripts

<i>ave</i>	average value
<i>base</i>	base film
<i>c</i>	calibration; core
<i>G</i>	gas phase
<i>i</i>	interface
<i>L</i>	liquid phase
<i>max</i>	maximum value
<i>s</i>	single-phase
<i>TP</i>	two-phase
<i>w</i>	tube wall; disturbance wave

CHAPTER 1

Introduction

1.1 Role of annular flow in practical applications

Gas-liquid annular flow is one of the two-phase flow regimes together with bubble flow, slug flow, and churn flow as shown in Fig. 1.1. It occurs in various industrial equipment, such as nuclear reactors, heat exchangers, pipelines, and steam boilers and many other gas-liquid interacting applications [1–4]. In the regime of annular flow, as shown in Fig. 1.2, a continuously flowing gas core locates in the center and is surrounded by a liquid film attaching to the tube wall. Intermittent disturbance waves exist at the gas–liquid interface and large amount of liquid are transferred by the disturbance waves [5]. Meanwhile, the ripples on top of disturbance waves are sheared by the gas stream, which leads to the creation of droplets entrained in the gas core [6,7]. The entrained droplets may deposit back to the liquid film. Because the thin liquid film between two successive disturbance waves leads to the dryout on the heating surface and limits the performance of the heating components, complete knowledge of the characteristics of annular flow is of great significance for the industries [5,8].

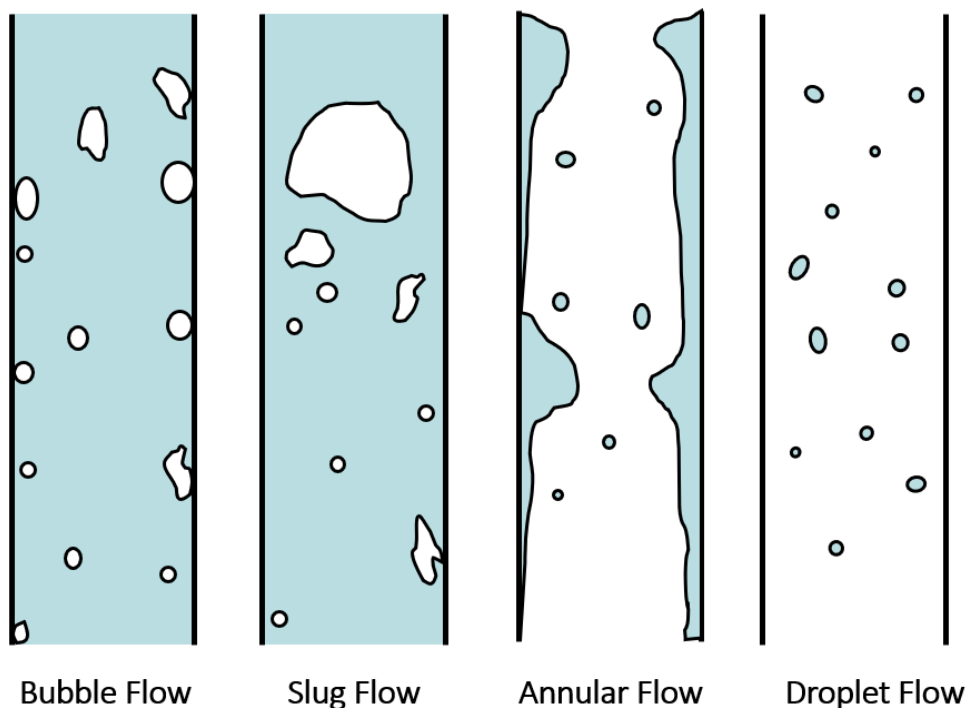


Fig. 1.1 Flow patterns of gas-liquid two-phase flow in a vertical tube

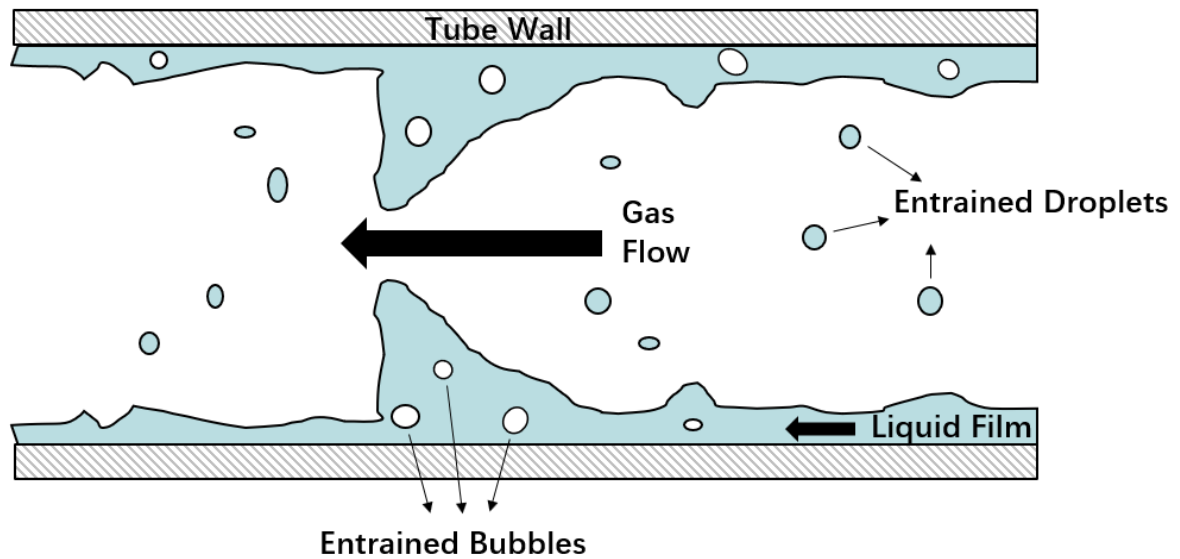


Fig. 1.2 Schematic illustration of annular flow

In the heat transfer applications, particularly in systems such as Boiling Water Reactors (BWRs) as shown in Fig. 1.3, annular flow plays a critical role. In the BWR vessel, heat is generated in fuel rods as a result of nuclear fission. Water is supplied to cool down the fuel rods and generate steam that spins turbines to get electricity. To guarantee adequate cooling of the fuel rods, they must be permanently covered with a liquid film. If liquid film along the fuel rods dries out, the heat transferred to the water will be reduced and the fuel rods will keep being heated up. The fuel rods quickly become so hot that it burns through the surface and the vessel floor, causing radiation release. This is the direct cause of the Three Mile Island and Fukushima nuclear accident. The flow between fuel rods can be roughly considered as the flow in a heated tube for the simplicity of investigation. Due to the high heat flux, the subcooled water flows upward as a boiling two-phase flow. The flow pattern changes from bubble flow, slug flow, churn flow to annular flow. In the annular flow, disturbance waves move upward with supplying water to the heated surface. When the interval of the disturbance waves become large accidentally, the dryout of liquid film occurs. In order to clarify the dryout mechanism, it is necessary to fully understand the behavior of liquid film and be able to predict characteristics of annular flow with reasonable accuracy over wide range of conditions to keep the nuclear power reactors safe from burnout.

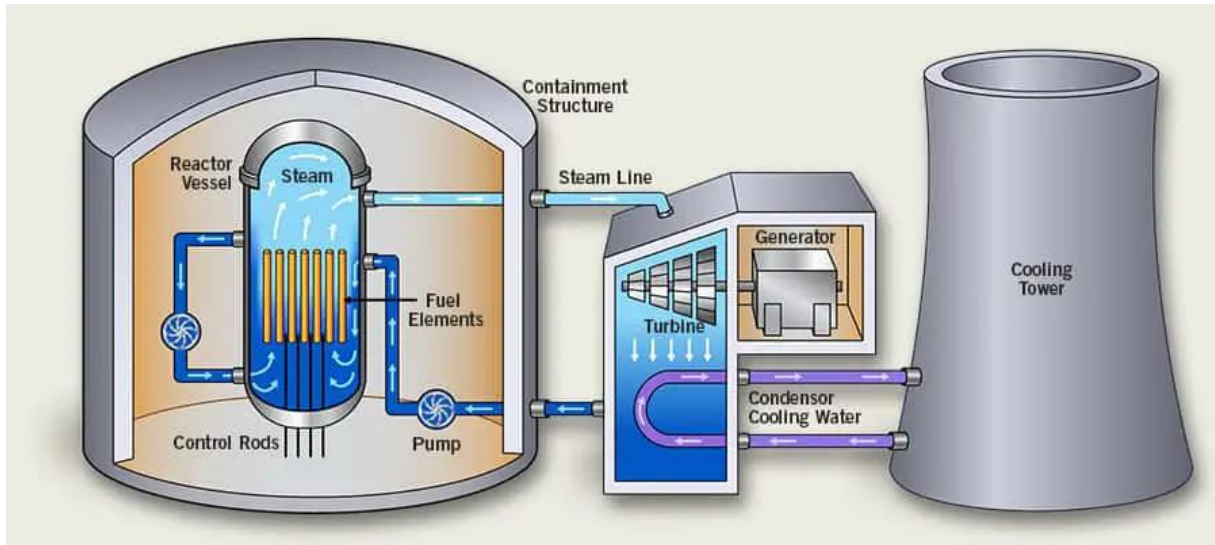


Fig. 1.3 Simplified scheme of plant with boiling water reactor (<https://www.cameco.com>).

1.2 Previous studies in annular flow

Over the past decades, significant attention has been received for annular flow. Through using X-ray imaging, Hewitt and Roberts identified different two-phase flow patterns including slug flow, churn flow, annular flow, wispy annular flow, and bubble flow [9]. Later, Mishima and Ishii introduced two criteria for the annular flow regimes considering the mechanisms of flow-regime transitions. One is based on the flow reversal in the liquid film section along large bubbles, as the annular flow is characterized by the liquid film flow with the same direction of the gas phase. The other one is the onset of the entrainment criteria, since destruction of liquid slugs or large waves by entrainment [10]. As a result, an accurate knowledge of the entrained liquid fraction is essential in the analysis and modeling of annular flows.

Experimental observations of the annular flow shows that the disturbance waves travelling on the liquid film interface are the main source of droplet entrainment [6]. Ishii and Grolmes proposed shearing off of the disturbance wave crest as the primary mechanism of entrainment for the low viscosity liquid such as water [6]. Based on this entrainment mechanism, Ishii and Mishima developed a correlation for the prediction of the entrainment fraction in quasi equilibrium annular flow region [11]. Since then, extensive experimental and theoretical investigation on droplet entrainment has been conducted and correlations for entrainment rate have been proposed [12–15].

In addition to the entrained droplets in the gas core, another important feature of annular flow is the wavy structure of the liquid film. The characteristics of liquid film such as base, average, and maximum liquid film thickness, wave height, wave velocity, wave frequency, wavelength, and wave

pitch, as indicated in Fig. 1.4, have been investigated by numerous researchers. Ishii and Grolmes correlated the average film thickness through the comprehensive consideration of interfacial shear stress and liquid film velocity [6]. Henstock and Hanratty proposed a correlation for film thickness, which is derived from the relationship between interfacial friction factor and film thickness [16]. Fukano and Furukawa measured film thickness using water and glycerol solution at atmospheric pressure and predicted the film thickness using gas Froude number, liquid Reynolds numbers, and quality [17]. Kumar et al. used flush-wire conductivity probes to measure the wave velocity and film thickness of air–water annular flow in a duct. They derived a model for predicting the wave velocity by matching the interfacial shear in the gas and liquid and correlated the base film thickness with liquid and gas Reynolds numbers based on experimental results [18]. Han et al. investigated the effect of gas flow rate on the velocity, height, and frequency of disturbance wave. An average velocity model for the wave and base regions to determine the wave velocity was proposed. They also described the disturbance wave height using the liquid Reynolds number [4]. Hazuku et al. experimented with air–water two-phase flow, and a correlation was proposed between the minimum film thickness with respect to the interfacial shear stress and the liquid Reynolds number [19]. Sawant et al. experimented on air–water annular flow under the pressures of 0.12, 0.4, and 0.58 MPa in a 9.4 mm inner diameter pipe with various liquid flow rates. Through a comprehensive analysis of experimental data, they revealed that using gas Weber number and liquid Reynolds number can predict the dependence of disturbance wave height on pressure, gas flow rate, and liquid flow rate. They reported that only the gas Weber number and liquid phase Reynolds number can satisfactorily predict the dependence of disturbance wave velocity on pressure, liquid, and gas flow rates and that wavelength can be described by liquid and gas Reynolds numbers. They also noted that the correlations available in the literature could not fully predict the wave velocity in their experimental data. [20]. Berna et al. reviewed previous databases and derived a new correlation for predicting the wave velocity by using the gas Reynolds number, liquid Reynolds number, and surface tension factor defined by Ishii and Grolmes [6]. After reviewing previous studies, they obtained a new correlation using the Reynolds and Froude numbers for liquid film thickness prediction [21]. By conducting air–water annular flow experiments, Wolf et al. measured wave velocity and frequency and revealed that wave velocity and frequency take a fairly short distance of about 100 times of diameters to reach a quasi-steady state when liquid is introduced to a porous wall [22]. Ju et al. reviewed the experimental data on annular flow available in the literature and derived two correlations for the wave velocity from liquid interfacial velocity and interfacial shear stress. Their correlations performed better than the other correlations in the literature [23]. Schubring et al. studied air–water annular flow by using a high-speed camera and revealed the

relationship between wave pitch and liquid and gas flow rates [24]. Alekseenko et al. measured the wave pitch in downward annular flow experiments by using a high-speed laser-induced fluorescence technique and emphasized that wave pitch decreased with gas velocity and slightly increased with liquid viscosity and flow rate [25]. Vasques et al. comprehensively studied the properties of disturbance waves by using the brightness-based laser-induced fluorescence technique. They demonstrated that wave intermittency decreases when the flow rate of the base film increases, and that this reduction may either be due to a decrease in the wave pitch at low liquid Reynolds numbers or an increase in disturbance wave wavelength [26]. Nevertheless, in contrast to film thickness, wave velocity, and wave height, which have been extensively studied, the investigation in terms of wave pitch remains limited. Establishing a physical model of wave frequency is difficult because annular flow is a complex problem involving strongly coupled physics. Generally, wave frequency is described by using the Strouhal number, a dimensionless form of wave frequency. Thus far, several empirical correlations for the Strouhal number have been established on the basis of experimental data. Azzopardi correlated wave frequency data by plotting the Strouhal number against the excess liquid Reynolds number [27]. Sawant et al. derived a new correlation for wave frequency by applying the Strouhal number, liquid Reynolds number, and density ratio [20]. On the basis of the experimental results for air–water annular flow in a pipe with an inner diameter of 76.2 mm, Al-Sarkhi et al. reported that wave frequency strongly depends on the modified Lockhart–Martinelli parameter and derived a new correlation [28]. Dasgupta et al. compared the measured wave frequency of air–water annular flow in an 11 mm diameter vertical tube with previous correlations and noted that the correlation from Sekoguchi et al. can predict the data with an error of 30% [29,30]. On the basis of experimental investigation, Wang et al. noted that the wave frequency increases with liquid flow rate and reaches the maximum value when the liquid Reynolds number is ca. 6000–8000. Further increases in the liquid flow rate lead to waves with less frequency [31].

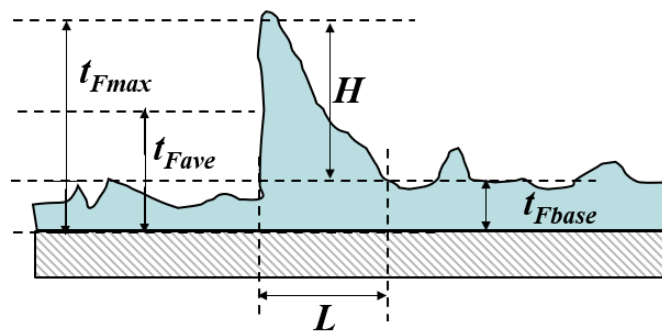


Fig. 1.4 Schematic illustration of liquid film configuration.

On the other hand, in many industrial applications especially energy facilities, it is critical to provide accurate prediction of pressure drop of two-phase flow system for increasing energy conversion efficiency. Meanwhile, accompanied by the wavy structure of the gas-liquid interface, the gas at the core flows upward with a larger frictional pressure drop than it in a smooth wall tube as a single-phase flow due to the higher interfacial shear stress, τ_i , induced by the roughened interface. Considering that interfacial shear stress can make a critical contribution to the pressure drop of two-phase annular flow, interfere with force balances of both gas core and liquid film, and be coupled with liquid film characteristics, accurate prediction of interfacial shear stress has received huge attention and attracted numerous researchers. Conventionally, the interfacial shear stress is expressed by the equation involving gas density, gas velocity, and interfacial friction factor which is denoted by C_{fi} . Wallis [32] derived the correlations for the interfacial friction factor considering the liquid film as a type of wall roughness of single phase flow. Since then, a large amount of correlations of interfacial friction factor were proposed. To the author's best knowledge, these correlations can be roughly divided into 4 types based on the derivation method. The first type of C_{fi} correlations are the Wallis-type correlations which are mostly arithmetic modifications of Wallis correlation. For example, Moeck raised the exponent of the dimensionless average film thickness and altered other coefficients [33]. Fukano and Furukawa introduced the liquid kinetic viscosity to account for the effect of the change in the working fluids viscosity [17]. Fore et al. added gas Reynolds number to Wallis correlation to better predict C_{fi} over a wide range of gas Reynolds numbers and liquid film thicknesses [34]. Ju et al. derived C_{fi} correlation by introducing Weber numbers and viscosity number which are related to the dimensionless average film thickness into Wallis correlation [35]. The second type of C_{fi} correlations relate the interfacial friction factor to the sand-grain roughness of turbulent single-phase flow in rough pipes. Oliemans et al. [36] obtained the correlation for interface roughness employing gas Weber number and combined it with the phenomenological Colebrook equation [37], which expresses the Darcy friction factor as a function of Reynolds number and wall roughness, to predict C_{fi} . Zhao and Bi modified the coefficients in Churchill equation [38], which is a famous approximation of Colebrook equation, to predict the C_{fi} of gas-liquid flow in vertical triangular channel [39]. Belt et al. found the relationship between the average film thickness and equivalent sand-grain roughness, which is obtained from the Churchill equation, and derived the empirical correlation for C_{fi} [40]. The third type of C_{fi} correlations can be treated as the modification of Wallis equation by using a computed single-phase gas friction factor for a smooth walled tube, C_{f_s} , in replace of the constant 0.005 in Wallis equation, represented by Henstock [16], Asali [41], Hajiloo [42], and

Aliyu [43,44]. Last but not least, the forth type of C_{fi} correlations is based on the dimensional analysis on the experimental data as derived by Cioncolini et al. [45].

1.3 Current status and objectives of this study

Although several researchers have investigated the annular flow through experimental and analytical approaches. However, most experimental data and analysis available in the literature are limited to the air–water system under near atmospheric and room temperature while the physical properties of working fluids in these studies are very different from those of the steam–water annular flow in BWRs [19,20,25,31,46–49]. As shown in Table 2.2, the fluids properties of steam-water under BWR operating condition and steam-water under atmospheric pressure and room temperature including information on gas density, liquid density, surface tension, gas viscosity, and liquid viscosity, denoted by ρ_G , ρ_L , σ , μ_G , and μ_L , are listed respectively. It is readily clear that the density ratio of liquid and gas, surface tension, and liquid viscosity, which affect the flow behavior mostly, are quite different between these two conditions [32,50]. Therefore, experimental investigations and mechanistic models for the annular two-phase flow with a wide range of the density ratio, surface tension, and viscosity are required. Moreover, it is in urgent need of studying the annular flow behavior under BWR operating conditions. However, conducting experiments in BWR condition demand for high cost and the experimental condition, which is under high pressure and temperature, is challenging to achieve. Therefore, few experimental data of annular flow under BWR operating condition is available in the literature [51].

In this study, I investigate the characteristics of the annular using nitrogen gas, HFC134a gas, water, and 95% (v/v) aqueous ethanol solution under different pressure conditions. A wide range of density ratio and surface tension will be achieved. Meanwhile, I employ the HFC134a gas and 95% ethanol aqueous solution, whose properties under comparatively low pressure and temperature conditions (0.7 MPa, 40 °C) are similar to those of steam and water under BWR operating conditions (7 MPa, 285 °C) as the working fluids. The properties of working fluids in this study are summarized in Table 2.3. Through conducting gas-liquid annular flow experiments, the liquid film thickness will be carefully measured with respect to time. A detailed schematic illustration for the liquid film time trace under various density ratios, surface tension, and superficial liquid velocity can be obtained. Through systematical analysis and mechanistic interpretation, the annular flow behavior coupled with fluid properties and experimental conditions are expected to be clarified and the empirical correlation will be proposed for predicting the characteristics and behaviors of annular flow.

Overall, the objectives of current study can be summarized as follows:

1. Conduct upward vertical annular flow experiments of Nitrogen–Water system under 0.2 MPa and 0.4MPa, HFC134a–Water system under 0.7 MPa and Nitrogen–95% Ethanol system under 0.2 MPa.
2. Investigate the effect of density ratio and surface tension on the annular flow characteristics including film thickness, wave height, wave pitch, wave frequency, wave velocity, and interfacial shear stress.
3. Based on the experimental data and comprehensive analysis, propose models to predict the characteristics of annular flow.

Table 1.1 Summary of properties for working fluids of Steam–Water under BWR operating condition and Air–Water under low atmospheric pressure and room temperature

System	Pressure (MPa)	Temperature (°C)	ρ_G (kg/m ³)	ρ_L (kg/m ³)	σ (mN/m)	μ_G (μPaS)	μ_L (μPaS)	ρ_L/ρ_G (-)
Steam–Water	7.0	285	37.1	738.1	17.4	19.7	90.8	20
Air–Water	0.12	25	1.41	998.0	72.3	18.4	932.0	707

Table 1.2 Summary of properties for working fluids in current experiments

System	Pressure (MPa)	Temperature (°C)	ρ_G (kg/m ³)	ρ_L (kg/m ³)	σ (mN/m)	μ_G (μPaS)	μ_L (μPaS)	ρ_L/ρ_G (-)
Nitrogen–Water	0.2	25	2.3	997.0	67.4	17.7	850.0	434
	0.4	25	4.5	997.0	67.4	17.7	850.0	222
HFC134a–Water	0.7	40	31.5	992.0	59.0	12.3	570.0	32
Nitrogen–95% Ethanol	0.2	25	2.3	850.0	30.7	17.7	1420.0	370

The originality of this paper is specifically introduced below:

1. Experiments of vertical upward annular flows with wide range of gas-liquid density ratio and surface tension are performed.
2. The single unifying relationship between the wave height and gas Weber number differs under different liquid flow rates is found and interpreted. A unique relationship between the height

and pitch of the disturbance wave is found.

3. Models are derived to predict the average film thickness, height, velocity and frequency of the disturbance wave and evaluated by multiple databases.

1.4 Structure of the thesis

In order to achieve the objectives stated above, this thesis has been structured into six different Chapters.

Chapter 1 is the introduction on emphasizing the significance of two-phase pipe flow in practical applications and research on the annular flow up to the present.

Chapter 2 of this thesis introduce the study on the effect of density ratio and surface tension on the average film thickness and disturbance wave height based on the experimental result of annular flow in a 5mm tube.

Chapter 3 focuses on the effect of density ratio and surface tension on the velocity, wavelength, pitch, intermittency and frequency of disturbance waves. Unique relationships on the wave pitch and intermittency are introduced.

Chapter 4 discusses experimental investigation on the pressure drop and interfacial shear stress of annular flow.

Chapter 5 summarizes the conclusions drawn from this study and recommendations for further work.

In the appendix, the detailed information on the film thickness measurement sensors, prepared working liquids, and dynamic performance of the sensors are described.

References

- [1] J.-M. Le Corre, U.C. Bergmann, A. Hallehn, H. Tejne, F. Waldemarsson, B. Morenius, R. Baghai, Measurements of local two-phase flow parameters in fuel bundle under BWR operating conditions, *Nucl. Eng. Des.* 336 (2018) 15–23. <https://doi.org/10.1016/j.nucengdes.2017.04.033>.
- [2] A. Sandá, S.L. Moya, L. Valenzuela, Modelling and simulation tools for direct steam generation in parabolic-trough solar collectors: A review, *Renew. Sustain. Energy Rev.* 113 (2019) 109226. <https://doi.org/10.1016/j.rser.2019.06.033>.
- [3] K.J. Chu, A.E. Dukler, Statistical characteristics of thin, wavy films III. Structure of the large waves and their resistance to gas flow, *AIChE J.* 21 (1975) 583–593. <https://doi.org/10.1002/aic.690210323>.
- [4] H. Han, Z. Zhu, K. Gabriel, A study on the effect of gas flow rate on the wave characteristics in two-phase gas–liquid annular flow, *Nucl. Eng. Des.* 236 (2006) 2580–2588. <https://doi.org/10.1016/j.nucengdes.2006.03.015>.
- [5] S. Mori, T. Fukano, Relation between the occurrence of Burnout and differential pressure fluctuation characteristics caused by the disturbance waves passing by a flow obstacle in a vertical boiling two-phase upward flow in a narrow annular channel, *Nucl. Eng. Des.* 236 (2006) 985–992. <https://doi.org/10.1016/j.nucengdes.2005.09.005>.
- [6] M. Ishii, M.A. Grolmes, Inception criteria for droplet entrainment in two-phase concurrent film flow, *AIChE J.* 21 (1975) 308–318. <https://doi.org/10.1002/aic.690210212>.
- [7] D.B. Hann, A.V. Cherdantsev, B.J. Azzopardi, Study of bubbles entrapped into a gas-sheared liquid film, *Int. J. Multiph. Flow.* 108 (2018) 181–201. <https://doi.org/10.1016/j.ijmultiphaseflow.2018.07.001>.
- [8] N. Borhani, J.R. Thome, Intermittent dewetting and dryout of annular flows, *Int. J. Multiph. Flow.* 67 (2014) 144–152. <https://doi.org/10.1016/j.ijmultiphaseflow.2014.04.009>.
- [9] G.F. Hewitt, D.N. Roberts, *Studies of two-phase flow patterns by simultaneous x-ray and flash photography*, (1969).
- [10] K. Mishima, M. Ishii, Flow regime transition criteria for upward two-phase flow in vertical tubes, *Int. J. Heat Mass Transf.* 27 (1984) 723–737. [https://doi.org/10.1016/0017-9310\(84\)90142-X](https://doi.org/10.1016/0017-9310(84)90142-X).
- [11] M. Ishii, K. Mishima, Droplet entrainment correlation in annular two-phase flow, *Int. J. Heat Mass Transf.* 32 (1989) 1835–1846. [https://doi.org/10.1016/0017-9310\(89\)90155-5](https://doi.org/10.1016/0017-9310(89)90155-5).
- [12] T. Okawa, T. Kitahara, K. Yoshida, T. Matsumoto, I. Kataoka, New entrainment rate correlation in annular two-phase flow applicable to wide range of flow condition, *Int. J. Heat Mass Transf.* (2002). [https://doi.org/10.1016/S0017-9310\(01\)00111-9](https://doi.org/10.1016/S0017-9310(01)00111-9).

- [13] P. Sawant, M. Ishii, M. Mori, Droplet entrainment correlation in vertical upward co-current annular two-phase flow, *Nucl. Eng. Des.* 238 (2008) 1342–1352. <https://doi.org/10.1016/j.nucengdes.2007.10.005>.
- [14] G. Wang, P. Sawant, M. Ishii, A new entrainment rate model for annular two-phase flow, *Int. J. Multiph. Flow.* 124 (2020) 103185. <https://doi.org/10.1016/j.ijmultiphaseflow.2019.103185>.
- [15] A. Cioncolini, J.R. Thome, Prediction of the entrained liquid fraction in vertical annular gas–liquid two-phase flow, *Int. J. Multiph. Flow.* 36 (2010) 293–302. <https://doi.org/10.1016/j.ijmultiphaseflow.2009.11.011>.
- [16] W.H. Henstock, T.J. Hanratty, The interfacial drag and the height of the wall layer in annular flows, *AIChE J.* 22 (1976) 990–1000. <https://doi.org/10.1002/aic.690220607>.
- [17] T. Fukano, T. Furukawa, Prediction of the effects of liquid viscosity on interfacial shear stress and frictional pressure drop in vertical upward gas–liquid annular flow, *Int. J. Multiph. Flow.* 24 (1998) 587–603. [https://doi.org/10.1016/S0301-9322\(97\)00070-0](https://doi.org/10.1016/S0301-9322(97)00070-0).
- [18] R. Kumar, M. Gottmann, K.R. Sridhar, Film Thickness and Wave Velocity Measurements in a Vertical Duct, *J. Fluids Eng.* 124 (2002) 634–642. <https://doi.org/10.1115/1.1493808>.
- [19] T. Hazuku, T. Takamasa, Y. Matsumoto, Experimental study on axial development of liquid film in vertical upward annular two-phase flow, *Int. J. Multiph. Flow.* 34 (2008) 111–127. <https://doi.org/10.1016/j.ijmultiphaseflow.2007.10.008>.
- [20] P. Sawant, M. Ishii, T. Hazuku, T. Takamasa, M. Mori, Properties of disturbance waves in vertical annular two-phase flow, *Nucl. Eng. Des.* 238 (2008) 3528–3541. <https://doi.org/10.1016/j.nucengdes.2008.06.013>.
- [21] C. Berna, A. Escrivá, J.L. Muñoz-Cobo, L.E. Herranz, Review of droplet entrainment in annular flow: Interfacial waves and onset of entrainment, *Prog. Nucl. Energy.* 74 (2014) 14–43. <https://doi.org/10.1016/j.pnucene.2014.01.018>.
- [22] A. Wolf, S. Jayanti, G.F. Hewitt, Flow development in vertical annular flow, *Chem. Eng. Sci.* (2001). [https://doi.org/10.1016/S0009-2509\(00\)00546-7](https://doi.org/10.1016/S0009-2509(00)00546-7).
- [23] P. Ju, Y. Liu, X. Yang, M. Ishii, Wave characteristics of vertical upward adiabatic annular flow in pipes, *Int. J. Heat Mass Transf.* 145 (2019) 118701. <https://doi.org/10.1016/j.ijheatmasstransfer.2019.118701>.
- [24] D. Schubring, T.A. Shedd, E.T. Hurlburt, Studying disturbance waves in vertical annular flow with high-speed video, *Int. J. Multiph. Flow.* 36 (2010) 385–396. <https://doi.org/10.1016/j.ijmultiphaseflow.2010.01.003>.
- [25] S.V. Alekseenko, A.V. Cherdantsev, M.V. Cherdantsev, S.V. Isaenkov, D.M. Markovich, Study

of formation and development of disturbance waves in annular gas–liquid flow, *Int. J. Multiph. Flow.* 77 (2015) 65–75. <https://doi.org/10.1016/j.ijmultiphaseflow.2015.08.007>.

[26] J. Vasques, A. Cherdantsev, M. Cherdantsev, S. Isaenkov, D. Hann, Comparison of disturbance wave parameters with flow orientation in vertical annular gas-liquid flows in a small pipe, *Exp. Therm. Fluid Sci.* 97 (2018) 484–501. <https://doi.org/10.1016/j.expthermflusci.2018.03.020>.

[27] B.J. Azzopardi, Disturbance wave frequencies, velocities and spacing in vertical annular two-phase flow, *Nucl. Eng. Des.* 92 (1986) 121–133. [https://doi.org/10.1016/0029-5493\(86\)90240-2](https://doi.org/10.1016/0029-5493(86)90240-2).

[28] A. Al-Sarkhi, C. Sarica, K. Magrini, Inclination effects on wave characteristics in annular gas-liquid flows, *AIChE J.* 58 (2012) 1018–1029. <https://doi.org/10.1002/aic.12653>.

[29] A. Dasgupta, D.K. Chandraker, S. Kshirasagar, B.R. Reddy, R. Rajalakshmi, A.K. Nayak, S.P. Walker, P.K. Vijayan, G.F. Hewitt, Experimental investigation on dominant waves in upward air-water two-phase flow in churn and annular regime, *Exp. Therm. Fluid Sci.* 81 (2017) 147–163. <https://doi.org/10.1016/j.expthermflusci.2016.10.012>.

[30] M. Nakazatomi, K. Sekoguchi, Effect of pressure on entrainment flow rate in vertical upward gas—liquid annular two-phase flow. Part II: An assessment of published correlations of entrainment flow rate through high-pressure data and proposal of new correlations, *Heat Transf. - Jpn. Res.* 25 (1996) 281–292. [https://doi.org/10.1002/\(SICI\)1520-6556\(1996\)25:5<281::AID-HTJ2>3.0.CO;2-T](https://doi.org/10.1002/(SICI)1520-6556(1996)25:5<281::AID-HTJ2>3.0.CO;2-T).

[31] G. Wang, Z. Dang, M. Ishii, Wave structure and velocity in vertical upward annular two-phase flow, *Exp. Therm. Fluid Sci.* 120 (2021) 110205. <https://doi.org/10.1016/j.expthermflusci.2020.110205>.

[32] G.B. Wallis, *One-dimensional two-phase flow*, McGraw-Hill, New York, 1969.

[33] E.O. Moeck, *Annular-dispersed two-phase flow and critical heat flux*, Canada, 1970. http://inis.iaea.org/search/search.aspx?orig_q=RN:01002083.

[34] L.B. Fore, S.G. Beus, R.C. Bauer, Interfacial friction in gas–liquid annular flow: analogies to full and transition roughness, *Int. J. Multiph. Flow.* 26 (2000) 1755–1769. [https://doi.org/10.1016/S0301-9322\(99\)00114-7](https://doi.org/10.1016/S0301-9322(99)00114-7).

[35] P. Ju, Y. Liu, C.S. Brooks, M. Ishii, Prediction of interfacial shear stress of vertical upward adiabatic annular flow in pipes, *Int. J. Heat Mass Transf.* 133 (2019) 500–509. <https://doi.org/10.1016/j.ijheatmasstransfer.2018.12.057>.

[36] R.V.A. Oliemans, B.F.M. Pots, N. Trompé, Modelling of annular dispersed two-phase flow in vertical pipes, *Int. J. Multiph. Flow.* 12 (1986) 711–732. [https://doi.org/10.1016/0301-9322\(86\)90047-9](https://doi.org/10.1016/0301-9322(86)90047-9).

[37] C.F. Colebrook, *Turbulent flow in pipes, with particular reference to the transition region*

between the smooth and rough pipe laws., *J. Inst. Civ. Eng.* 11 (1939) 133–156. <https://doi.org/10.1680/ijoti.1939.14509>.

[38] S.W. Churchill, Friction-factor equation spans all fluid-flow regimes., *Chem. Eng.* 84 (1977) 91–92.

[39] T.S. Zhao, Q.C. Bi, Pressure drop characteristics of gas–liquid two-phase flow in vertical miniature triangular channels, *Int. J. Heat Mass Transf.* 44 (2001) 2523–2534. [https://doi.org/10.1016/S0017-9310\(00\)00282-9](https://doi.org/10.1016/S0017-9310(00)00282-9).

[40] R.J. Belt, J.M.C. Van't Westende, L.M. Portela, Prediction of the interfacial shear-stress in vertical annular flow, *Int. J. Multiph. Flow.* 35 (2009) 689–697. <https://doi.org/10.1016/j.ijmultiphaseflow.2008.12.003>.

[41] J.C. Asali, T.J. Hanratty, P. Andreussi, Interfacial drag and film height for vertical annular flow, *AIChE J.* 31 (1985) 895–902. <https://doi.org/10.1002/aic.690310604>.

[42] M. Hajiloo, B.H. Chang, A.F. Mills, Interfacial shear in downward two-phase annular co-current flow, *Int. J. Multiph. Flow.* 27 (2001) 1095–1108. [https://doi.org/10.1016/S0301-9322\(00\)00065-3](https://doi.org/10.1016/S0301-9322(00)00065-3).

[43] A.M. Aliyu, L. Lao, A.A. Almagbrok, H. Yeung, Interfacial shear in adiabatic downward gas/liquid co-current annular flow in pipes, *Exp. Therm. Fluid Sci.* 72 (2016) 75–87. <https://doi.org/10.1016/j.expthermflusci.2015.10.025>.

[44] A.M. Aliyu, Y.D. Baba, L. Lao, H. Yeung, K.C. Kim, Interfacial friction in upward annular gas–liquid two-phase flow in pipes, *Exp. Therm. Fluid Sci.* 84 (2017) 90–109. <https://doi.org/10.1016/j.expthermflusci.2017.02.006>.

[45] A. Cioncolini, J.R. Thome, C. Lombardi, Unified macro-to-microscale method to predict two-phase frictional pressure drops of annular flows, *Int. J. Multiph. Flow.* 35 (2009) 1138–1148. <https://doi.org/10.1016/j.ijmultiphaseflow.2009.07.005>.

[46] D. Schubring, A.C. Ashwood, T.A. Shedd, E.T. Hurlburt, Planar laser-induced fluorescence (PLIF) measurements of liquid film thickness in annular flow. Part I: Methods and data, *Int. J. Multiph. Flow.* 36 (2010) 815–824. <https://doi.org/10.1016/j.ijmultiphaseflow.2010.05.007>.

[47] P. de Jong, K.S. Gabriel, A preliminary study of two-phase annular flow at microgravity: experimental data of film thickness, *Int. J. Multiph. Flow.* 29 (2003) 1203–1220. [https://doi.org/10.1016/S0301-9322\(03\)00085-5](https://doi.org/10.1016/S0301-9322(03)00085-5).

[48] R. Lin, K. Wang, L. Liu, Y. Zhang, S. Dong, Study on the characteristics of interfacial waves in annular flow by image analysis, *Chem. Eng. Sci.* 212 (2020) 115336. <https://doi.org/10.1016/j.ces.2019.115336>.

- [49] L. Pan, H. He, P. Ju, T. Hibiki, M. Ishii, The influences of gas–liquid interfacial properties on interfacial shear stress for vertical annular flow, *Int. J. Heat Mass Transf.* 89 (2015) 1172–1183. <https://doi.org/10.1016/j.ijheatmasstransfer.2015.06.022>.
- [50] G.F. Hewitt, N.S. Hall-Taylor, *Annular two-phase flow*, 1st ed., Pergamon Press, Oxford, New York, 1970.
- [51] J. Würtz, *An experimental and theoretical investigation of annular steam-water flow in tubes and annuli at 30 to 90 bar*, Risø National Laboratory Roskilde, 1978.

CHAPTER 2

Effect of density ratio and surface tension on liquid film thickness and disturbance wave height

In this chapter, I use nitrogen gas and water under the system pressures of 0.2 and 0.4 MPa, as well as HFC134a gas and water under the system pressure of 0.7 MPa as working fluids to conduct annular flow experiments. The density ratio can be varied between 32 and 434. Based on my experimental data, I report a direct link between the film thickness, wave height, and dimensionless numbers. The analysis indicates the Weber number which represents the ratio of the fluid inertia force to the surface tension force is critical for the film thickness behavior. To examine this, I perform the experiments using nitrogen gas and 95% (v/v) of aqueous ethanol solution under the system pressure of 0.2 MPa. Finally, two models are proposed to predict the averaged film thickness and wave height, which are then compared with previous data.

2.1 Introduction

Annular two-phase flow is a common but highly crucial flow regime encountered in many practical applications, such as nuclear reactors, refrigeration systems, and steam boilers [1,2]. It is characterized as a continuously flowing gas core at the center and a liquid film attached to the channel wall. Notably, the film thickness, together with the disturbance wave that occurs at the gas–liquid interface, is of great significance to the nuclear industry because the dryout of the liquid film always occurs at the thin base film between two successive disturbance waves when the interval of the disturbance waves becomes large [3,4]. This may result in the burnout of the heating components, and an accurate film thickness prediction is required. Moreover, the film thickness and wave height play a crucial role in droplet entrainment in annular two-phase flow [5]. Hence, the film thickness and disturbance wave in the annular flow have been studied by several researchers.

Based on the consideration of the interfacial shear stress τ_i and the assumption of the interfacial friction factor (C_{fi}) and liquid film velocity using empirical correlations, Ishii and Grolmes [5] expressed the film thickness in terms of liquid Reynolds number and τ_i . Henstock and Hanratty [6] correlated the C_{fi} with a group of dimensionless numbers and used the C_{fi} relationship to derive the correlation for the film thickness. Fukano and Furukawa [7] measured film thickness using water and glycerol solution at atmospheric pressure and predicted the film thickness using gas Froude number,

liquid Reynolds numbers, and quality. Kumar et al. [8] observed the air–water annular flow in a rectangular duct and correlated the base film thickness with liquid and gas Reynolds numbers based on experimental results. Han et al. [9] investigated the disturbance wave in the air–water annular flow and described the disturbance wave height using the liquid Reynolds number. Hazuku et al. [10] experimented with air–water two-phase flow, and a correlation was proposed between the minimum film thickness with respect to the τ_i and the liquid Reynolds number. Sawant et al. [11] experimented on air–water annular flow under the pressures of 0.12, 0.4, and 0.58 MPa with various liquid flow rates. Through a comprehensive analysis of experimental data, they revealed that using gas Weber number and liquid Reynolds number can predict the dependence of disturbance wave height on pressure, gas flow rate, and liquid flow rate. Next, after conducting an extensive review of previous studies, Berna et al. [12] obtained a new correlation using the Reynolds and Froude numbers for liquid film thickness prediction.

Previous studies considerably contributed to the development of models for the film thickness and disturbance wave in annular flows [13–18]. However, most experiments and mechanistic models are accomplished through investigating air–water annular flows under atmospheric conditions, but the liquid–gas density ratio is relatively high under such conditions. Considering that the density ratio is rather low in actual nuclear applications, experimental investigations and mechanistic models for the annular two-phase flow with a wide range of the density ratio are required.

In this study, I investigate the characteristics of the film thickness and disturbance waves using nitrogen gas, HFC134a gas, water, and 95% (v/v) aqueous ethanol solution under different pressure conditions. A wide density ratio range of 32–434 is achieved and the surface tension varies from 30.7 to 72.0 mN/m. During the experiments, the liquid film thickness is carefully measured with respect to time in the vertical upward annular flows. A detailed schematic illustration for the liquid film time trace under various density ratios, surface tension, and superficial liquid velocity is presented. From the experimental data analysis, the relationship between dimensionless numbers and film thickness as well as between dimensionless numbers and wave height are revealed. Finally, two models are derived to predict the average film thickness and wave height, which are then compared with experimental data from previous research. Compared with the previous study by Sawant et al. [11], this work constitutes a significant step forward in extending the density ratio from 147 to 32 which is closer to the density ratio in boiling water, evaluating the film thickness behavior of working fluids with different surface tension, and interpreting the observed phenomenon through theoretical analysis.

2.2 Experimental apparatus and procedures

2.2.1 Working fluids

The experimental conditions are summarized in Table 1.2, including information on gas density, liquid density, surface tension, gas viscosity, and liquid viscosity, which are obtained from literature and denoted by ρ_G , ρ_L , σ , μ_G , and μ_L , respectively [19]. Distilled water with a 0.03-wt% salt solution and 95% (v/v) of aqueous ethanol solution with a 0.8-wt% salt solution is employed as the working liquid. The electrical conductivity of the water is 1000 ± 100 S/cm and is measured before and after each experiment.

Nitrogen gas under 0.2 and 0.4 MPa and HFC134a gas under 0.7 MPa are used as the working gas. With the nitrogen and HFC134a gases under different pressures, the liquid–gas density ratio ranges from 32 to 434, while the steam–water density ratio in the boiling water reactor operating condition is around 30.

2.2.2 Experimental apparatus

A schematic of the experimental apparatus is shown in Fig. 2.1. The test section, which is made of non-conductive polycarbonate resin, is placed vertically. The working liquids are supplied from liquid tanks and transported by a feed pump. The flow rate of the working liquids is measured using a flow meter (Vision 1005-2F66 series, Badge Meter) with an accuracy of $\pm 3\%$. A heater comprising the temperature controller is placed in the liquid tank to keep the liquid temperature constant. The working gas is generated from the HFC134a liquid tank, which comprises a heater as well for gas generation, and its flow rate is measured using a YOKOGAWA EJA115 flow transmitter with an accuracy of $\pm 5\%$. To superheat the HFC134a gas, another hereafter is placed downstream of the HFC134a liquid tank. The working liquid and gas are mixed in a mixer at the inlet of the test section and then flow upward to the test section. The system pressure in the test section is controlled by a flow control valve at the test section downstream and measured by a Huba 510 pressure transmitter with an accuracy of $\pm 0.5\%$. During the experiment, to ensure that the HFC134a gas does not condense in the test section, the pressure and temperature of the HFC134a gas are controlled minutely. A separator is placed downstream of the test section to separate the gas–liquid mixture. The separated liquid flows back to the liquid tank, whereas the gas is ejected into the atmosphere. However, in the experiment condition of the HFC134a–water system, the HFC134a gas flows into a condenser

installed in the reservoir and is cooled below the saturation temperature and collected.

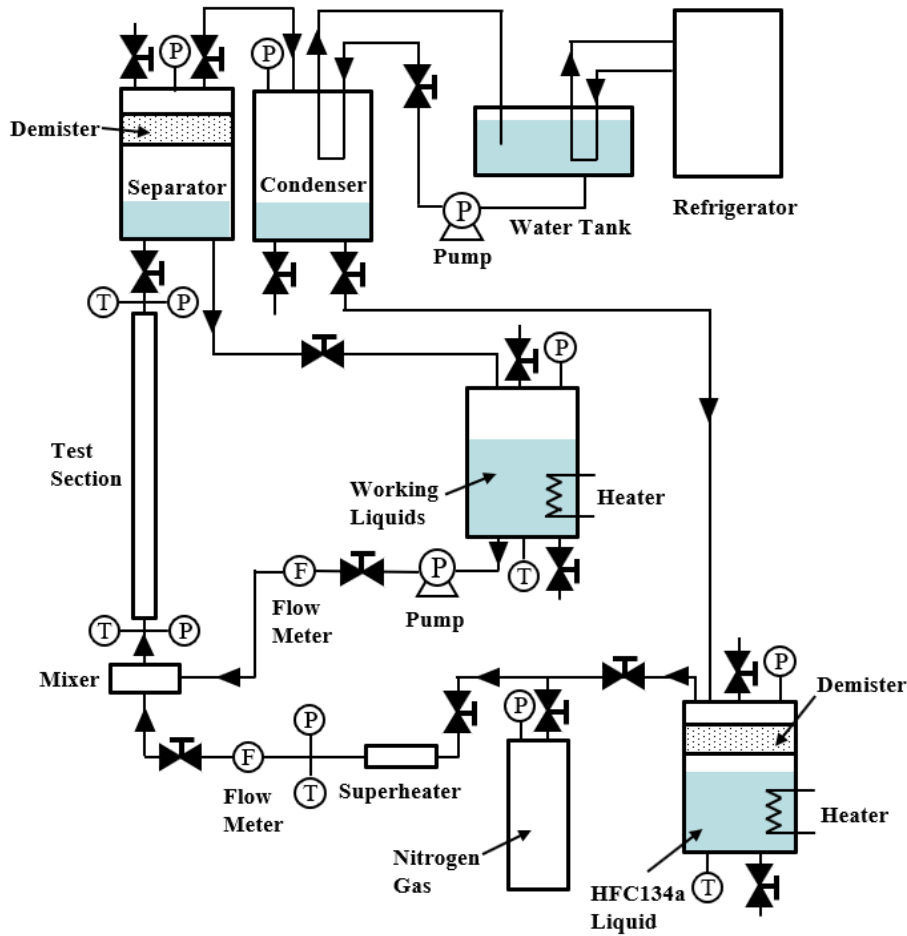


Fig. 2.1 Schematic illustration of the experimental facility.

A detailed schematic illustration of the test section is shown in Fig. 2.2. The test section is 1,500 and 5 mm in length and inner diameter, respectively. A developing length ($L/D = 300$) is selected to ensure that the measurements correspond to the fully developed equilibrium annular flow, which is in accordance with the correlation proposed by Kataoka and Ishii [20]. The liquid–gas mixer comprises a porous tube with an average pore diameter of 120 μm and an inner diameter of 5 mm which is almost equal to that of the test section. The liquid is supplied to the test section through the porous wall, whereas the gas is injected from the bottom of the mixer unit directly into the center of the test section. For the annular flow, this injection method using a porous tube can minimize the initial entrainment, also known as the entrance effect [21].

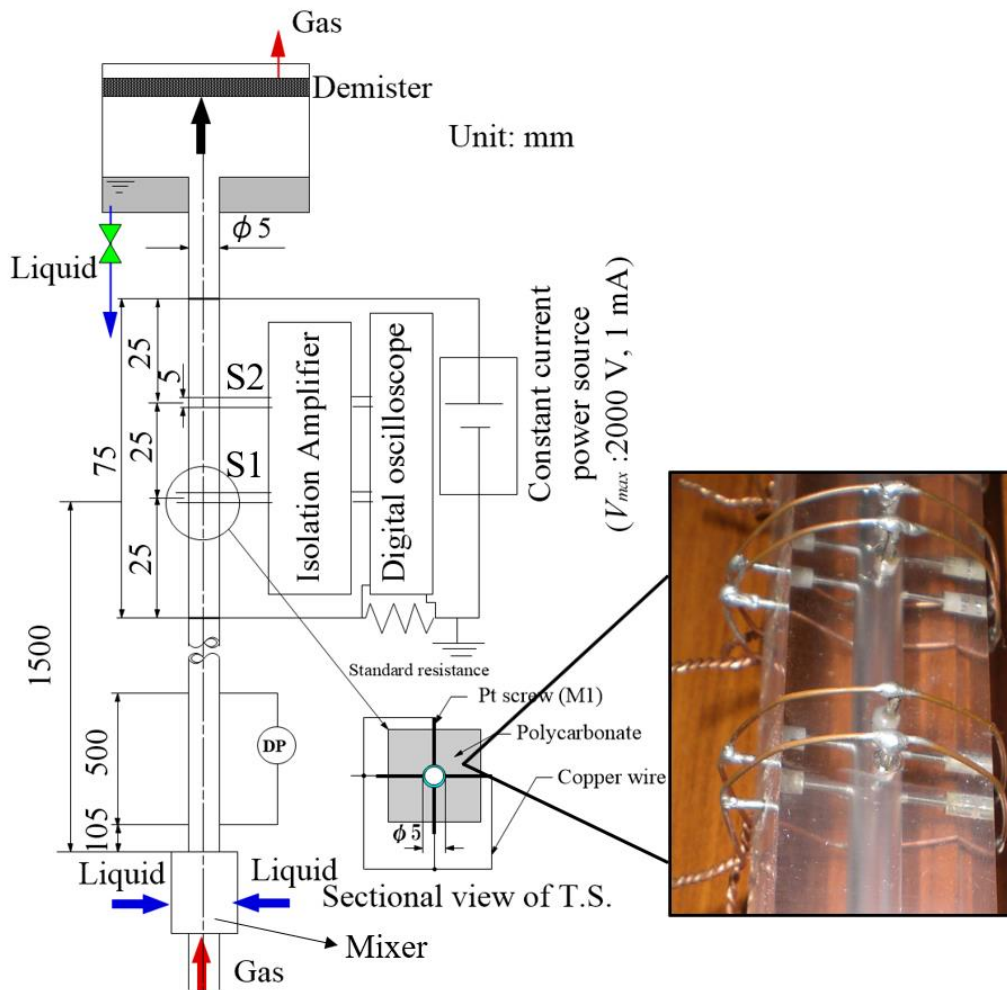


Fig. 2.2 Schematic illustration of the test section.

2.2.3 Test section

To measure the liquid film thickness in annular two-phase flows, several methods have been proposed, e.g., conductance probe, capacitance probe, optical camera, and X-ray methods [11,15,16,22–29]. In this study, the constant electric current method (CECM), a variant of the conductance probe method, is used to measure the time-varying liquid film thickness [27]. The CECM has a constant current density and high linearity in the liquid film, enabling accurate measurement even in thin film thickness regions. Two sets of sensors with an accuracy of $\pm 5\%$, named S1 and S2, are installed in the test section for the film thickness measurement (Fig. 2.2). Each sensor comprises one pair of conductance probes. The axial distance between one pair of conductance probes, l , is 5.0 mm. The electric current of the main circuit is fixed at 1.0 mA, which is provided by the constant current power source (the maximum output voltage is 2,000 V) and measured using a standard electric resistance of 1 k Ω . The time-varying voltage and current output from these sensors are recorded

simultaneously using a YOKOGAWA DL850E digital oscilloscope with an accuracy of $\pm 0.5\%$ at a sampling frequency of 5 kHz over the length of the 10,000 data points (2 s). An isolation amplifier is placed between the sensors and oscilloscope, to protect the oscilloscope from voltage overshoot. As shown in the cross-sectional view of the test section in Fig. 2.2, four M1 screws, which are employed to detect the electric current in the liquid film and form the conductance probe, are fixed vertically to the channel and connected by copper wire on the outside.

2.2.4 Film thickness measurement methods and measurement accuracy

To measure the film thickness, it is necessary to perform the calibration. I first insert a nonconductive polytetrafluoroethylene (PTFE) rod into the test section. The inner diameter of the PTFE rod, D_c , is 4.6 mm. Then the liquid film thickness is kept constant at 0.2 mm as shown in Fig. 2.3(a) and its electrical resistance over l , which is denoted by R_c , can be expressed by:

$$R_c = \frac{V_c}{I_c} = \rho \frac{l}{\frac{\pi}{4}(D^2 - D_c^2)}, \quad (2.1)$$

where $D = 5.0$ mm is the inner diameter of the test section, ρ denotes the electrical conductivity of the working liquid, and I_c and V_c denote the measured electric current of the main circuit and the measured voltage output between one pair of conductance probes during the calibration, respectively. Similarly, when two-phase flow in the test section with a film thickness of t_F as shown in Fig. 2.3(b), the measured electrical resistance of the liquid film over l can be expressed by:

$$R_m = \frac{V}{I} = \rho \frac{l}{\frac{\pi}{4}(D^2 - (D - t_F)^2)}, \quad (2.2)$$

where I and V denote the measured electric current of the main circuit and the measured voltage output between one pair of conductance probes in the two-phase flows experiments, respectively; The measured film thickness is obtained as both an axial mean value over an axial length of 5.0 mm and an azimuthal value. The cross-sectional average of the time-varying liquid thickness signals from the constant current holdup sensors is obtained by combining Eq. (2.1) and Eq. 2.2):

$$t_F = \frac{D}{2} \left[1 - \left[1 - \frac{V_c I (D^2 - D_c^2)}{V I_c D^2} \right]^{0.5} \right], \quad (2.3)$$

The calibration is performed before and after each experiment.

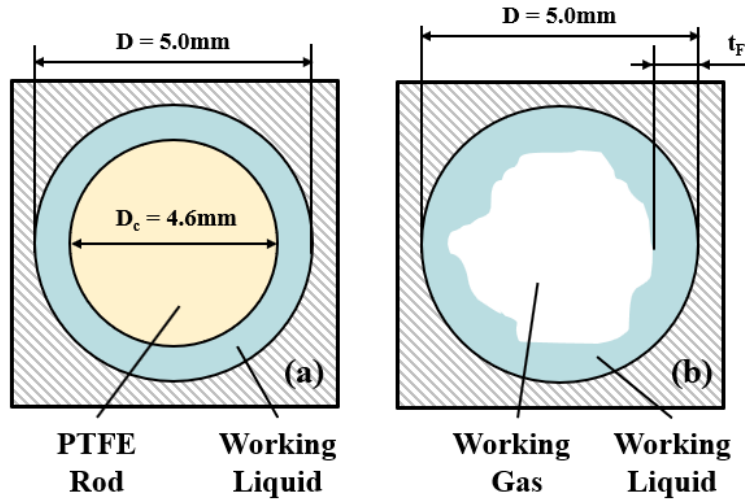


Fig. 2.3 Cross-sectional view of the test section when filled with working liquid and (a) PTFE Rod and (b) working gas.

Fig. 2.4 shows an example of static calibration using the non-conductive PTFE rods and water with 0.8-wt% salt solution. The rods with a diameter of 4.0, 4.2, 4.4, 4.6, and 4.8 mm are used in the calibration corresponding to a film thickness of 0.5, 0.4, 0.3, 0.2, and 0.1 mm. As shown in the figure, the error between the film thickness calculated by Eq. (2.3) and the actual film thickness is around $\pm 5\%$. Fig. 2.4 also shows that this method is extremely linear, so its linearity is expected to hold even in thin film thickness regions since the current density is always uniform in a constant electric current method (CECM) [27].

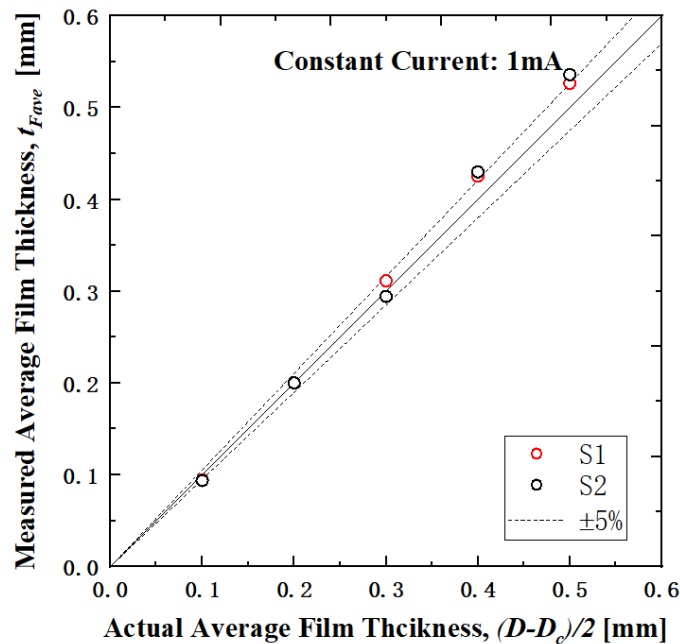


Fig. 2.4 Static calibration by nonconductive rods.

2.2.5 Experimental conditions

As described above, the gas–liquid flow experiments are performed under the pressure of 0.2 and 0.4 MPa for the nitrogen–water, 0.2MPa for the nitrogen-95% aqueous ethanol solution system, and 0.7 MPa for the HFC134a–water system. The superficial liquid velocity, denoted by j_L , at the test section is set at 0.1, 0.4, and 0.8 m/s for each pressure condition. The Hewitt–Roberts and Mishima–Ishii flow regime maps [30,31] are employed to indicate the flow regime of experiments corresponding to different experimental conditions (Fig. 2.5). Most flows are classified into the annular flow. Some flows with a superficial gas velocity of around 0.1 m/s are close to the transition regime of annular and churn flows.

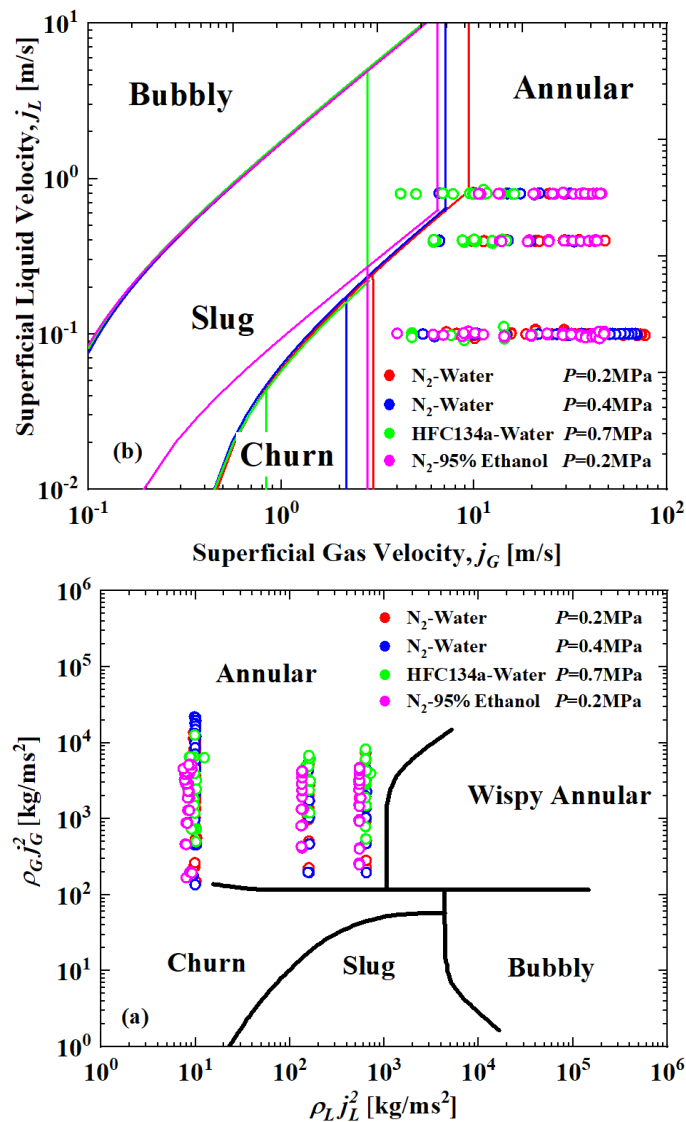


Fig. 2.5 Test matrix represented on the (a) Hewitt–Roberts flow map and (b) Mishima–Ishii flow map [30,31].

Nitrogen-Water System

$$P = 0.2 \text{ MPa}$$

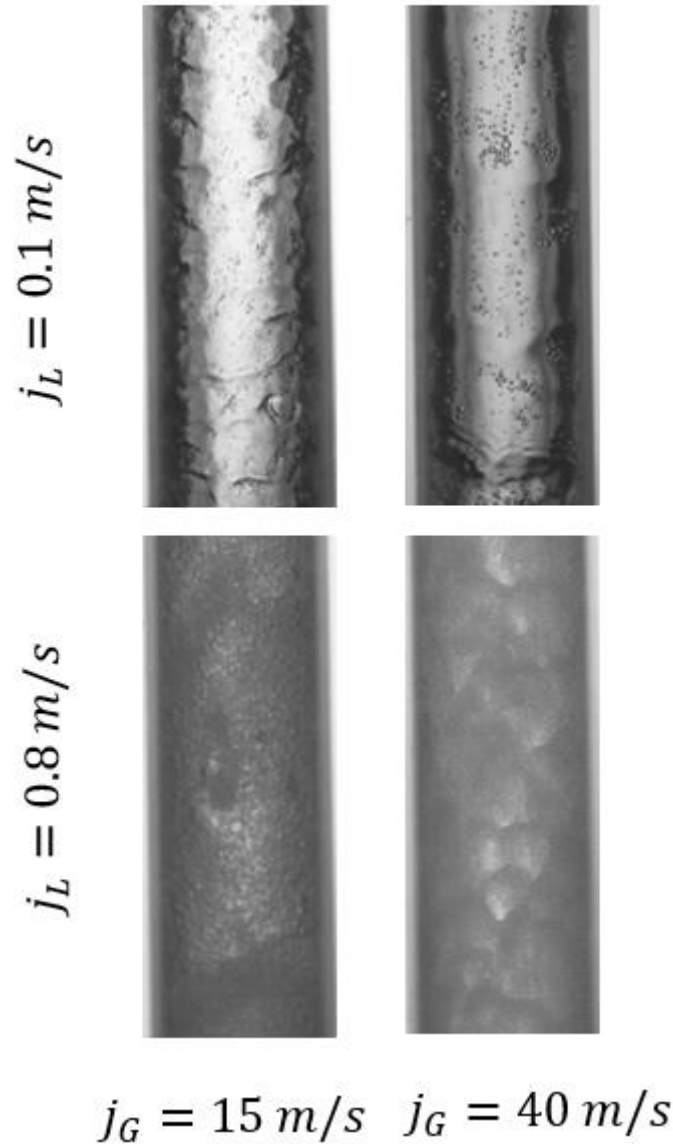


Fig. 2.6 Snapshots of annular flow of Nitrogen-Water system under the pressure 0.2 MPa in the 5.0 mm inner diameter tube.

In the Fig. 2.6, the flow configuration of Nitrogen-Water annular flows under 0.2 MPa with $j_L = 0.1$ and 0.8 m/s and $j_G = 15$ and 40 m/s is shown. It is readily apparent that under low liquid flow rate the liquid film and gas core can be clearly distinguished while under high liquid flow rate the number of bubbles in the liquid film increases extensively. As a result, it is difficult to determine the gas-liquid interface since the large number of bubbles move with very high speed. This could be

attributed to the increase of the fraction of the droplets or remnants of transitional liquid structures impacting on the liquid film and overturning of the fast-moving waves.

2.2.6 Film thickness data processing

From the obtained data of film thickness time trace, the probability density function is calculated and plotted against film thickness (Fig. 2.7). To compute the probability density function, the film thickness is divided into intervals with a width of 1 μm , ranging from 0 to 5 mm. The frequency of measured film thickness in each interval is counted. Then, the probability density function can be calculated by dividing the frequency for each interval by the total number of film thickness measurements, which is 10,000.

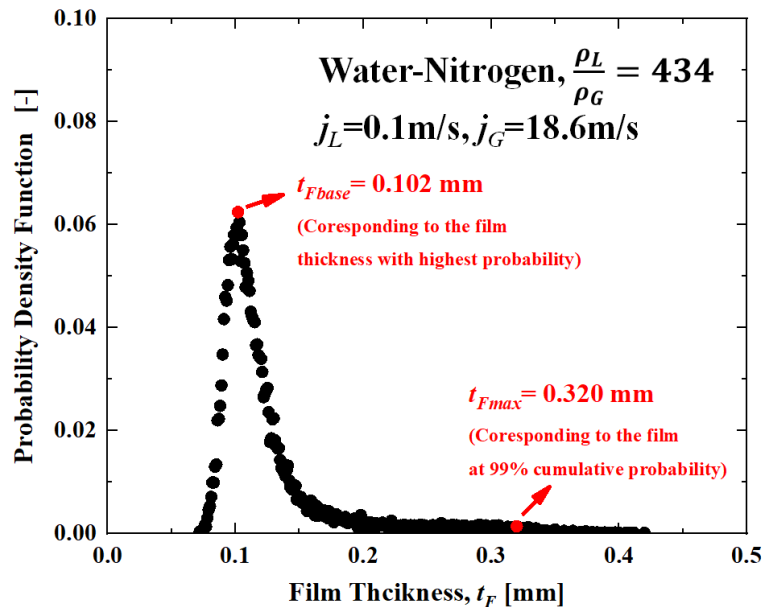


Fig. 2.7 The probability density function of film thickness when $j_L = 0.1 \text{ m/s}$, $j_G = 18.6 \text{ m/s}$ with a density ratio of 434.

I define the film thickness with the highest probability as the base film thickness denoted by t_{Fbase} and the film thickness with the 99% cumulative probability as the maximum film thickness denoted by t_{Fmax} . This definition of maximum film thickness is employed by Fukano and Furukawa [7] and Hazuku et al. [10], showing a good fitting with the film thickness time trace. Then, the disturbance wave height, H , is defined as the difference between the base and maximum film thicknesses. It is worth noting that the local wave height may deviate from the measured wave height which is measured as the mean value of the 5 mm measurement section as mentioned in section 2.4.

The average film thickness, t_{Fave} , is the arithmetic mean value of film thickness.

2.2.7 Uncertainty analysis

The superficial liquid and gas velocities were calculated from the electrical signals obtained by flow meters using the calibration relationships. To calibrate the superficial liquid velocity, I measured the water flows into a measuring cylinder in a specific period. To calibrate the superficial gas velocity, I immersed an upside-down laboratory measuring cylinder in a transparent bucket and measure the nitrogen gas that flows into the cylinder. Researchers showed that the maximum error of the liquid and gas superficial velocities calculation is $\pm 3\%$ and $\pm 5\%$, respectively. Considering that the error of liquid and gas velocities and the change of room temperature during experiments (no more than 15°C) exist, the maximum error of calculated dimensionless numbers is around 10%. Finally, considering an error of $\pm 5\%$ exists in the film thickness measurement, the error of disturbance wave height measurement is approximately $\pm 10\%$. It is worth noting that measurements were repeated at least three times and the experiments are repeated to ensure repeatability. The standard deviation of the measurement results is less than 0.01 mm. The random uncertainty in the film thickness measurement is estimated to be 0.02 mm.

2.3 Results and discussion

2.3.1 Film thickness

In Fig. 2.8, I present the measurement results obtained by two sensors and the illustration of the corresponding film thickness. Apparently, the base film thickness as defined above can approximately interpret the thickness of the liquid film from the inner tube wall to the wave trough and the maximum film thicknesses I defined can represent the distance from the inner tube wall to the wave peak. It should be emphasized here that deviations in the maximum film thickness exist when the threshold is changed. After comparing all the data points, it is shown that the mean deviation in t_{Fbase} is 3.5% and 5.3% when 98.5% and 99.5% are selected as the threshold, respectively. However, the comparison shows that there is no obvious relationship observed between the deviation and flow conditions. Consequently, the deviation in H is 5.6% and 8.3% when the threshold is 98.5% and 99.5%, respectively.

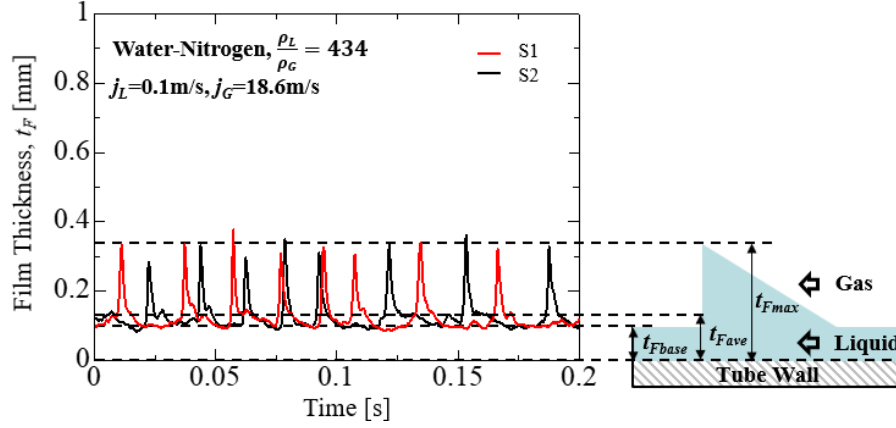


Fig. 2.8 Measurement of film thickness over time and the schematic illustration of the corresponding t_{Fbase} , t_{Fave} , and t_{Fmax} .

The comparison of the average film thickness under different density ratios, surface tension, and liquid superficial velocities is shown in Fig. 2.9. To examine the effect of the superficial gas velocity j_G , superficial liquid velocity j_L , density ratio, and surface tension on the average film thickness, the measured average film thickness is plotted against the superficial gas velocity in Fig. 2.9 (a). The figures on the left and right correspond to the superficial liquid velocities of 0.1 and 0.8 m/s, respectively. The average film thickness decreases as the superficial gas velocity increases under the same density ratio and superficial liquid velocity due to higher drag force. Moreover, the average film thickness increases with an increase in the density ratio under the same gas velocities, attributable to the higher drag force at the interface when the density ratio becomes smaller. However, the average film thickness slightly decreases at high j_L condition since the wave crests are easily sheared off due to the low surface tension.

In Fig. 2.9 (b) and (c), the average film thickness is plotted against the gas Reynolds number, and gas Weber number, respectively, which are defined as follows:

$$Re_G = \frac{\rho_G j_G D}{\mu_g}, \quad (2.4)$$

$$We_G = \frac{\rho_G j_G^2 D}{\sigma}, \quad (2.5)$$

where g denotes gravity. The figures show that the average film thickness decreases with an increase in density ratio under the same gas Reynolds number. Notably, when plotted against the gas Weber number, the average film thickness is almost the same as under the same superficial liquid velocity, indicating that the gas Weber number could converge the effect of density ratio on the average film thickness within a wide range of gas-liquid density ratios (32 to 434) even the surface tension varies. It should be noted here that the effect of tube diameter is not examined in current research due to the

limitation of the experimental apparatus. Thus, the dependency of average film thickness on such dimensionless numbers might vary and require more experimental investigation to evaluate.

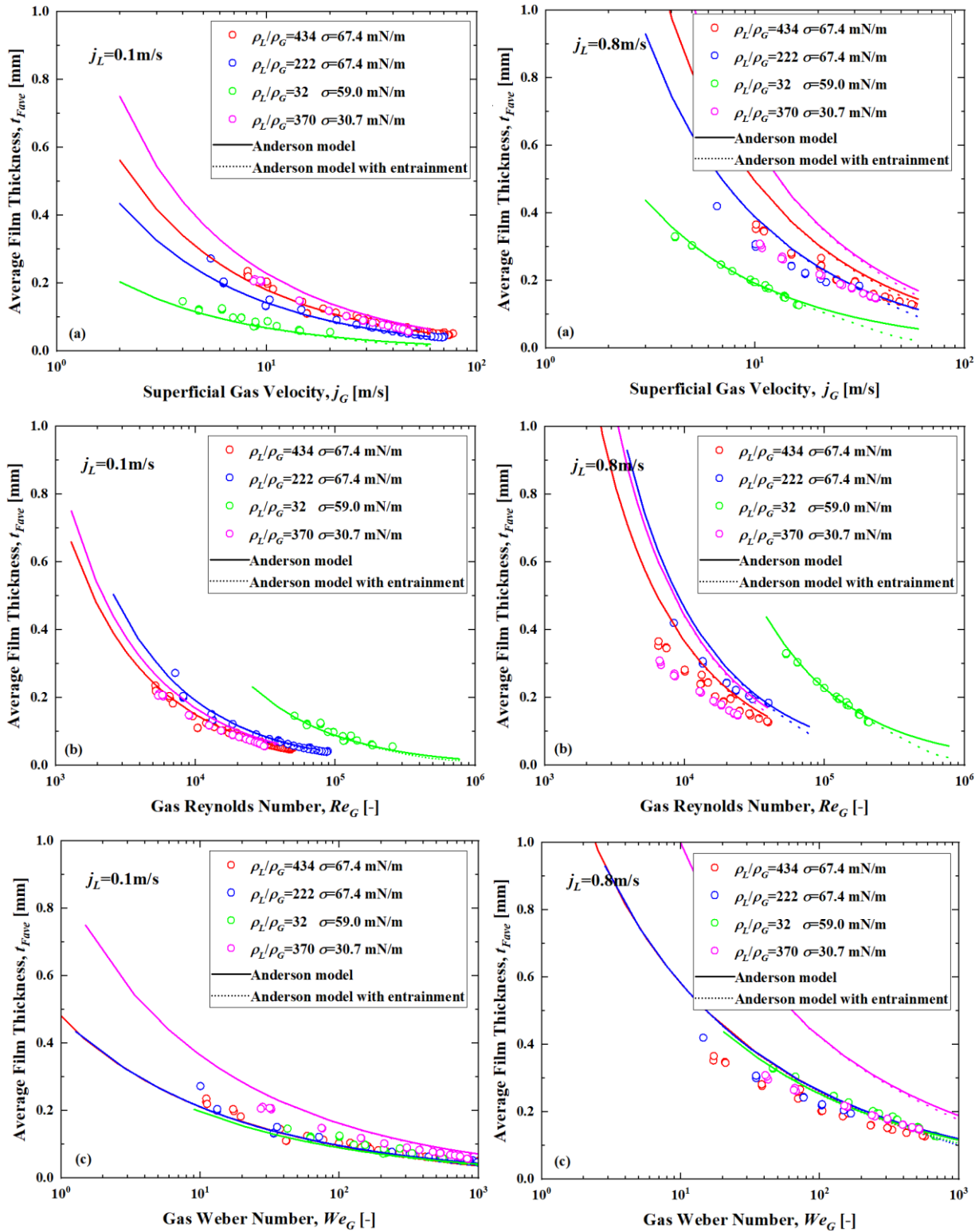


Fig. 2.9 Comparison of average film thickness under different experimental conditions when plotted against (a) j_G , (b) Re_G , (c) We_G ; the figures on the left side and right side correspond to the $j_L = 0.1$ and 0.8 m/s, respectively.

To predict the average film thickness, I employed a model based on the work of Anderson and Mantzouranis [32]. In this model, the assumption exists that the liquid film velocity, u , follows the universal velocity profile of Von Karman [33], which is expressed in the form of three equations corresponding to three regions in the liquid film velocity profile, as follows:

$$\text{laminar layer: for } y^+ < 5, u^+ = y^+, \quad (2.6)$$

$$\text{buffer layer: } 5 < y^+ < 30, u^+ = -3.05 + 5 \ln y^+, \quad (2.7)$$

$$\text{turbulent layer: for } y^+ > 30, u^+ = 5.5 + 2.5 \ln y^+, \quad (2.8)$$

where u^+ denotes the dimensionless velocity parameter and y^+ denotes the dimensionless film thickness. u^+ and y^+ are calculated as follows:

$$u^+ = \frac{u}{u^*}. \quad (2.9)$$

$$y^+ = \frac{\rho_L u^* y}{\mu_L}. \quad (2.10)$$

where u^* denotes the friction velocity, defined as $u^* = \sqrt{\frac{\tau_w}{\rho_L}}$; μ_L denotes the liquid viscosity, y denotes the distance from the tube wall, and τ_w denotes the wall shear stress. Nonetheless, it is assumed that the τ_w equals the τ_i , due to the very thin liquid film compared with the tube diameter; thus, the τ_w is calculated as $\tau_w = \tau_i = C_{fi} \frac{\rho_G}{2} j_G^2$. The C_{fi} , is obtained from the empirical correlation of Wallis et al. (1969) as $C_{fi} = 0.005(1 + 300 \frac{t_{Fave}}{D})$.

Now, it is possible to calculate the liquid film velocity in each region with knowledge of the velocity profile in the liquid film and the τ_w . The liquid mass flow, W , is calculated by integrating the liquid film velocity over the liquid film cross-sectional area dA as $W = \int \rho_L u dA$, where $dA = 2\pi \left(\frac{D}{2} - y\right) dy$.

Then, the liquid mass flow can be divided into three regions, as mentioned previously, and calculated as follows:

$$\text{laminar layer: for } y^+ < 5, W_l^+ = 12.5 - \frac{125}{3Re^*}, \quad (2.11)$$

$$\text{buffer layer: } 5 < y^+ < 30, W_b^+ = \frac{1}{2Re^*} (5.55 - 5 \ln y^+) y^{+2} + (5 \ln y^+ - 8.05) y^+, \quad (2.12)$$

$$\text{turbulent layer: for } y^+ > 30, W_t^+ = \frac{1}{2Re^*} (4.25 - 2.5 \ln y^+) y^{+2} + (2.5 \ln y^+ + 3) y^+. \quad (2.13)$$

where $Re^* = \frac{D\rho_L u_*}{2\mu_L}$, and $W = \pi D\mu_L W^+$. Then, the total liquid mass flow is obtained by $W = W_l + W_b + W_t$. Notably, this calculated liquid mass flow should be roughly equal to the measured liquid mass flow. Hence, given only the experimental conditions, such as j_G and j_L , the average film thickness is calculated without any experimental data at all.

Because liquid droplets could be entrained in the gas core and affect the liquid film thickness, the entrainment fraction should be considered in the model. A droplet entrainment correlation proposed by Sawant et al. [34], which has been examined by several researchers [35,36] and shows a satisfying prediction, is introduced as follows:

$$E = \left(1 - \frac{Re_{fflim}}{Re_L}\right) \tan(2.31 \times 10^{-4} Re_L^{-0.35} We_G''^{-1.25}), \quad (2.14)$$

$$Re_L = \frac{\rho_L j_G D}{\mu_L}, \quad (2.15)$$

$$Re_{fflim} = 250 \ln(Re_L) - 1265, \quad (2.16)$$

$$We_G'' = \frac{\rho_G j_G^2 D}{\sigma} \left(\frac{\rho_L - \rho_G}{\rho_G}\right)^{1/4}, \quad (2.17)$$

where E denotes the entrainment fraction, Re_L denotes the liquid Reynolds number, Re_{fflim} denotes the limiting liquid film Reynolds number, and We_G'' denotes the modified gas Weber number.

In Fig. 2.9, the average film thickness calculated from Anderson's model with and without entrainment consideration from Sawant et al. [34] is shown as the dotted and solid lines, respectively. Similar to the measured average film thickness, the average film thickness curves obtained from Anderson's model under different density ratios but similar surface tension collapse onto a single curve when plotted against the gas Weber number. However, under higher superficial liquid velocity or lower surface tension conditions, Anderson's model overpredicts the average film thickness although the droplet entrainment is considered. This fact could be interpreted by the underestimation of the C_{fi} at high superficial liquid velocity and low surface tension conditions when using the Wallis correlation and coincides with the findings of Wang et al. [23]. Recently, several researchers derived correlations for predicting the C_{fi} . Belt et al. [37] improved the Wallis correlation to predict the C_{fi} based on the physical analysis, as follows:

$$C_{fi} = 2 \left(1.158 \frac{t_{Fave}}{D} + 3.413 \times 10^{-4}\right). \quad (2.18)$$

Based on the theoretical analysis of experimental data, Ju et al. [38] correlated the C_{fi} using a group of dimensionless numbers, as follows:

$$C_{fi} = 0.0028 + 4.28We_L^{0.28}We_G''^{-0.53}N_{\mu L}^{0.25}. \quad (2.19)$$

where We_L denotes the liquid Weber number, and $N_{\mu L}$ denotes the liquid viscosity number. They are, respectively, defined as follows:

$$We_L = \frac{\rho_L j_L^2 D}{\sigma}, \quad (2.20)$$

$$N_{\mu L} = \frac{\mu_L}{\sqrt{\rho_L \sigma \sqrt{\frac{\sigma}{g \Delta \rho}}}}. \quad (2.21)$$

The correlations of C_{fi} from Belt et al. [37] and Ju et al. [38] are employed in Anderson's model to predict the average film thickness. The normalized predicted average film thickness, defined by the average film thickness divided by the tube diameter, with respect to different C_{fi} correlations under the consideration of entrainment is compared (Fig. 2.10). Clearly, these two correlations can be employed to predict the normalized average film thickness of most data within a deviation of 30%.

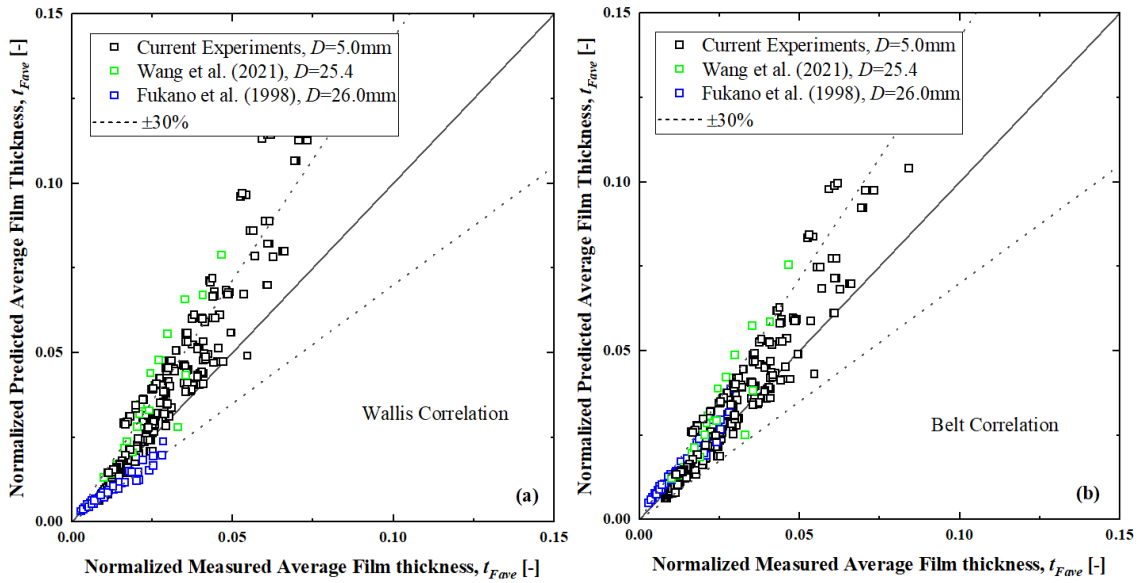


Fig. 2.10 The comparison of normalized predicted average film thickness corresponding to the C_{fi} from the correlation of (a) Wallis, (b) Ju, and (c) Belt.

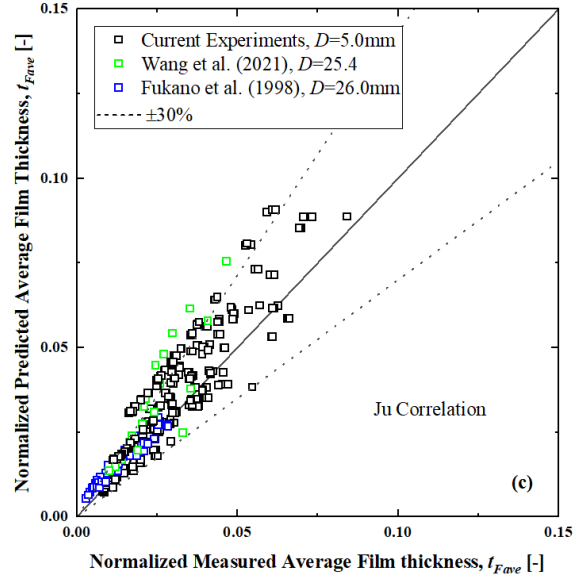


Fig. 2.10 (Continued)

However, this method of predicting average film thickness can be cumbersome and difficult. Thus, in the following section, to predict the average film thickness, another easy-to-use model established through theoretical and experimental analysis is provided.

In Anderson's model, the dimensionless film thickness can be expressed using the gas Weber number, liquid Reynolds and Weber number. Substituting the expressions for the friction velocity, τ_w , C_{fi} , Eq. (2.5), Eq. (2.15), and Eq. (2.20) into Eq. (2.10) and replacing the distance from the tube wall with the tube diameter to simplify the equation under the consideration that the distance from the tube wall is a function of tube diameter, I obtain the following equation:

$$y^+ = \sqrt{0.5C_{fi}Re_L^2We_L^{-1}We_G}. \quad (2.22)$$

This suggests that the dimensionless film thickness should be a function of the gas Weber number, liquid Weber number, and liquid Capillary number. Assuming the dimensionless film thickness equals the normalized average film thickness approximately, multiple regression with the current experimental data is conducted, and the following equation is obtained:

$$\frac{t_{Fave}}{D} = 0.28Re_L^{-0.14}We_L^{0.25}We_G^{-0.36}. \quad (2.23)$$

To evaluate Eq. (2.23), the normalized average film thickness from the experimental data of current experiments and previous databases of Wang et al. (2021) and Fukano and Furukawa [7] (Table 2.2) with the normalized predicted average film thickness using Eq. (2.23) are compared, as shown in Fig. 2.11. Most normalized average film thickness can be approximately predicted within 20% deviation using this correlation. With the databases from Fukano and Furukawa (1998) and

Wang et al. (2021), the effect of tube diameter is examined while the effect of liquid viscosity is examined by the database of Fukano and Furukawa (1998). Although the effect of density ratio, viscosity, surface tension, and liquid and gas flow rates are covered by these databases, this correlation is determined based on the current experiments empirically and might result in deviations when applied to other conditions; thus, more data are needed to examine the relationship under other condition ranges. However, the investigation will provide guidelines for the prediction of average film thickness.

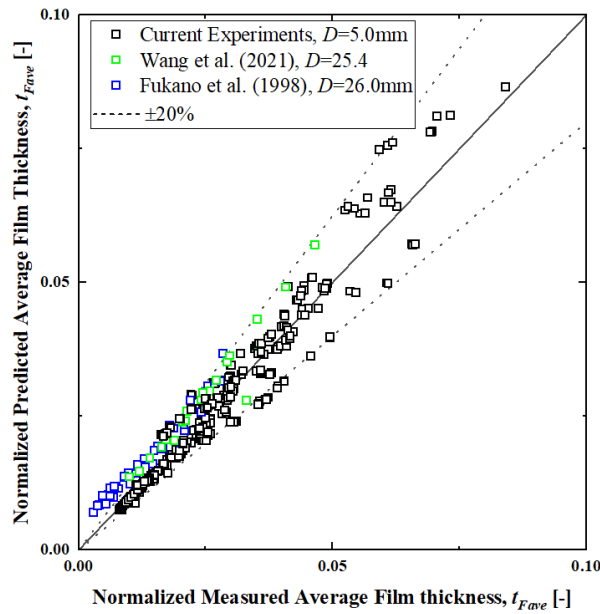


Fig. 2.11 Comparison of normalized measured average film thickness from different databases with normalized predicted average film thickness obtained from Eq. (2.23).

Table 2.1 Summary of experimental conditions of the databases employed in this study.

Reference	Inner diameter (mm)	Superficial liquid velocity range (m/s)	Corresponding data range	Density ratio range
Current experiments	5.0	0.1, 0.4, and 0.8	Nitrogen–Water (0.2 and 0.4 MPa) and HFC134a–Water (0.7 MPa)	32–434

Table 2.1 (continued)

Sawant et al. [11]	9.4	0.05, 0.1, 0.15, 0.3, and 0.54	Air–Water	147–712
			0.12, 0.4, and 0.58 MPa	
Wang et al. [23]	25.4	0.06, 0.15, 0.3, and 0.5	Air–Water Near Atmospheric Pressure	874
Fukano and Furukawa [7]	26.0	0.04, 0.06, and 0.1	Air–Water and wt% Glycerol solution 0.103–0.117 MPa	45 786–876

It has been reported that the base film thickness, average film thickness, and maximum film thickness collapsed onto a single curve under the same liquid flow rate when plotted against the gas Weber number [39,40]. Fig. 2.12 shows the average film thickness, base film thickness, and maximum film thickness plotted against the gas Weber number. The dotted and solid lines correspond to the average film thickness obtained from Anderson's model using the C_{fi} correlation of Belt et al. (2009) with and without entrainment, respectively. The average film thickness is the same under the same liquid Weber number and superficial liquid velocity, which coincides with a previous report from Ju et al. [41].

Although the dependence of average film thickness on the gas Weber number has been described by a few researchers, the dependence of base and maximum film thicknesses on the gas Weber number is barely reported and the effect of surface tension is hardly examined by experimental investigation. As shown in Fig. 2.12, the base and maximum film thicknesses also collapse onto a single curve under the same superficial liquid velocity within the range of error, even though the density ratio and surface tension differ. However, since the range of surface tension in current experimental data has limited variety and the surface tension alternates considerably at high temperatures, especially under BWR operating conditions, more experimental data with various surface tension is needed to verify this tendency.

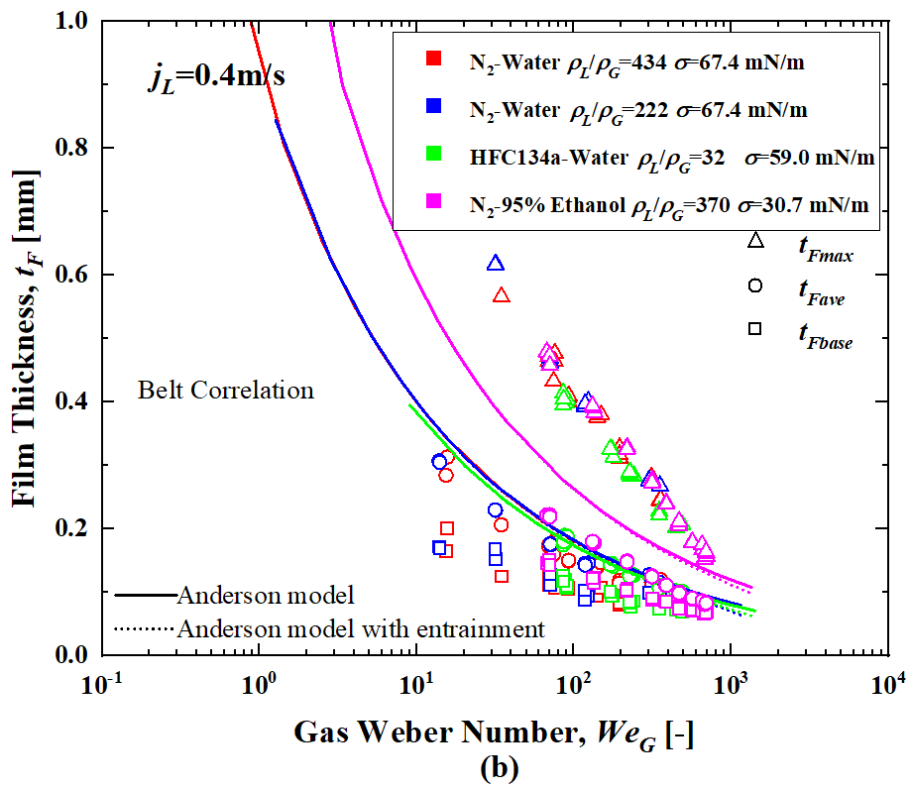
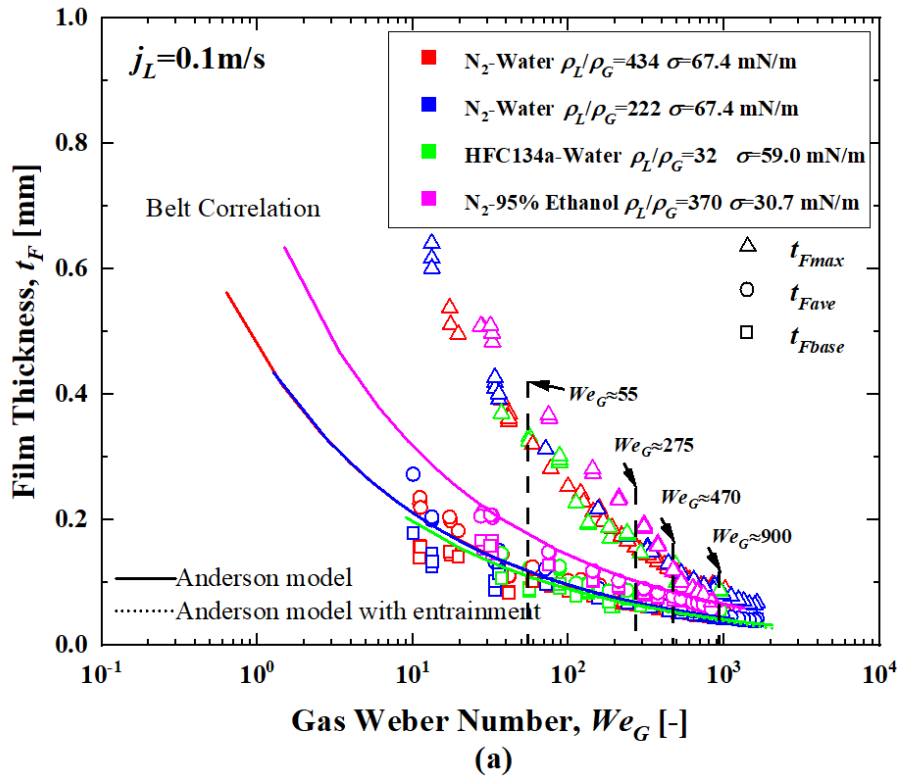


Fig. 2.12 Film thickness measurement results under the superficial liquid velocity of (a) 0.1, (b) 0.4, and (c) 0.8 m/s.

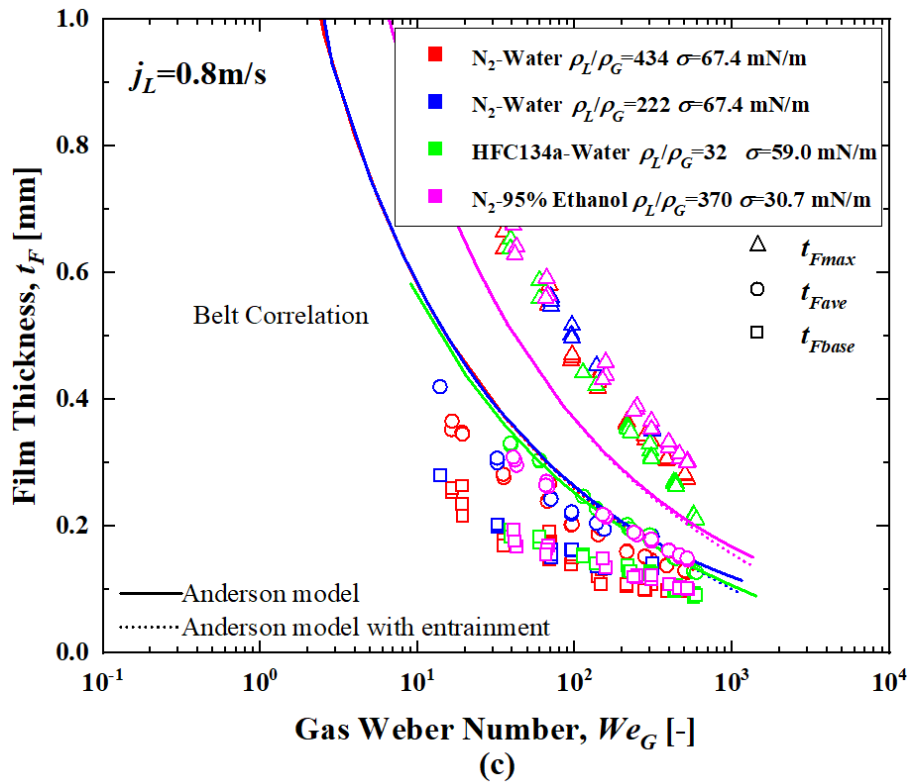


Fig. 2.12 (Continued)

In Fig. 2.13, I present the film thickness time trace measured under the superficial liquid velocity of 0.1 m/s and gas Weber number around 55, 275, 470, and 900, as indicated in Fig. 2. 12(a). The time trace on the left and right sides of the diagram corresponds to the density ratios of 434 and 32, respectively. Interestingly, this figure also shows that for the same value of We in the gas phase, the disturbance wave height and base film thickness are almost the same. Both film thickness and wave height decrease as gas Weber number increases, irrespective of density ratio and surface tension. This observation confirms the relationship between film thickness and gas Weber number as shown in Fig. 2. 13. The above phenomena are most likely to be attributable to the enhanced drag force due to increased gas velocity. On one hand, a larger drag force induces larger shear stress at the gas–liquid interface, which increases the liquid film velocity. As a result, both the film thickness and wave height decrease because the liquid flow rate is constant. Conversely, higher τ_i tends to deform the gas–liquid interface because the retaining force cannot maintain the interface shape. This causes the liquid to be sheared off from the liquid film and entrained in the gas core as droplets. Consequently, film thickness and wave height decrease as the Weber number increases.

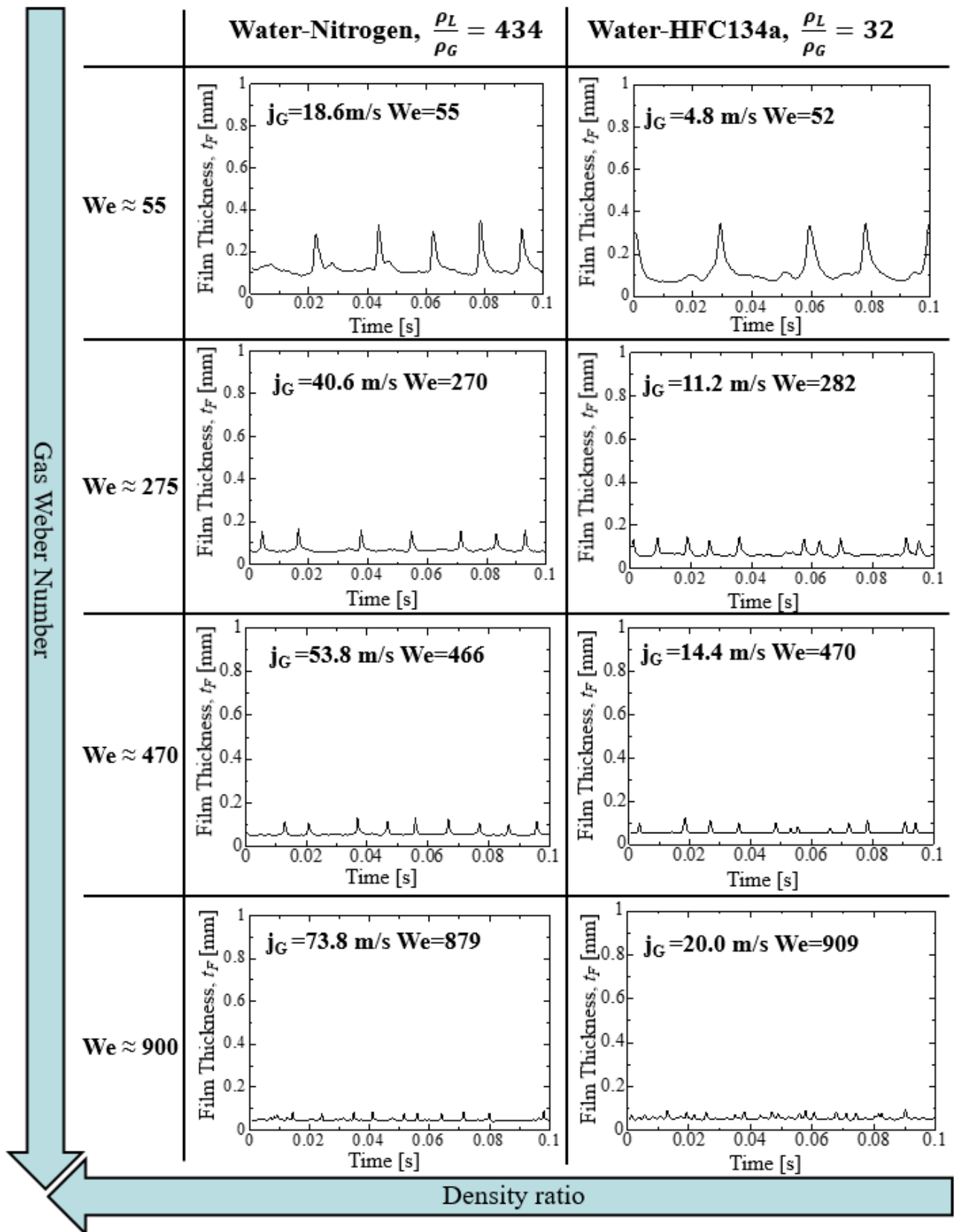


Fig. 2.13 Comparison of film thickness time trace under a superficial liquid velocity of 0.1 m/s and density ratios of 434 and 32 with the gas Weber numbers of 55, 275, 470, and 900.

2.3.2 Disturbance wave height

The disturbance wave height is plotted against the gas Weber number Fig. 2.14. Similar to the film thickness, the wave height collapses onto a single curve when plotted against the gas Weber number even when the gas-liquid density ratio, which simulates high-pressure condition, is very small ($\rho_L/\rho_G = 32$), and surface tension is changed. Sawant et al. (2008a) reported that the wave height shows a similar tendency in annular flows in an air–water system at the pressures of 0.12, 0.4, and 0.58 MPa with a density ratio between 147 and 712, indicating that the gas Weber number could reveal the effect of density ratio on the wave height. The results confirm the observation of Sawant et al. (2008a) and suggest that the single unifying relationship between wave height and gas Weber number still exists when the surface tension is changed and the density ratio is as low as 32 which is close to the density ratio in the BWR operating condition.

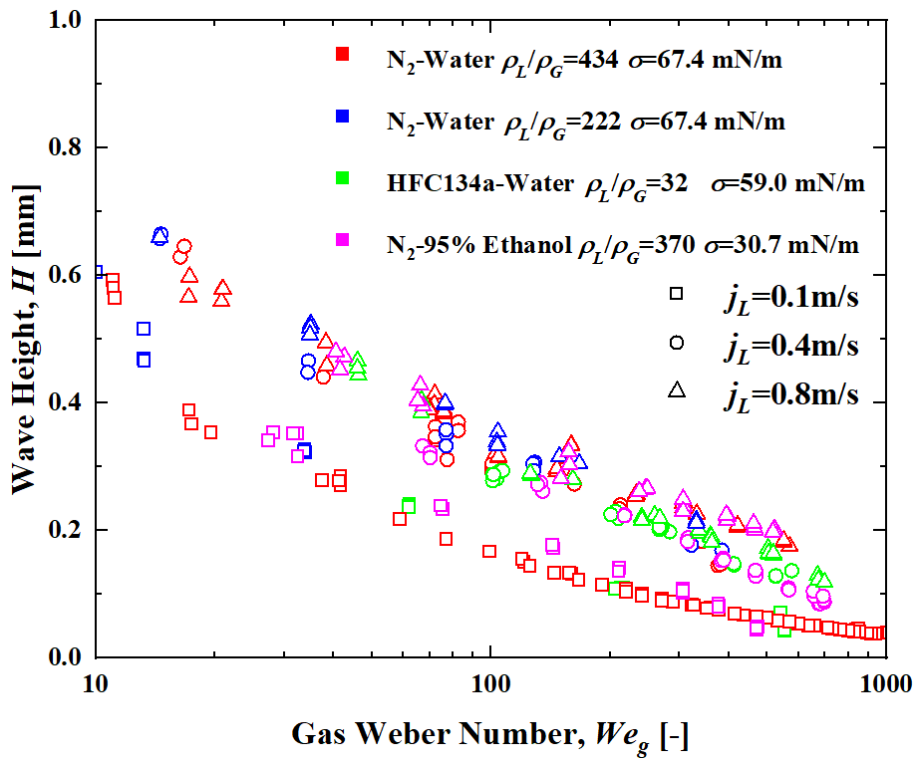


Fig. 2.14 Comparison of disturbance wave height against gas Weber number.

To predict the wave height, I propose a simple model based on Ishii's analysis of the force balance between drag force and surface tension force that acts on the wave crest [5]. The drag force tends to deform the interface, whereas the surface tension force tends to maintain the interface. As shown in Fig. 2.14, the drag force F_d and the surface tension force F_σ act on the wave crest, and I assume that

they are equal. Then, I have the following equation:

$$\frac{1}{2}C_D\rho_G(j_G - v_w)^2A_{DW} = \sigma\pi(D - 2t_{Fbase}), \quad (2.24)$$

where v_w denotes the velocity of the disturbance wave, A_{DW} denotes the axial projected area of disturbance wave height, and σ denotes the surface tension. The left- and right-hand sides of Eq. (2.24) represent the drag force given in terms of the drag coefficient C_D and surface tension force, respectively. Considering $j_G \gg v_w$ and $t_{Fbase} \ll D$, the wave height H is obtained from Eq. (2.24) as a function of C_D and gas Weber number, as follows:

$$H = \frac{1}{2}D\left(1 - \sqrt{1 - \frac{8}{C_D We_G}}\right). \quad (2.25)$$

Notably, this wave height model can satisfactorily explain the phenomenon that wave height is a function of gas Weber number, as shown in Fig. 2.15.

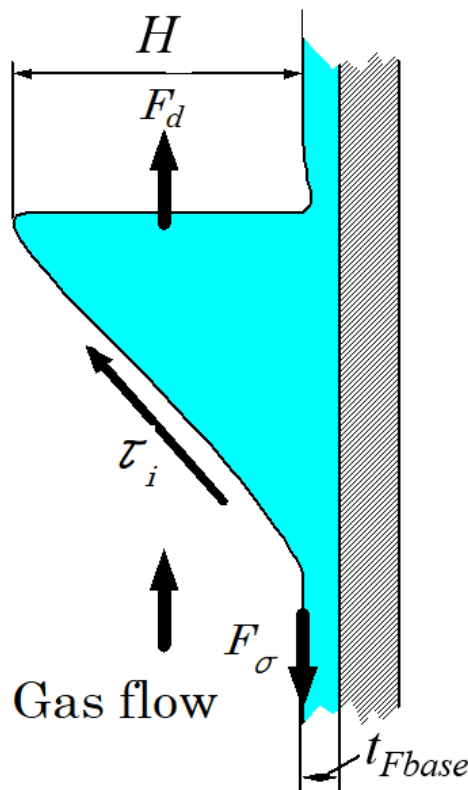


Fig. 2.15 Schematic illustration of force balance on disturbance wave.

Based on current experimental data, correlation of drag coefficient is proposed:

$$C_D = 6.7We_L^{-0.15}We_G^{-0.55}. \quad (2.26)$$

The correlation is determined by multiple regression, and the dimensionless numbers in the

correlation are decided based on the following considerations. As shown in the experimental results, the disturbance wave height is a function of gas Weber number under the same superficial liquid velocity. Therefore, the gas Weber number is employed in the correlation. However, as discussed above, the single unifying relationship between the wave height and gas Weber number differs under different liquid flow rates. Therefore, another parameter that counts the effect of working liquid is required to predict the wave height. After the multiple regression analysis, it is found that the wave height can be predicted better with gas Weber number along with liquid Weber number, as defined in Eq. (2.19), than other dimensionless number groups. This agrees with the former study by Ju et al. (2015) that the gas and liquid Weber numbers are used to predict wave height. As a result, the liquid Weber number is employed as the second parameter. It is worth noting that both C_D and C_{fi} in Eq. (2.19) are empirical parameters. However, C_D could differ from C_{fi} since C_D is correlated to describe the drag force while C_{fi} is used to describe the interfacial shear stress. Meanwhile, the current experiment does not contain the effect of the viscosity; hence, further study is needed to examine the applicability of the correlation when fluids exhibit various viscosities.

After substituting the correlation of drag coefficient into Eq. (2.26), I obtain the function of wave height, as follows:

$$H = \frac{1}{2}D \left(1 - \sqrt{1 - \frac{8}{6.7We_L^{-0.15}We_G^{0.45}}} \right). \quad (2.27)$$

Fig. 2.16 shows the plot of the wave height obtained from the current experimental data against $We_L^{-0.15}We_G^{0.45}$. The wave height approximately collapses onto a single curve irrespective of the density ratio, surface tension, and superficial liquid velocity. The comparison of the current wave height data with the predicted wave height obtained from Eq. (2.27) is shown in Fig. 2.17. It is readily apparent that the correlation predicts the experimental disturbance wave height data within $\pm 20\%$ deviation.

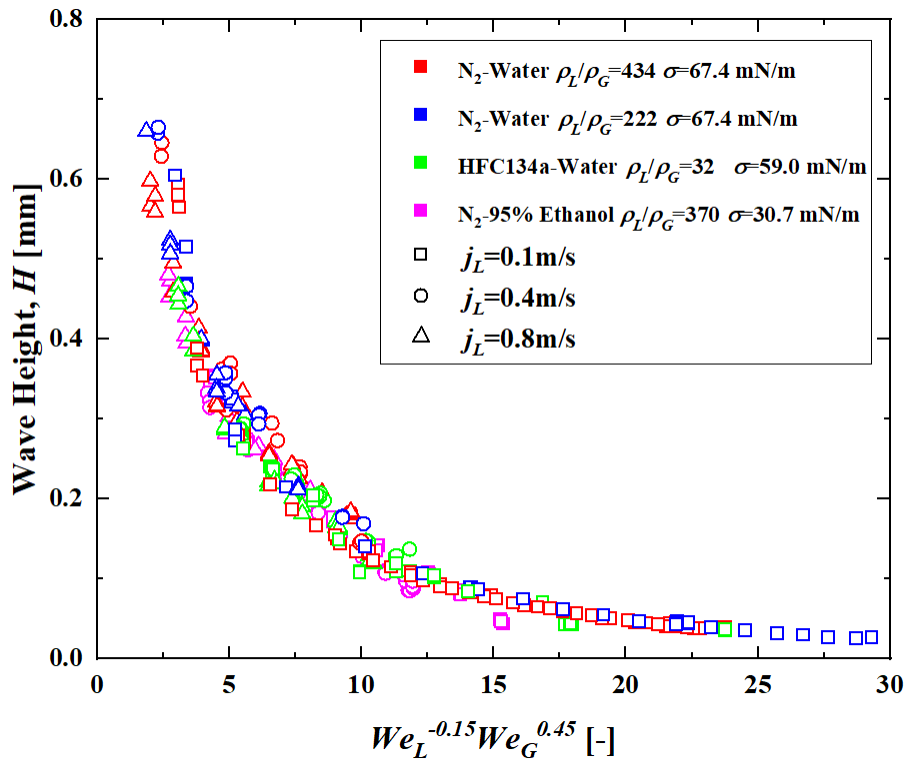


Fig. 2.16 Effect of liquid Weber number and gas Weber number on wave height for different density ratios and superficial liquid velocity.

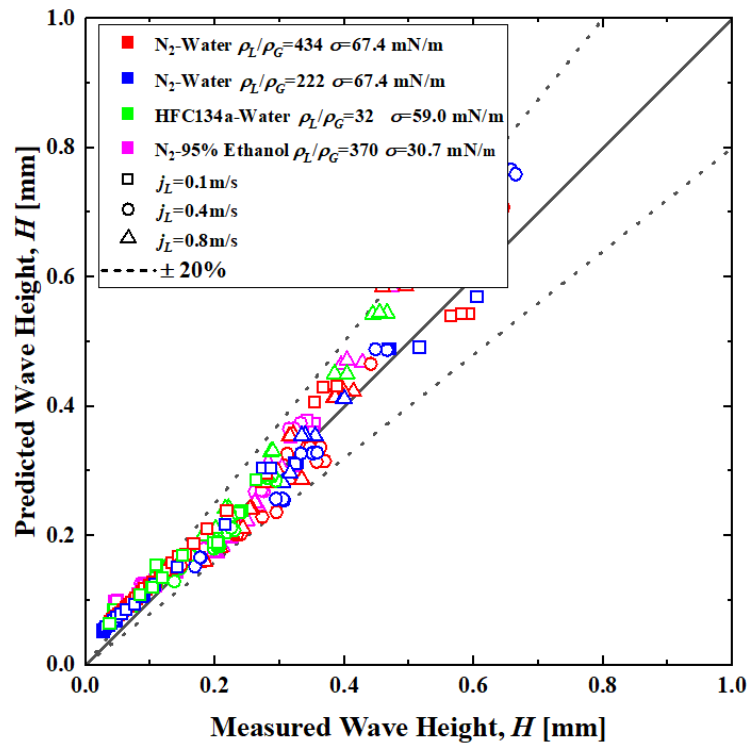


Fig. 2.17 Comparison of measured wave height with predicted wave height.

2.3.3 Comparison of the current model with previous databases

The normalized wave height, which is defined as the wave height divided by the tube diameter, from four databases by Sawant et al. (2008a), Wang et al. (2021), and Fukano and Furukawa (1998), is plotted against $We_L^{-0.15}We_G^{0.45}$ (Fig. 2.17). The experimental conditions are summarized in Table 2. 2. A wide range of superficial gas velocity, superficial liquid velocity, density ratio, and tube diameter is included in these databases; hence, the influence of these factors on the wave height could be examined by the current model. Fig. 2.19 shows the plot of the normalized measured wave height against normalized predicted wave height with the current experimental data and previous four databases. It is readily apparent that the current model can satisfactorily predict the disturbance wave height from previous experimental databases within $\pm 20\%$ deviation. However, considering the current experiments are conducted with a tube of 5.0 mm inner diameter, the effect of tube diameter is not investigated and needed to be verified by more investigation.

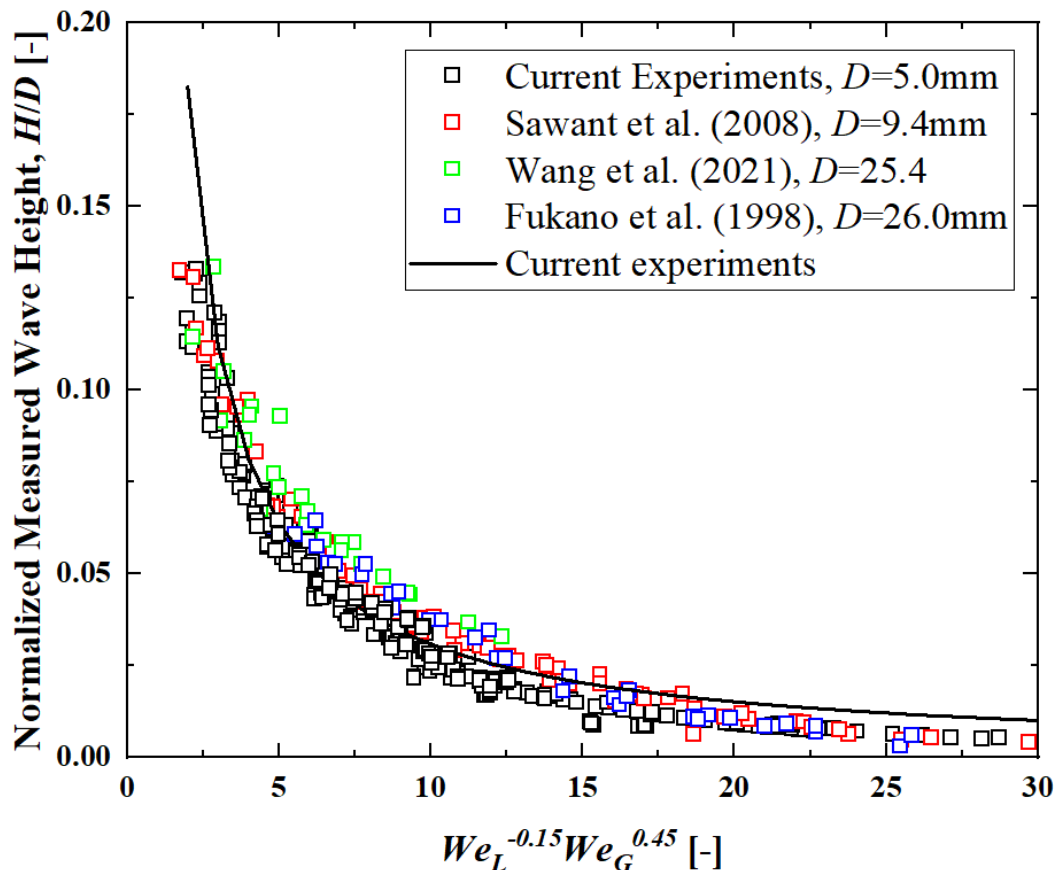


Fig. 2.18 Effect of liquid and gas Weber numbers on normalized wave height from different databases for different density ratios and superficial liquid velocity.

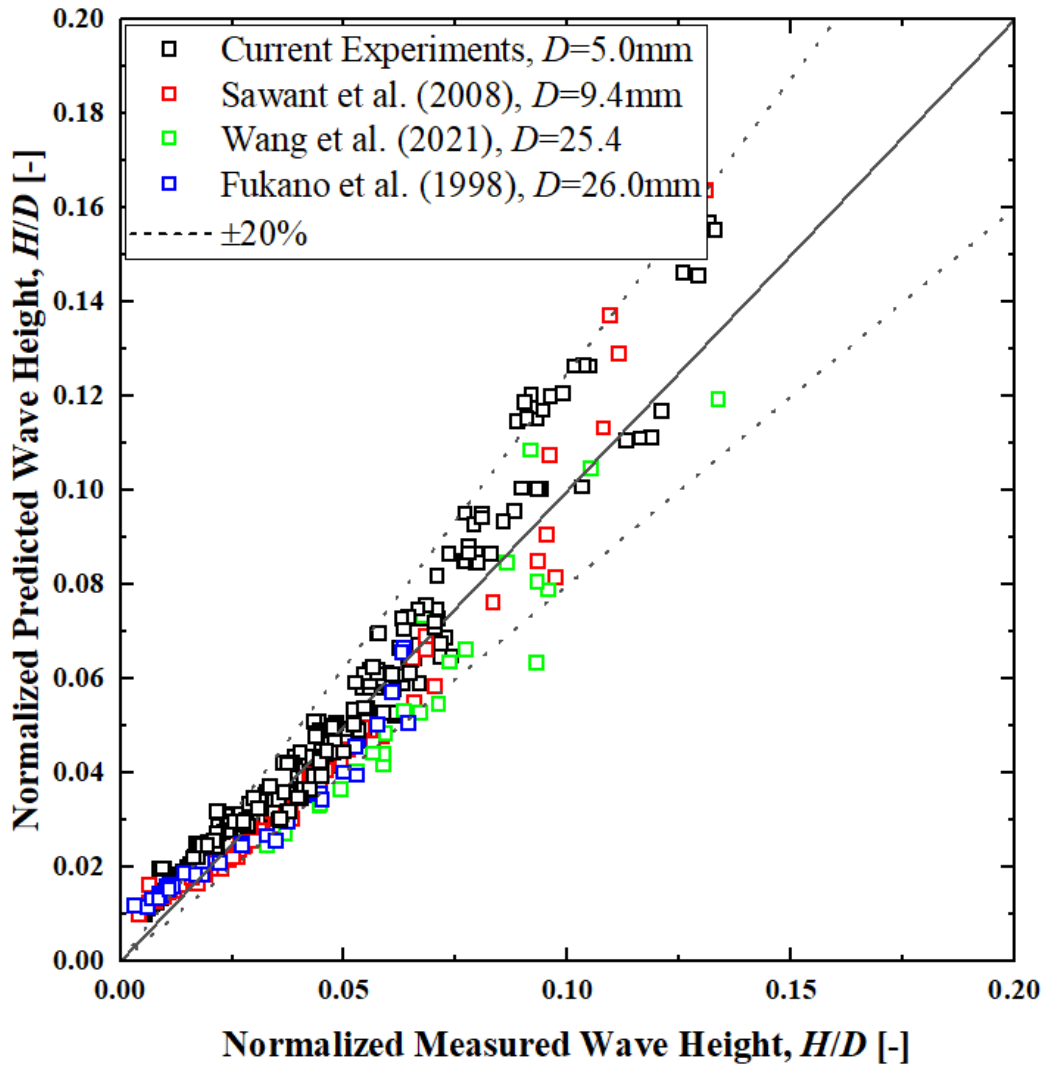


Fig. 2.19 Comparison of normalized measured wave height from different databases with normalized predicted wave height.

2.4 Conclusions

Comprehensive investigation of film thickness and disturbance wave height under low gas–liquid density ratio is crucial in industrial applications, whereas existing studies are either based on high gas–liquid density ratio or lack the focus on the density ratio. In this study, the experiments of nitrogen–water, HFC134a–water annular, and nitrogen–95% aqueous ethanol solution flows with the gas–liquid density ratio between 32 and 434 are performed. The effect of surface tension is examined by altering the working liquids from water to 95% aqueous ethanol solution. The film thickness and disturbance wave height are obtained from the experimental results and numerically investigated. In summary, the major findings of this study are as follows.

1. The base film thickness, average film thickness, maximum film thickness, and wave height are found to be the same when plotted with the gas Weber number under the same liquid flow rate condition. This could be interpreted by the fact that the gas Weber number includes the effect of drag force of the gas phase and the surface tension force, which codetermine the shape of the interface.
2. A theoretical model based on Von Karman's universal velocity profile and Anderson's model considering the droplet entrainment is developed to predict the average film thickness. In addition, through the analytical investigation and multiple regression, another easy-to-use model expressed in terms of dimensionless numbers is proposed for the average film thickness prediction. Both models are evaluated by previous databases. Finally, when plotted with gas Weber number, the average, base, and maximum film thicknesses each is the same under the same gas Weber number and liquid flow rate regardless of density ratio and surface tension.
3. Further data analysis of the disturbance wave height reveals that it tends to collapse onto a single curve when plotted against a group of dimensionless numbers, $We_L^{-0.15}We_G^{0.45}$. Then, to estimate the disturbance wave height, I propose another simple theoretical model based on Ishii's study, which can explain the dependence of wave height on gas Weber number. Three previous databases are employed to evaluate the proposed model, and the model can predict the wave height satisfactorily within the error range.

References

- [1] J.M. Le Corre, Experimental characterization of boiling two-phase flow structures under BWR core operating conditions, *Nucl. Eng. Des.* 365 (2020). <https://doi.org/10.1016/j.nucengdes.2020.110708>.
- [2] A. Sandá, S.L. Moya, L. Valenzuela, Modelling and simulation tools for direct steam generation in parabolic-trough solar collectors: A review, *Renew. Sustain. Energy Rev.* 113 (2019) 109226. <https://doi.org/10.1016/j.rser.2019.06.033>.
- [3] S. Mori, D. Matsushita, T. Fukano, Characteristics of the disturbance wave and the base film in vertical upward boiling annular flow, *Nihon Kikai Gakkai Ronbunshu B Hen Transactions Jpn. Soc. Mech. Eng. Part B.* 72 (2006) 2723–2732. <https://doi.org/10.1299/kikaib.72.2723>.
- [4] S. Mori, T. Fukano, Relation between the occurrence of Burnout and differential pressure fluctuation characteristics caused by the disturbance waves passing by a flow obstacle in a vertical boiling two-phase upward flow in a narrow annular channel, *Nucl. Eng. Des.* 236 (2006) 985–992. <https://doi.org/10.1016/j.nucengdes.2005.09.005>.
- [5] M. Ishii, M.A. Grolmes, Inception criteria for droplet entrainment in two-phase concurrent film flow, *AIChE J.* 21 (1975) 308–318. <https://doi.org/10.1002/aic.690210212>.
- [6] W.H. Henstock, T.J. Hanratty, The interfacial drag and the height of the wall layer in annular flows, *AIChE J.* 22 (1976) 990–1000. <https://doi.org/10.1002/aic.690220607>.
- [7] T. Fukano, T. Furukawa, Prediction of the effects of liquid viscosity on interfacial shear stress and frictional pressure drop in vertical upward gas-liquid annular flow, *Int. J. Multiph. Flow.* 24 (1998) 587–603. [https://doi.org/10.1016/S0301-9322\(97\)00070-0](https://doi.org/10.1016/S0301-9322(97)00070-0).
- [8] R. Kumar, M. Gottmann, K.R. Sridhar, Film thickness and wave velocity measurements in a vertical duct, *J. Fluids Eng. Trans. ASME.* 124 (2002) 634–642. <https://doi.org/10.1115/1.1493808>.
- [9] H. Han, Z. Zhu, K. Gabriel, A study on the effect of gas flow rate on the wave characteristics in two-phase gas-liquid annular flow, *Nucl. Eng. Des.* 236 (2006) 2580–2588. <https://doi.org/10.1016/j.nucengdes.2006.03.015>.
- [10] T. Hazuku, T. Takamasa, Y. Matsumoto, Experimental study on axial development of liquid film in vertical upward annular two-phase flow, *Int. J. Multiph. Flow.* 34 (2008) 111–127. <https://doi.org/10.1016/j.ijmultiphaseflow.2007.10.008>.
- [11] P. Sawant, M. Ishii, T. Hazuku, T. Takamasa, M. Mori, Properties of disturbance waves in vertical annular two-phase flow, *Nucl. Eng. Des.* 238 (2008) 3528–3541. <https://doi.org/10.1016/j.nucengdes.2008.06.013>.
- [12] C. Berna, A. Escrivá, J.L. Muñoz-Cobo, L.E. Herranz, Review of droplet entrainment in

annular flow: Interfacial waves and onset of entrainment, *Prog. Nucl. Energy.* 74 (2014) 14–43. <https://doi.org/10.1016/j.pnucene.2014.01.018>.

[13] Barry Azzopardi, Disturbance wave frequencies, velocities and spacing in vertical annular two-phase flow, *Nucl. Eng. Des.* 92 (1986) 121–133.

[14] K. Sekoguchi, M. Takeishi, Interfacial structures in upward huge wave flow and annular flow regimes, *Int. J. Multiph. Flow.* 15 (1989) 295–305. [https://doi.org/10.1016/0301-9322\(89\)90002-5](https://doi.org/10.1016/0301-9322(89)90002-5).

[15] A. Al-Sarkhi, C. Sarica, K. Magrini, Inclination effects on wave characteristics in annular gas-liquid flows, *AIChE J.* 58 (2012) 1018–1029. <https://doi.org/10.1002/aic.12653>.

[16] T. Arai, M. Furuya, T. Kanai, K. Shirakawa, Concurrent upward liquid slug dynamics on both surfaces of annular channel acquired with liquid film sensor, *Exp. Therm. Fluid Sci.* 60 (2015) 337–345. <https://doi.org/10.1016/j.expthermflusci.2014.05.018>.

[17] S. V. Alekseenko, A. V. Cherdantsev, M. V. Cherdantsev, S. V. Isaenkov, D.M. Markovich, Study of formation and development of disturbance waves in annular gas-liquid flow, *Int. J. Multiph. Flow.* 77 (2015) 65–75. <https://doi.org/10.1016/j.ijmultiphaseflow.2015.08.007>.

[18] J. Vasques, A. Cherdantsev, M. Cherdantsev, S. Isaenkov, D. Hann, Comparison of disturbance wave parameters with flow orientation in vertical annular gas-liquid flows in a small pipe, *Exp. Therm. Fluid Sci.* 97 (2018) 484–501. <https://doi.org/10.1016/j.expthermflusci.2018.03.020>.

[19] N.B. Vargaftik, *Handbook of physical properties of liquids and gases-pure substances and mixtures*, (1975).

[20] I. Kataoka, M. Ishii, *Mechanism and correlation of droplet entrainment and deposition in annular two-phase flow.*, United States, 1982.

[21] G.F. Hewitt, *Annular two-phase flow*, Elsevier, 2013.

[22] Z. Dang, G. Wang, M. Ishii, Two-phase interfacial structure of bubbly-to-slug transition flows in a 12.7 mm ID vertical tube, *Int. J. Heat Mass Transf.* 165 (2021) 1–10. <https://doi.org/10.1016/j.ijheatmasstransfer.2020.120556>.

[23] G. Wang, Z. Dang, M. Ishii, Wave structure and velocity in vertical upward annular two-phase flow, *Exp. Therm. Fluid Sci.* 120 (2021). <https://doi.org/10.1016/j.expthermflusci.2020.110205>.

[24] L.M. Pan, H. He, P. Ju, T. Hibiki, M. Ishii, Experimental study and modeling of disturbance wave height of vertical annular flow, *Int. J. Heat Mass Transf.* 89 (2015) 165–175. <https://doi.org/10.1016/j.ijheatmasstransfer.2015.05.073>.

[25] Y. Zhao, C.N. Markides, O.K. Matar, G.F. Hewitt, Disturbance wave development in two-phase gas-liquid upwards vertical annular flow, *Int. J. Multiph. Flow.* 55 (2013) 111–129. <https://doi.org/10.1016/j.ijmultiphaseflow.2013.04.001>.

- [26] R. Lin, K. Wang, L. Liu, Y. Zhang, S. Dong, Study on the characteristics of interfacial waves in annular flow by image analysis, *Chem. Eng. Sci.* 212 (2020) 115336. <https://doi.org/10.1016/j.ces.2019.115336>.
- [27] T. Fukano, Measurement of time varying thickness of liquid film flowing with high speed gas flow by a constant electric current method (CECM), *Nucl. Eng. Des.* 184 (1998) 363–377. [https://doi.org/10.1016/S0029-5493\(98\)00209-X](https://doi.org/10.1016/S0029-5493(98)00209-X).
- [28] A. Wolf, S. Jayanti, G.F. Hewitt, Flow development in vertical annular flow, *Chem. Eng. Sci.* 56 (2001) 3221–3235. [https://doi.org/10.1016/S0009-2509\(00\)00546-7](https://doi.org/10.1016/S0009-2509(00)00546-7).
- [29] S. V. Isaenkov, A. V. Cherdantsev, I.S. Vozhakov, M. V. Cherdantsev, D.G. Arkhipov, D.M. Markovich, Study of primary instability of thick liquid films under strong gas shear, *Int. J. Multiph. Flow.* 111 (2019) 62–81. <https://doi.org/10.1016/j.ijmultiphaseflow.2018.11.010>.
- [30] K. Mishima, M. Ishii, Flow Two-Phase Flow in Vertical for Upward Two-Phase Flow In Vertical Tubes, *Int. J. Heat Mass Transf.* 27 (1984) 723–737.
- [31] G.F. Hewitt, D.N. Roberts, Studies of two-phase flow patterns by simultaneous x-ray and flash photography, *Aere-M* 2159. (1969) 28.
- [32] G.H. Anderson, B.G. Mantzouranis, Two-phase (gas-liquid) flow phenomena-I Pressure drop and hold-up for two-phase flow in vertical tubes, *Chem. Eng. Sci.* 12 (1960) 109–126. [https://doi.org/10.1016/0009-2509\(60\)87004-2](https://doi.org/10.1016/0009-2509(60)87004-2).
- [33] T. von Karman, The analogy between fluid friction and heat transfer, *Trans. Am. Soc. Mech. Eng.* 61 (1939) 705–710.
- [34] P. Sawant, M. Ishii, M. Mori, Droplet entrainment correlation in vertical upward co-current annular two-phase flow, *Nucl. Eng. Des.* 238 (2008) 1342–1352. <https://doi.org/10.1016/j.nucengdes.2007.10.005>.
- [35] A. Al-sarkhi, C. Sarica, B. Qureshi, Modeling of droplet entrainment in co-current annular two-phase flow: A new approach, *Int. J. Multiph. Flow.* 39 (2012) 21–28. <https://doi.org/10.1016/j.ijmultiphaseflow.2011.10.008>.
- [36] P. Ju, Y. Liu, X. Yang, M. Ishii, Wave characteristics of vertical upward adiabatic annular flow in pipes, *Int. J. Heat Mass Transf.* 145 (2019) 1–10. <https://doi.org/10.1016/j.ijheatmasstransfer.2019.118701>.
- [37] R.J. Belt, J.M.C. Van't Westende, L.M. Portela, Prediction of the interfacial shear-stress in vertical annular flow, *Int. J. Multiph. Flow.* 35 (2009) 689–697. <https://doi.org/10.1016/j.ijmultiphaseflow.2008.12.003>.
- [38] P. Ju, Y. Liu, C.S. Brooks, M. Ishii, Prediction of interfacial shear stress of vertical upward

adiabatic annular flow in pipes, *Int. J. Heat Mass Transf.* 133 (2019) 500–509.
<https://doi.org/10.1016/j.ijheatmasstransfer.2018.12.057>.

[39] S. Mori, N. Dobata, K. Okuyama, Measurements of liquid film thickness in vertical annular flow composed of HFC134a gas and ethanol liquid, in: 14th Natl. Symp. Power Energy Syst. SPES 2009, Japan, 2009: p. 536.

[40] H. Zhang, T. Hisano, S. Mori, H. Yoshida, Measurement of Liquid Film Thickness for Annular Two-Phase HFC134a Gas-Liquid Ethanol Flow in the Vertical Tube, in: *Int. Conf. Nucl. Eng.*, 2021: p. V004T14A015.

[41] P. Ju, C.S. Brooks, M. Ishii, Y. Liu, T. Hibiki, Film thickness of vertical upward co-current adiabatic flow in pipes, *Int. J. Heat Mass Transf.* 89 (2015) 985–995.
<https://doi.org/10.1016/j.ijheatmasstransfer.2015.06.002>.

CHAPTER 3

Effect of density ratio and surface tension on characteristics of disturbance waves

In this chapter, the characteristics of disturbance waves, including velocity, frequency, wavelength, intermittency, and pitch are comprehensively investigated by conducting gas–liquid upward annular flow experiments in a 5 m m. The film thickness time trace is recorded with respect to time, and the information on disturbance waves is subsequently extracted. The effect of liquid and gas flow rate, density ratio, and surface tension on the disturbance wave is quantitatively analyzed. Different predictive models of the wave velocity are proposed. Physical model for wave frequency prediction is derived on the basis of the mass conservation equation. A simple empirical model with good prediction accuracy of wave frequency is also derived. Compared with existing correlations available in the literature, the newly derived models show better performance under a wide range of flow conditions.

3.1 Introduction

Disturbance waves have received considerable attention because the liquid film between two successive disturbance waves can easily dry out with the existence of heat flux on the wall and disturbance waves move with the liquid supply along the heated wall. Numerous experimental investigations on the disturbance wave characteristics including velocity, wavelength, and frequency have been performed within the past decades. Through conducting air–water annular flow experiments [1], Wolf measured the wave velocity and frequency and revealed that the wave velocity and frequency take a fairly short distance, of the order of 100 diameters, to reach a quasi-steady state when liquid is introduced a porous wall. Kumar measured the wave velocity of the air–water annular flow in a duct using flush-wire conductivity probes [2]. A model for predicting the wave velocity by matching the interfacial shear in the gas and liquid phase was derived. Han investigated the effect of gas flow rate on the characteristics and an average velocity model for the wave and base regions was developed to determine the wave velocity [3]. Sawant conducted air–water annular flow experiments in a 9.4mm inner diameter pipe under different pressure [4]. They reported that only the gas Weber number and liquid phase Reynolds number can satisfactorily predict the dependence of disturbance wave velocity on pressure, liquid and gas flow rate while the wavelength can be described by liquid and gas Reynolds number. They also noted that the correlations available in the literature could not

fully predict the wave velocity in their experimental data. Berna reviewed previous databases and derived a new correlation for predicting wave velocity using gas Reynolds number, liquid Reynolds number [5], and the factor of surface tension defined by Ishii and Grolmes [6]. Ju reviewed experimental data of annular flow available in the literature and derived two correlations for wave velocity from liquid interfacial velocity and interfacial shear stress, respectively [7]. Their correlations showed better performance compared to the other correlations in the literature.

Since the annular flow is a complex phenomenon involving strongly coupled physics, it is difficult to establish a physical model for the wave frequency. Generally, wave frequency is described using the Strouhal number, a dimensionless form of wave frequency while several empirical correlations for the Strouhal number have been established based on experimental data so far. Azzopardi correlated wave frequency data through plotting the Strouhal number against the excess liquid Reynolds number [8]. Sawant derived a new correlation for wave frequency using the Strouhal number, liquid Reynolds number, and density ratio [4]. Based on the experimental results of air–water annular flow in the 76.2mm inner diameter pipe, Al-sarkhi reported that wave frequency strongly depends on the modified Lockhart–Martinelli parameter, and a new correlation was derived [9]. Dasgupta compared the measured wave frequency of air–water annular flow in an 11mm diameter vertical tube with previous correlations [10] and noted that the correlation from Sekoguchi can predict the data within the error of 30% [11]. Based on the experimental investigation, Wang noted that the wave frequency increases with the liquid flow rate and reaches the maximum when the liquid Reynolds number is ca. 6000–8000 [12]. Further increase in liquid flow rate leads to waves with less frequency.

Notably, since the wave pitch and wave intermittency play an important role in the pressure drop models and momentum balance for the annular flow [13,14], they have also been investigated by several researchers. Schubring studied air–water annular flow using a high-speed camera and revealed the relationship between wave pitch, wave intermittency, and flow rate of liquid and gas [15]. Alekseenko measured the wave pitch in the downward annular flow experiments using a high-speed laser-induced fluorescence technique and highlighted that the wave pitch decreased with gas velocity and slightly grow with liquid viscosity and flow rate [16]. Vasques comprehensively studied the properties of disturbance waves using the brightness-based laser-induced fluorescence technique [17]. It is shown that the wave intermittency decreases when the flow rate of the base film increases and its decrease may either be due to a decrease in the wave pitch at low liquid Reynolds numbers or due to an increase in the disturbance wave wavelength. Nevertheless, compared with numerous studies on the film thickness, wave velocity, and wave height, the effect of fluid properties on the wave pitch

and wave intermittency is still not clear.

Although disturbance wave characteristics have been extensively inspected, most experimental investigations available in the literature were conducted by using air and water under nearly atmospheric pressure, whereas the variety of fluid properties was limited. In this chapter, the effect of density ratio and surface tension on velocity, frequency, wavelength, intermittency, and pitch of disturbance waves will be experimentally studied by using nitrogen gas, HFC134a gas, water, and 95% (v/v) aqueous ethanol solution as working fluids under the pressure from 0.2 MPa to 0.7 MPa. New models for wave velocity and frequency will be developed, evaluated with available databases, and compared with previous empirical correlations.

3.2 Experimental apparatus and procedures

In this chapter, the experimental facility for vertical annular flow measurement was the same as it in the Chapter 2. With the time trace measured by the two sensors, the cross-correlation function was used to calculate the time lag between the same disturbance wave recorded by the two sensors successively. Then, the wave velocity, v_w , was calculated by dividing the distance between two sensors by the time lag. A developing length ($L/D = 300$) was achieved to ensure that the measurements corresponded to the fully developed equilibrium annular flow, which is in accordance with the correlation proposed by Kataoka and Ishii [18]. The uncertainty of the velocity measurement was estimated at 10%.

As summarized in Table 1.2, the experimental working fluids in this chapter were the same as those in the previous section. The properties of the working liquid and gas are listed. Gas density, liquid density, surface tension, gas viscosity, and liquid viscosity are denoted as ρ_G , ρ_L , σ , μ_G , and μ_L , respectively. The density of the working liquid was obtained with an electronic scale and measuring cylinder. However, with the help of the A&D SV-10 viscometer with an accuracy of 5% and a Rhesca 5200tn tester with an accuracy of 9%, the dynamic viscosity and surface tension of the working liquid were measured before and after each experiment respectively. The density and dynamic viscosity of the working gas were obtained from the literature [19]. Nitrogen gas under 0.2 and 0.4 MPa and HFC134a gas under 0.7 MPa were used as the working gases. The superficial liquid velocity, denoted by j_L , at the test section was set at 0.1, 0.4, and 0.8 m/s for each pressure condition. All the flows in current experiments were classified as annular flow indicated by the flow maps from Hewitt and Roberts and Mishima and Ishii [20,21] and confirmed by the high-speed camera.

3.3 Results and discussion

3.3.1 Wave velocity

The effects of density ratio and surface tension on the wave velocity at different superficial liquid velocities are shown in Fig. 3.1. It is shown that the wave velocity increases as superficial gas velocity and superficial liquid velocity increase. Moreover, the wave velocity tends to increase as the density ratio decreases under the same j_G and σ , which could be attributed to the increase in the interfacial shear stress when the density ratio decreases. It is worth noting that, from the comparison between red plots (representing data with $\rho_L/\rho_G = 434$ and $\sigma = 67.4 \text{ mN/m}$) and pink plots (representing data with $\rho_L/\rho_G = 370$ and $\sigma = 30.7 \text{ mN/m}$), the difference in wave velocity of most plots is approximately 10% which is comparable to the measurement error. Therefore, it is difficult to determine the exact effect of surface tension on wave velocity based on the current experimental results. Additional research may be necessary to fully understand the underlying mechanisms. An attempt has also been made to bring the wave velocity data closer to each other by plotting the wave velocity against the mass flux and momentum flux of the gas. However, this attempt was not successful.

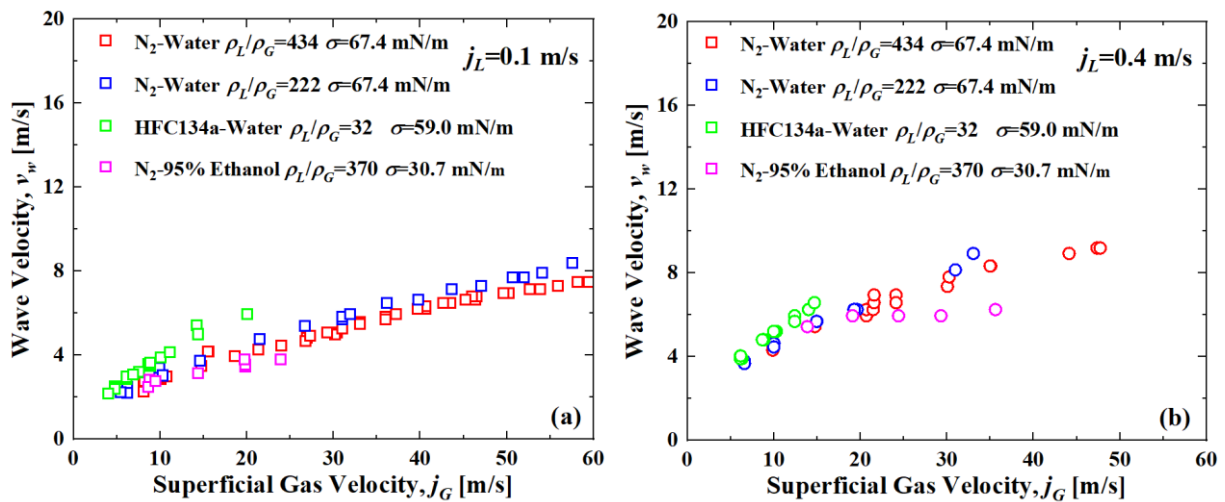


Fig. 3.1 Disturbance wave velocity at the superficial liquid velocities of (a) 0.1, (b) 0.4, and (c) 0.8 m/s.

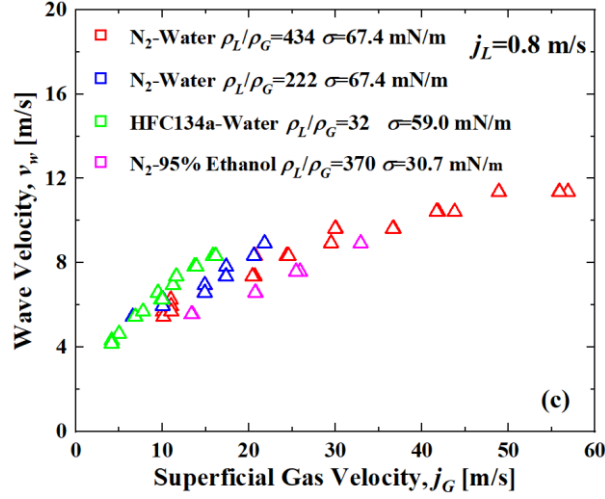


Fig. 3.1 (Continued)

A model based on the balance between wall and gas–liquid interfacial shear stress acting on the liquid film was developed to predict wave velocity. As shown in Fig. 3.2, the model was established on the basis of the assumption that the wall shear stress τ_w is approximately equal to the interfacial shear stress τ_i because the liquid film is considerably thinner than the tube diameter as suggested and evaluated by previous studies [22–24]. Conventionally, wall shear stress and interfacial shear stress can be expressed as

$$\tau_w = \frac{1}{2} C_{fw} \rho_L u_L^2, \quad (3.1)$$

$$\tau_i = \frac{1}{2} C_{fi} \rho_G (j_G - u_L)^2, \quad (3.2)$$

where C_{fw} and C_{fi} are the wall and interfacial friction factors, respectively, and u_L is the average velocity of the liquid film. Here, the gas core is treated as moving with a velocity relative to the liquid film, which is $j_G - u_L$. Then, the relative velocity $j_G - u_L$ is used for computing τ_i considering the gas core as the control volume. The average deviation between j_G and u_L is 16% except experiments of HFC134a-water annular flows. For experiments of HFC134a-water annular flows, the average deviation is 46%. For simplifying the model and predicting the wave velocity by using only easily accessible information, the liquid film is roughly assumed to be flat on the gas–liquid interface with an average film thickness considering that the liquid film is very thin compared with the tube diameter [25].

The velocity profile in the liquid film is complicated due to the nature of turbulent flow and the instability of the gas–liquid interface. However, given that the liquid film is very thin and almost equal shear stresses act on both sides of the liquid film [26,27], the liquid film is assumed as plane-Couette flow. Then, the velocity profile could be symmetric and the liquid interfacial velocity u_i can

be reasonably assumed to be two times the average liquid velocity, i.e., $u_i = 2u_L$. However, this assumption may need more verification by optical observation. Previous reports stated that the interfacial velocity is almost equal to the wave velocity [25,28,29]. Thus, the wave velocity is also close to two times the average liquid velocity, i.e., $v_w \approx 2u_L$. Then, the wave velocity is obtained by combining Eqs. (3.1) and (3.2) in the form of

$$v_w = \frac{2j_G \sqrt{\frac{C_{fi} \rho_G}{C_{fw} \rho_L}}}{\left(1 + \sqrt{\frac{C_{fi} \rho_G}{C_{fw} \rho_L}}\right)}. \quad (3.3)$$

Conventionally, the friction factor is related to the average film thickness as proposed by [30] and widely adopted by later studies [31,32]. Therefore, comparing the friction factor ratio $\frac{C_{fi}}{C_{fw}}$ obtained from Eq. (3.3) using measured wave velocity with the normalized average film thickness, as shown in Fig. 3.3, is interesting. Obviously, the friction factor ratio collapses into a single curve when plotted with the normalized average film thickness irrespective of the density ratio and surface tension. In previous report [33], the normalized average film thickness was expressed by a dimensionless number group that included the liquid Reynolds number, liquid Weber number, and gas Weber number, which are denoted as Re_L , We_L , and We_G , respectively. Therefore, the friction factor ratio should also be related to this dimensionless number group. After employing multiple regression, a correlation for the friction factor group based on the current experimental result is developed as

$$\frac{C_{fi}}{C_{fw}} = 81Re_L^{0.05}We_L^{0.25}We_G^{-0.68}, \quad (3.4)$$

The predictive value of this model was plotted against the current experimental data as shown in Fig. 3.4. The current experimental data are predicted within the $\pm 20\%$ error band. Then, as presented in Table 3.2, multiple databases [9,34–36] were used to examine the developed model and the comparison of the measured and predicted value by Eqs. (3.3) and (3.4) are shown in Fig. 3.5. Although the current model can predict the data of [35] and [37] with good agreement, the data of [36,38] are overestimated.

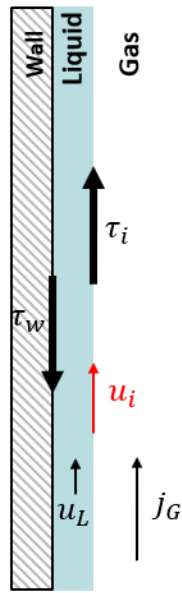


Fig. 3.2 Schematic of wall and interfacial shear stresses acting on the liquid film.

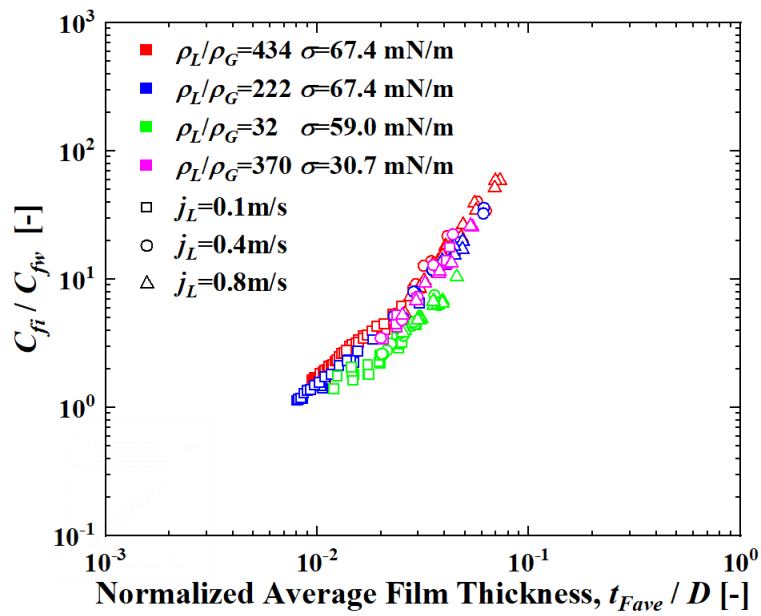


Fig. 3.3 Comparison of the normalized measured average film thickness with the friction factor ratio C_{fw}/C_{fi} .

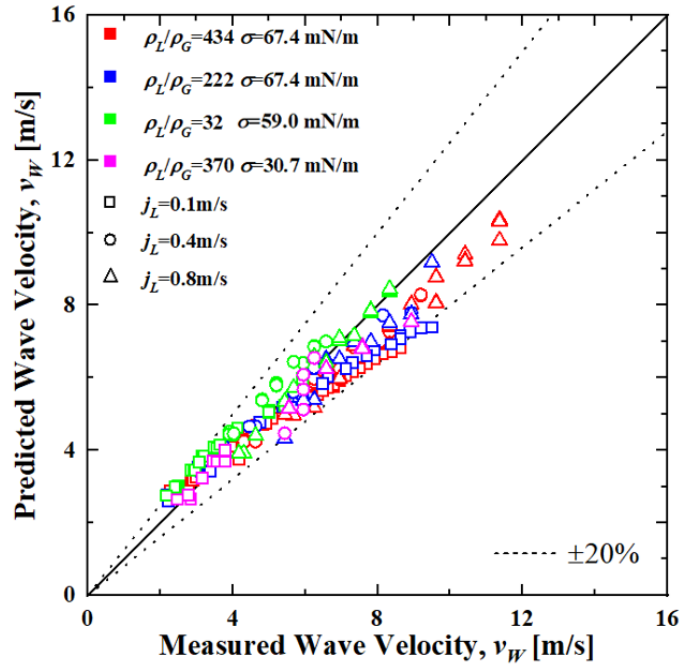


Fig. 3.4 Comparison of the measured wave velocity with the predicted wave velocity.

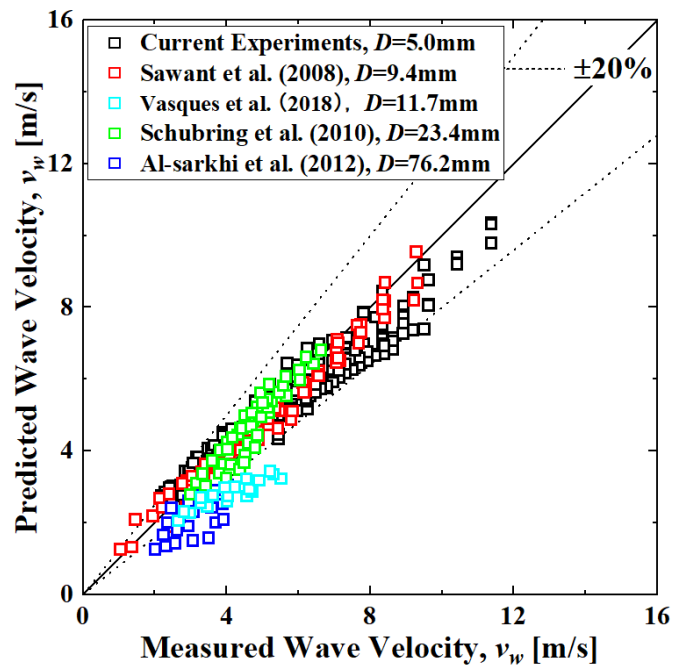


Fig. 3.5 Comparison of the measured wave velocity with the predicted wave velocity when previous databases were employed.

Given that the effect of the pipe diameter on the current correlation is not considered, the current experimental data, along with available previous databases (wherein tube diameter ranges from 5 mm to 76.2 mm), were used to fit the empirical constants as

$$\frac{c_{fi}}{c_{fw}} = 50Re_L^{0.1}We_L^{0.15}We_G^{-0.61}, \quad (3.5)$$

The modified model, which is expressed by Eqs. (3.3) and (3.5), and several existing proposed wave velocity correlations [9,25,29,34,39] summarized in Table 3.3 were evaluated by using the current and previous databases. The comparison between the measured wave velocity and the predicted wave velocity is presented in Fig. 3.6.

Table 3.1 Summary of the experimental conditions of the employed databases.

Reference	Inner diameter (mm)	Superficial liquid velocity range (m/s)	Corresponding data range	Density ratio	Surface tension range (N/m)
Current experiments	5.0	0.1, 0.4, and 0.8	Nitrogen–water (0.2 and 0.4 MPa), nitrogen–95% aqueous ethanol solution (0.2 MPa), and HFC134a–water (0.7 MPa)	32–434	30.7–67.4
Al-sarkhi et al. (2012)	76.2	0.0035, 0.01, 0.02, and 0.04	Air–water atmospheric pressure	near 832	73.0
Sawant et al. (2008)	9.4	0.05, 0.1, 0.15, 0.3, and 0.54	Air–water 0.12, 0.4, and 0.58 MPa	147–712	72.3
Schubring et al. (2010a)	23.4	0.04, 0.06, 0.08, 0.12, 0.15, 0.19, 0.23, 0.27, 0.35, and 0.39	Air–water atmospheric pressure	near 832	73.0
Vasques et al. (2018)	11.7	0.013, 0.021, 0.029, and 0.038	Air–water atmospheric pressure	near 819	73.3

Table 3.2 Previous models of wave velocity.

Reference	Correlation
Al-sarkhi et al. (2012)	$v_W = 1.942j_L X^{*-0.91}$, where $X^* = \sqrt{\frac{\rho_L j_L}{\rho_G j_G}}$
Berna et al. (2014)	$v_W = 50Re_G^{-0.38} Re_L^{0.16} C_W^{-0.13} \frac{\sqrt{\rho_G j_G + \sqrt{\rho_L j_L}}}{\sqrt{\rho_G + \sqrt{\rho_L}}}$ <p>where $C_W = 0.028N_\mu^{-0.8}$ for $N_\mu \leq 1/15$</p> $C_W = 0.025$ for $N_\mu > 1/15$, $N_\mu = \frac{\mu_L}{(\rho_L \sigma \sqrt{\frac{\sigma}{g\Delta\rho}})^{1/2}}$
Ju et al. (2019b)	$v_W = 10.1j_L We_L^{-0.392} We_G''^{0.227}$, where $We_G'' = \frac{\rho_G j_G^2 D}{\sigma} \left(\frac{\Delta\rho}{\rho_G}\right)^{1/4}$
Kumar et al. (2002)	$v_W = \frac{Cj_G + j_L}{1+C}$, where $C = 5.5\left(\frac{\rho_G}{\rho_L}\right)^{1/2} \left(\frac{Re_L}{Re_G}\right)^{1/4}$
Schubring et al. (2010b)	$v_W = 2.55j_G (Re_G \chi)^{-1/3}$, where $\chi = \frac{\rho_G j_G}{\rho_G j_G + \rho_L j_L}$

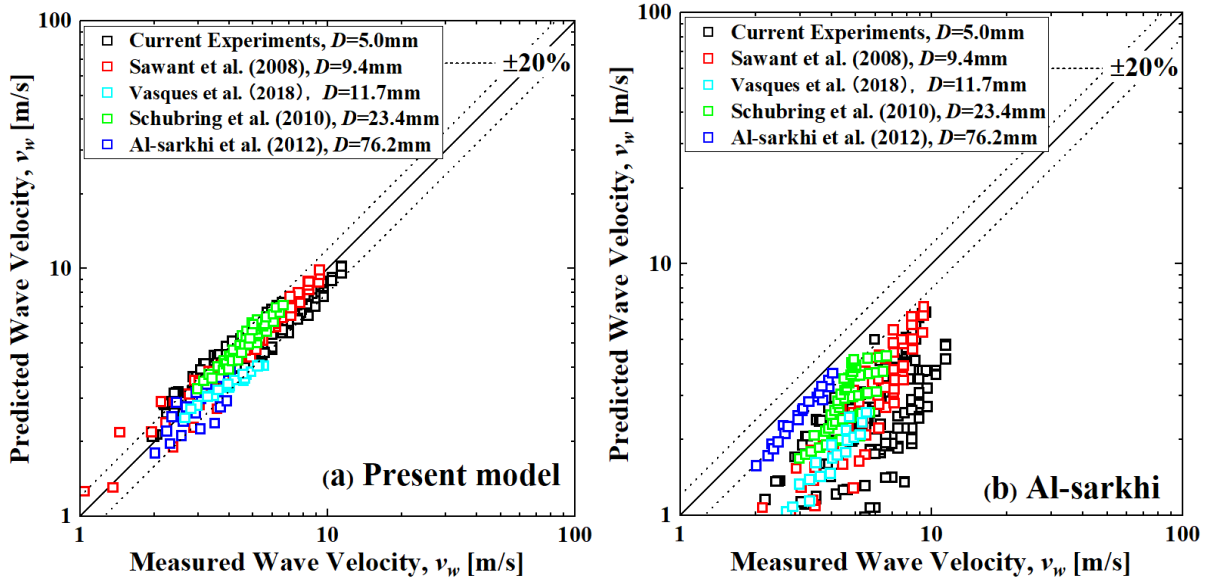


Fig. 3.6 Comparison of measured wave velocities from the database of the current experiments of [35], [36], and [37] and with wave velocity predicted by the correlations of (a) Eqs. (3.3) and (3.5); (b) [38]; (c) [39]; (d) [25]; (e) [29]; and (f) [34].

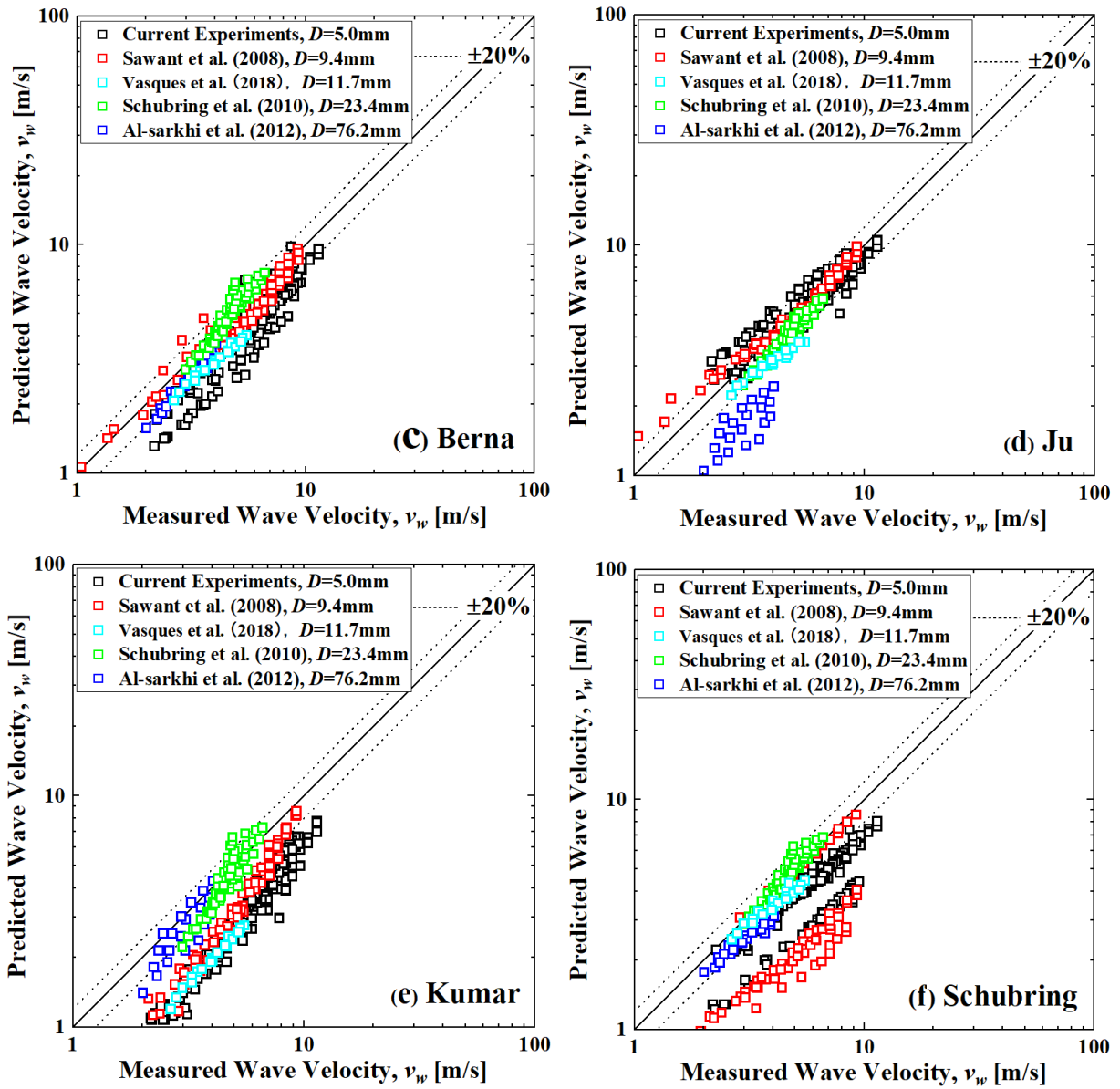


Fig. 3.6 (Continued)

Fig. 3.6 clearly shows that the newly developed model has relatively good performance and can predict most experimental data with a prediction error of less than 20%. Last but not least, the models of Al-Sarkhi, Kumar, and Schubring underestimate the wave velocity of the current experimental data and the experimental data from [35]. An effort has also been made by authors to derive a simpler empirical correlation for v_w by directly linking v_w with various dimensionless numbers in the form of the power function but failed.

3.3.2 Wavelength, wave pitch and intermittency

The shape of the disturbance wave was described using wave height H , pitch L , and wavelength λ as shown in Fig. 3.7. The wave pitch is defined as the longitudinal distance between the two points where the film thickness of the disturbance wave exceeds the base film thickness. The wavelength, denoted by λ , is defined as the spacing between two successive disturbance waves and can be obtained by:

$$\lambda = \frac{v_W}{f} \quad (3.6)$$

Meanwhile, the wave intermittency, INT , is defined as:

$$INT = \frac{L}{\lambda} \quad (3.7)$$

In what follows, more detailed discussions are given of wave pitch, wavelength, and intermittency. It is worth noting that the wave pitch and wavelength discussed in the following section refer to the mean value during the sampling time of each measurement.

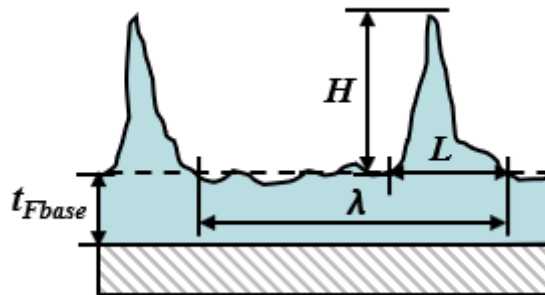


Fig. 3.7 Schematic illustration of the disturbance wave characteristics

Fig. 3.8 shows the dependence of the pitch of the disturbance wave on superficial gas velocity under different flow conditions. The measured wave pitch should refer to the mean value during the sampling time of each measurement. Wave pitch can be observed to decrease with superficial gas velocity, grow weakly with superficial liquid velocity, and increase weakly with decreasing surface tension. This tendency is similar to that previously reported by [49,51]. Meanwhile, wave pitch is found to decrease with the decrease in density ratio. However, the effect of liquid viscosity is barely clear in current experiments since the viscosity varies in limited range and the effect of surface tension or density ratio cannot be neglected when liquid viscosity varies. In view of the similar tendency of wave height observed in previous research [48], wave pitch was plotted against wave height, as

presented in Fig. 3.9. Here, the wave height, H , is defined as the difference between the base and maximum film thickness. The base and maximum film thickness are defined as the film thickness with the highest probability and the film thickness with 99% cumulative probability [48]. In most cases, wave pitch is shown to be roughly proportional to wave height under the same surface tension, density ratio, and superficial gas velocity even though the superficial liquid velocity varies. This finding indicates that a unique relationship should exist between the height and pitch of the disturbance wave to maintain geometric similarity under certain flow conditions.

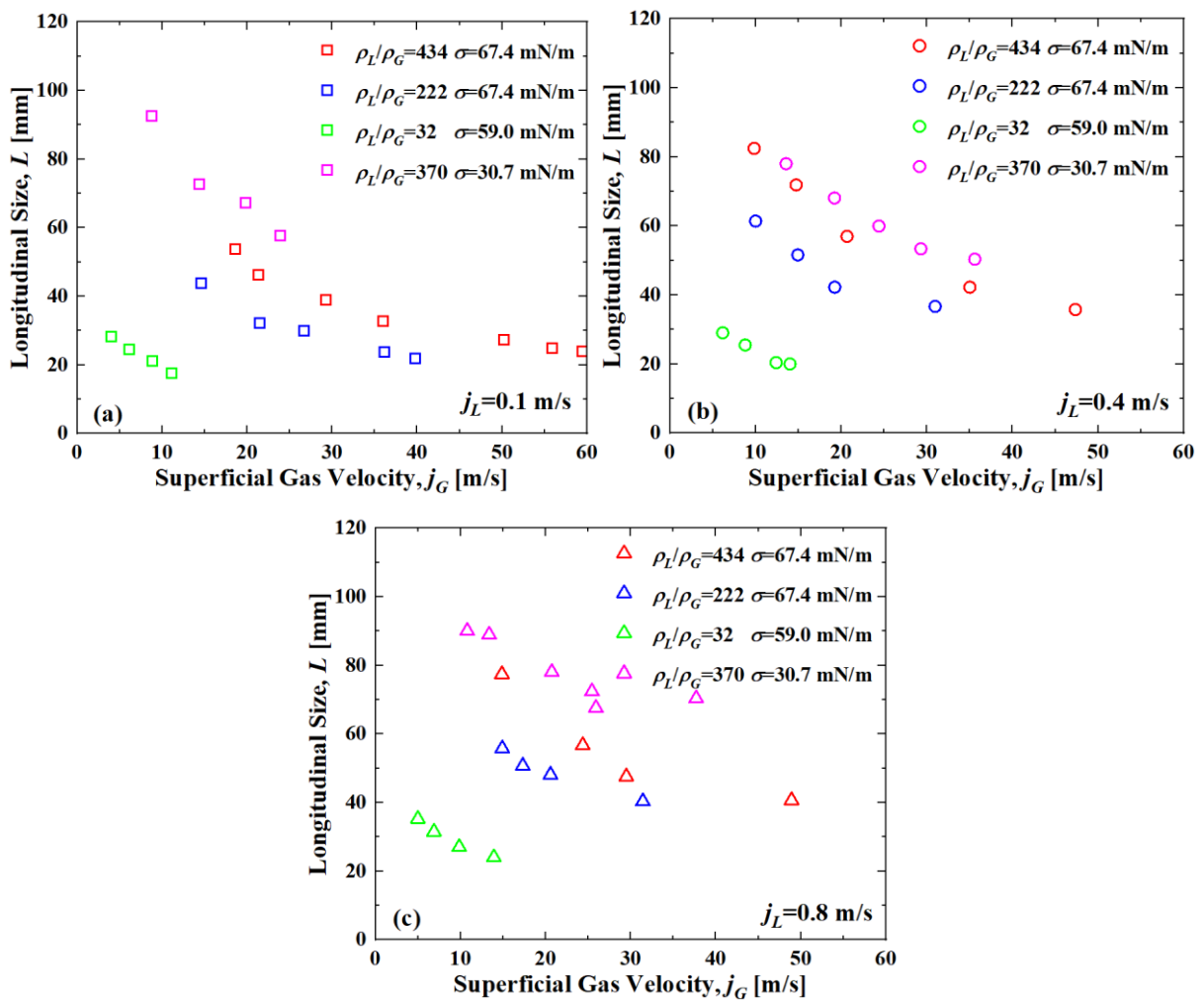


Fig. 3.8 Wave pitch at the superficial liquid velocities of (a) 0.1, (b) 0.4, and (c) 0.8 m/s.

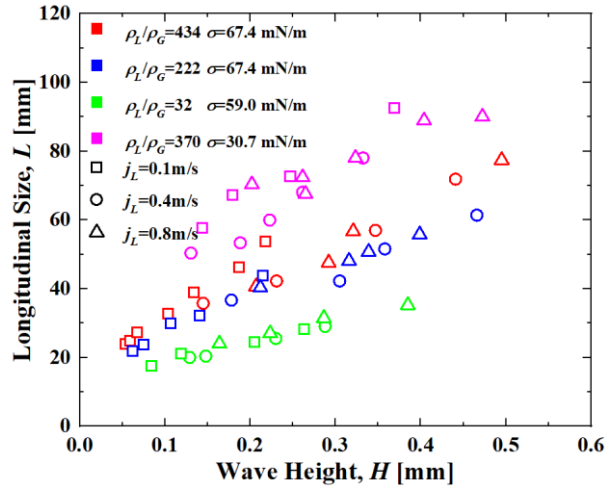


Fig. 3.9 Comparison of wave pitch with the disturbance wave height.

Interestingly, the experimental result shows that the ratio of wave pitch and wave height is close to a single line regardless of flow conditions when plotted against $\frac{\rho_G Re_L}{\rho_L We_G}$ as shown in Fig. 3.10. However, as mentioned above, the viscosity in the current experiments only varies within a limited range and needs to be examined through further investigation.

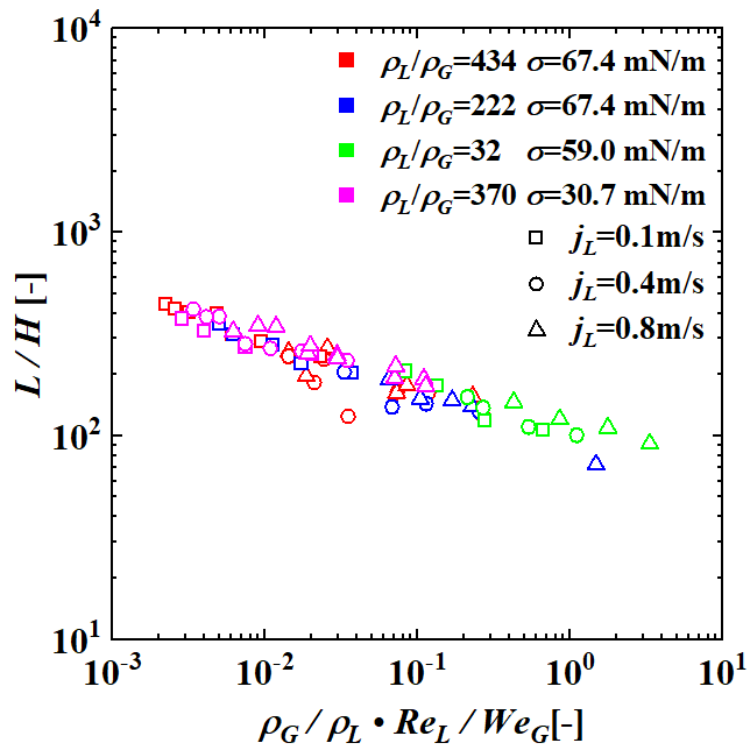


Fig. 3.10 Comparison of the ratio of wave pitch with $\rho_G/\rho_L \cdot Re_L/We_G$.

Based on current experimental data, the ratio of wave pitch and wave height is finally correlated

as:

$$\frac{L}{H} = 115 \left(\frac{\rho_G Re_L}{\rho_L We_G} \right)^{-0.2} \quad (3.8)$$

The comparison of the measured $\frac{L}{H}$ and predicted $\frac{L}{H}$ by Eq. (3.8) is shown in Fig. 3.11. It can be seen that the $\frac{L}{H}$ can be predicted within the error of 25% with Eq. (3.8).

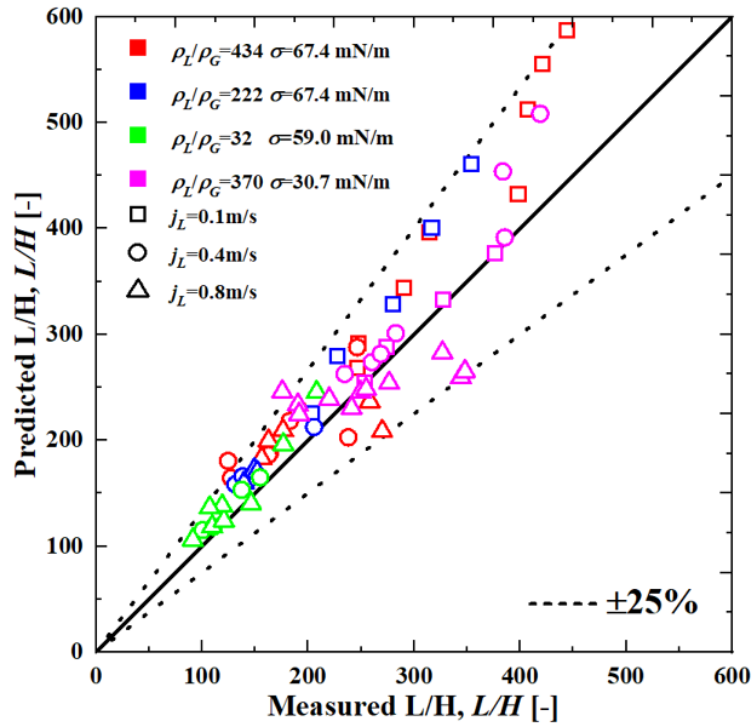


Fig. 3.11 Comparison of measured L/H with predicted L/H from Eq. (3.8).

The wavelength is plotted against the superficial gas velocity as shown in Fig. 3.12. For the effect of superficial gas velocity, the wavelength decreases with the superficial gas velocity. However, when the superficial gas velocity becomes high, the wavelength barely changes. For a fixed superficial gas velocity, it can be seen that the wavelength decreases with the increase of superficial liquid velocity and density ratio. This coincides with the previous study of [54,55]. As for the effect of surface tension, the wavelength increases as surface tension decreases under the j_L of 0.1m/s. When j_L is higher than 0.1m/s, the wavelength only slightly increases with the decrease of surface tension.

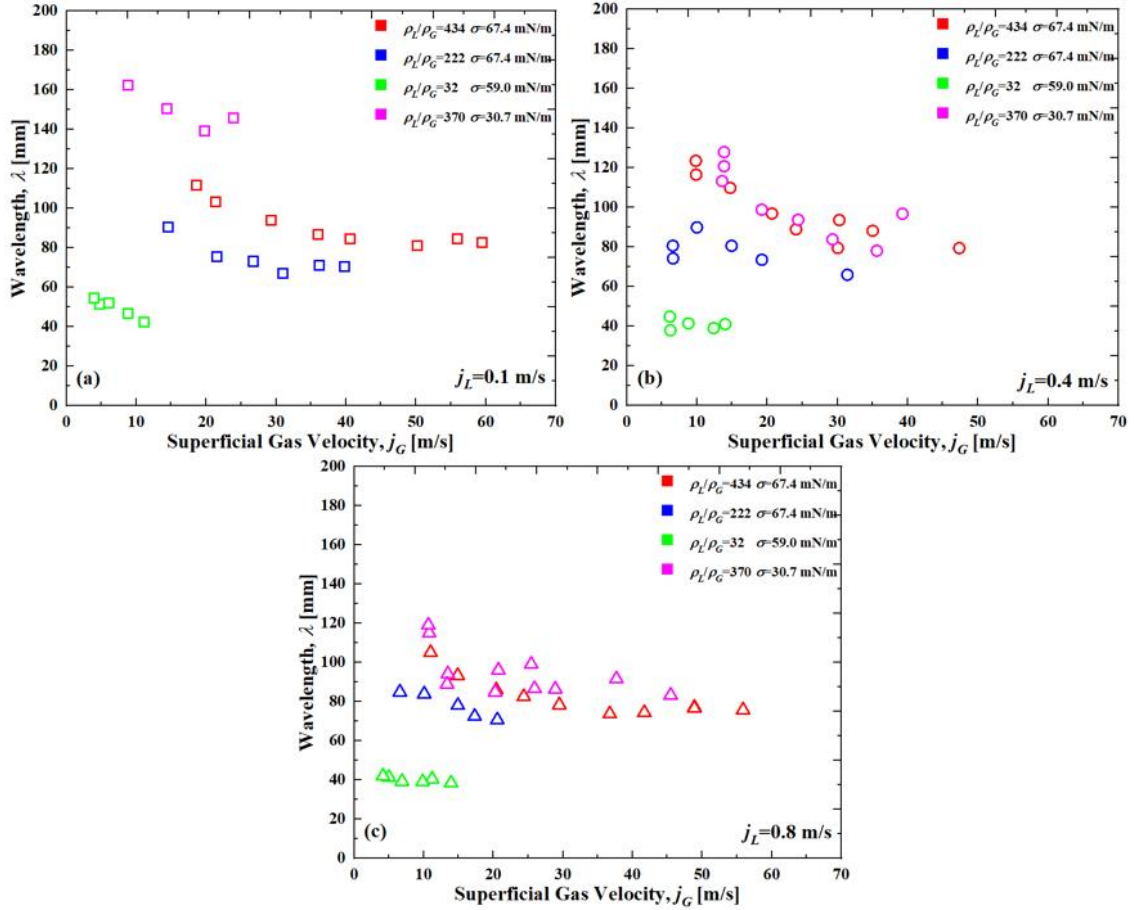


Fig. 3.12 Disturbance wave wavelength under the superficial liquid velocity of (a) 0.1, (b) 0.4, and (c) 0.8 m/s.

The wave intermittency is obtained by Eq. (3.7) and presented in Fig. 3.13. It can be seen that the intermittency increases with decreasing superficial gas velocity and increasing superficial liquid velocity and density ratio. However, the effect of surface tension on the intermittency is practically negligible as reflected in current experimental results.

It has been suggested by [56] and later extended by [57] that the relationship between average film thickness and wavelength should exist. However, it is found that a unique relationship between average film thickness and intermittency, rather than the wavelength, exists based on the current experimental result as shown in Fig. 3.14. It is shown that the intermittency increases as average film thickness increases due to the increase of wave pitch of the decreases of wavelength. Keeping in mind that the average film thickness is a function of Re_L , We_L , and We_G , the intermittency can be expressed by the dimensionless number group based on the current experimental result as:

$$INT = 0.5Re_L^{0.1}We_L^{0.1}We_G^{-0.15} \quad (3.9)$$

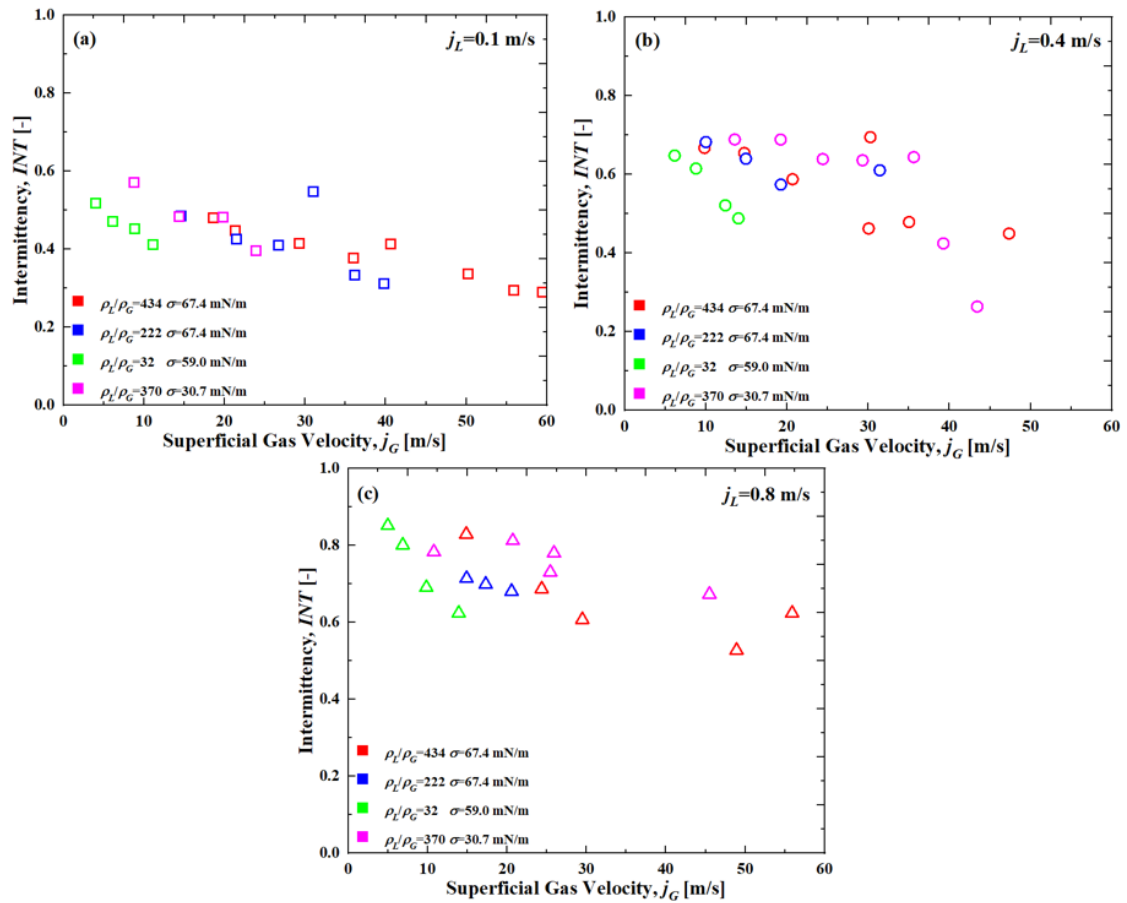


Fig. 3.13 Disturbance wave intermittency under the superficial liquid velocity of (a) 0.1, (b) 0.4, and (c) 0.8 m/s.

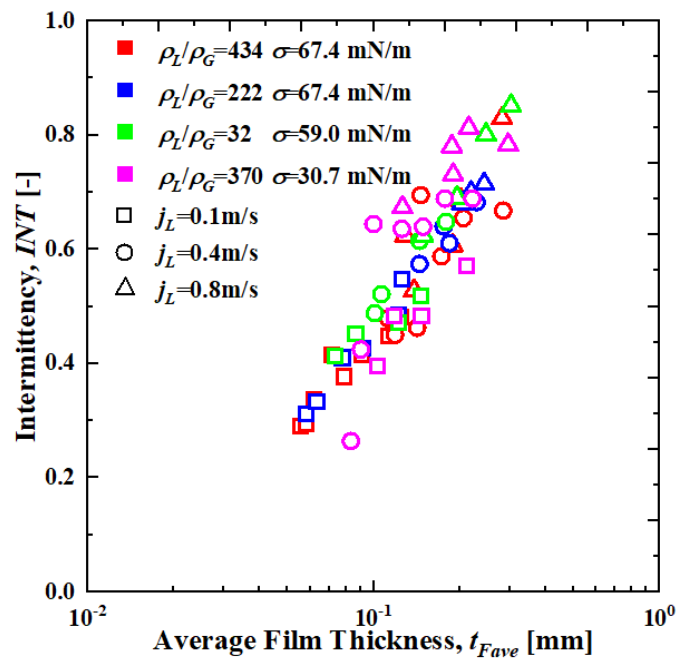


Fig. 3.14 Comparison of the ratio of wave intermittency with average film thickness.

3.3.3 Wave frequency

The measured film thickness time trace for the water–nitrogen system with different j_L and j_G is shown in Fig. 3.15. The dashed line indicates the threshold for the disturbance wave as defined by $t_{Fthr} = t_{Fbase} + \frac{1}{2}(t_{Fmax} - t_{Fbase})$. Meanwhile, the red circle indicates each identified disturbance wave whose local film thickness exceeds t_{Fthr} . The threshold is readily observed to work well with little misidentification. The error of the frequency measurement is estimated at 10% due to the uncertainty in the film thickness measurement [48].

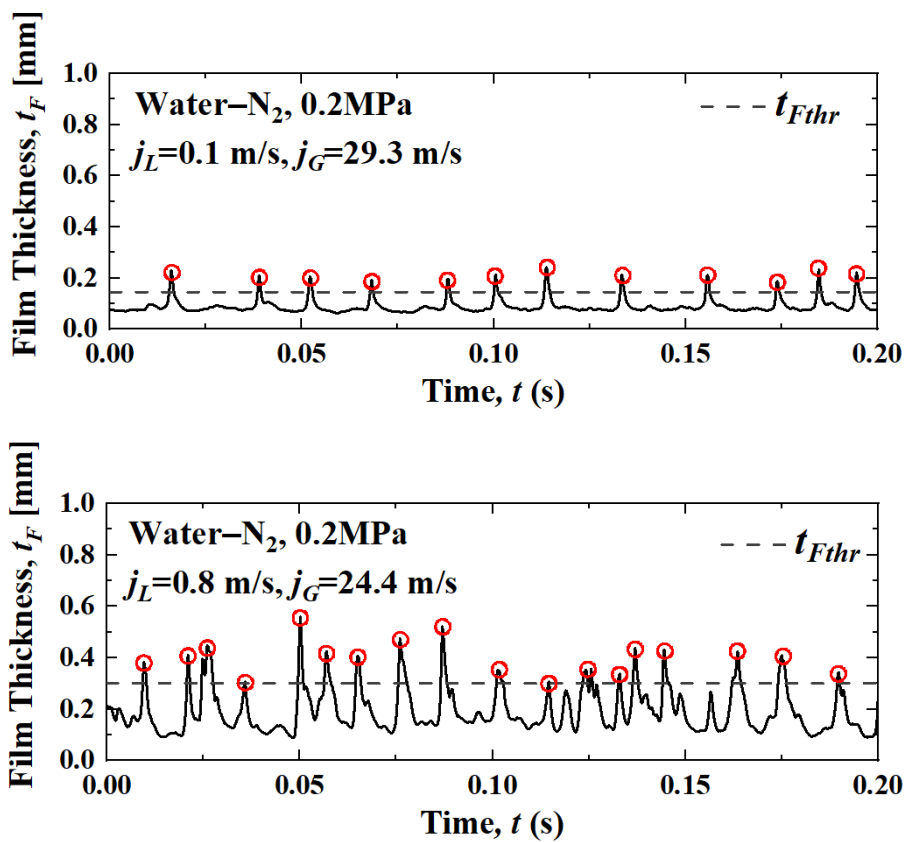


Fig. 3.15 Time trace of the measured film thickness for the water–nitrogen system at different j_L and j_G . The identified disturbance wave is indicated with the red circle.

As shown in Fig. 3.16, the tendency of the experimental data on the wave frequency plotted against superficial gas velocity is comparable with that of the wave velocity. As can be observed from Fig. 3.16, the wave frequency increases with the increase in superficial gas velocity and superficial liquid velocity. Moreover, the wave frequency increases with the decrease in density ratio. This behavior coincides with that previously reported by [50]. Regarding the difference between red and

pink plots, a deviation of around 10% is observed for most plots which is of a similar magnitude to the measurement error of the frequency.

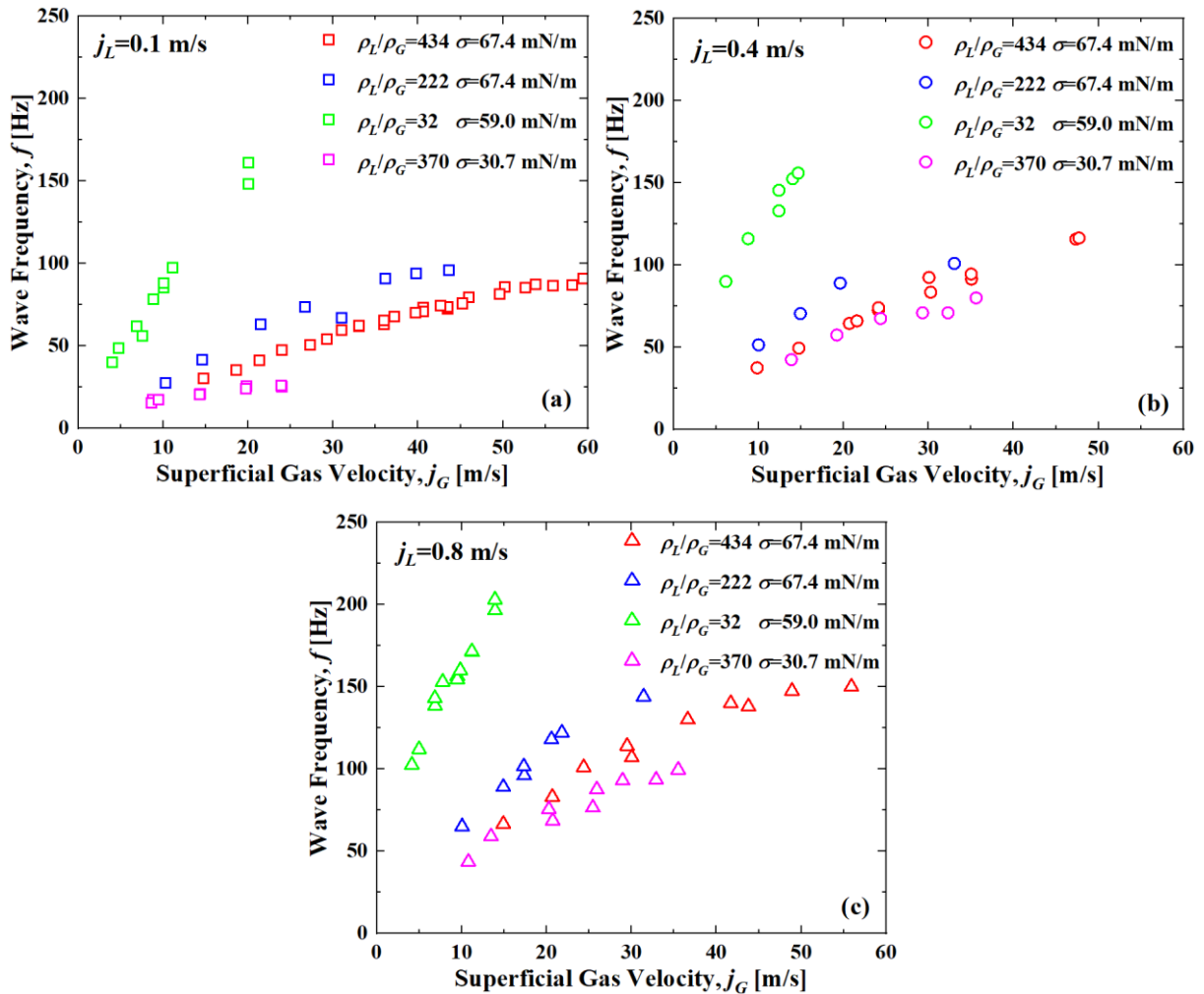


Fig. 3.16 Disturbance wave frequency at the superficial liquid velocities of (a) 0.1, (b) 0.4, and (c) 0.8 m/s.

Conventionally, the Strouhal number Sr , a dimensionless form of the disturbance wave frequency, is used to scale the wave frequency as suggested by previous research [9,35,37,44–46]. The Strouhal number of gas and liquid phases, Sr_G and Sr_L , are defined as:

$$Sr_G = \frac{fD}{j_G}, \quad (3.10)$$

$$Sr_L = \frac{fD}{j_L}. \quad (3.11)$$

Based on experimental data from various fluid systems, [47] suggests that the liquid Strouhal number can be well correlated using the Lockhart–Martinelli parameter which is defined as:

$$X = \sqrt{\frac{\rho_L j_L}{\rho_G j_G}} \quad (3.12)$$

As shown in Fig. 3.17, most data from current experiments collapse onto a single curve when the liquid Strouhal number is plotted against Lockhart–Martinelli parameter. This finding supports the proposition made by [45], which states that the frequency is directly related to the gas superficial velocity, while the effect of liquid superficial velocity is relatively negligible. Based on the current experimental data together with previous databases [35,37,48–51] as listed in Table 3.4, a new empirical correlation for wave frequency is derived as:

$$Sr_L = 0.526X^{-0.71} \quad (3.13)$$

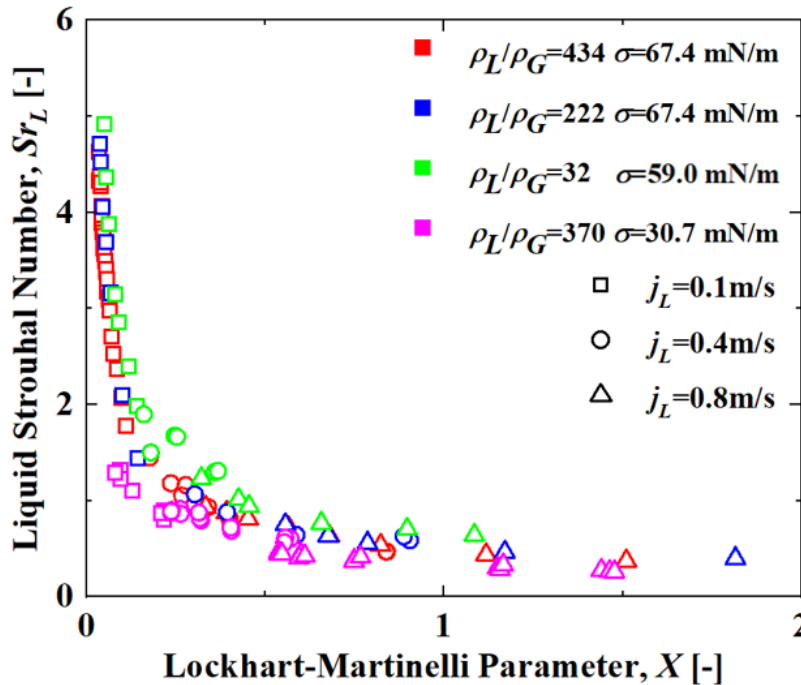


Fig. 3.17 Comparison of liquid Strouhal number with Lockhart–Martinelli parameter.

The comparison between the measured and predicted frequency by Eq. (3.13) is shown in Fig. 3.18 (a). The previous wave frequency correlations as summarized in Table 3.5 were evaluated with the current experimental data in the form of frequency as presented in Fig. 3.18 (b)–(f) [9,35,45,47,48].

It is readily apparent that models from the present work, [48], [35], and [45] have relatively satisfying performance for a wide range of flow conditions with an error of about 30%. However, as shown in Fig. 3.18, it is difficult to predict wave frequency from all the databases with only one single model. This could be attributed to the fact that frequency measurement error exists in different databases when different film thickness measuring methods (i.e., conductance probe and laser-

induced fluorescence), disturbance wave identification threshold, and disturbance wave frequency determining methods (i.e., power spectral density analysis and directly counting) are applied [36,52]. The authors attempted to develop correlations with various dimensionless numbers by multiple regression. However, the resulting correlations exhibit significant deviation in predicting wave frequency.

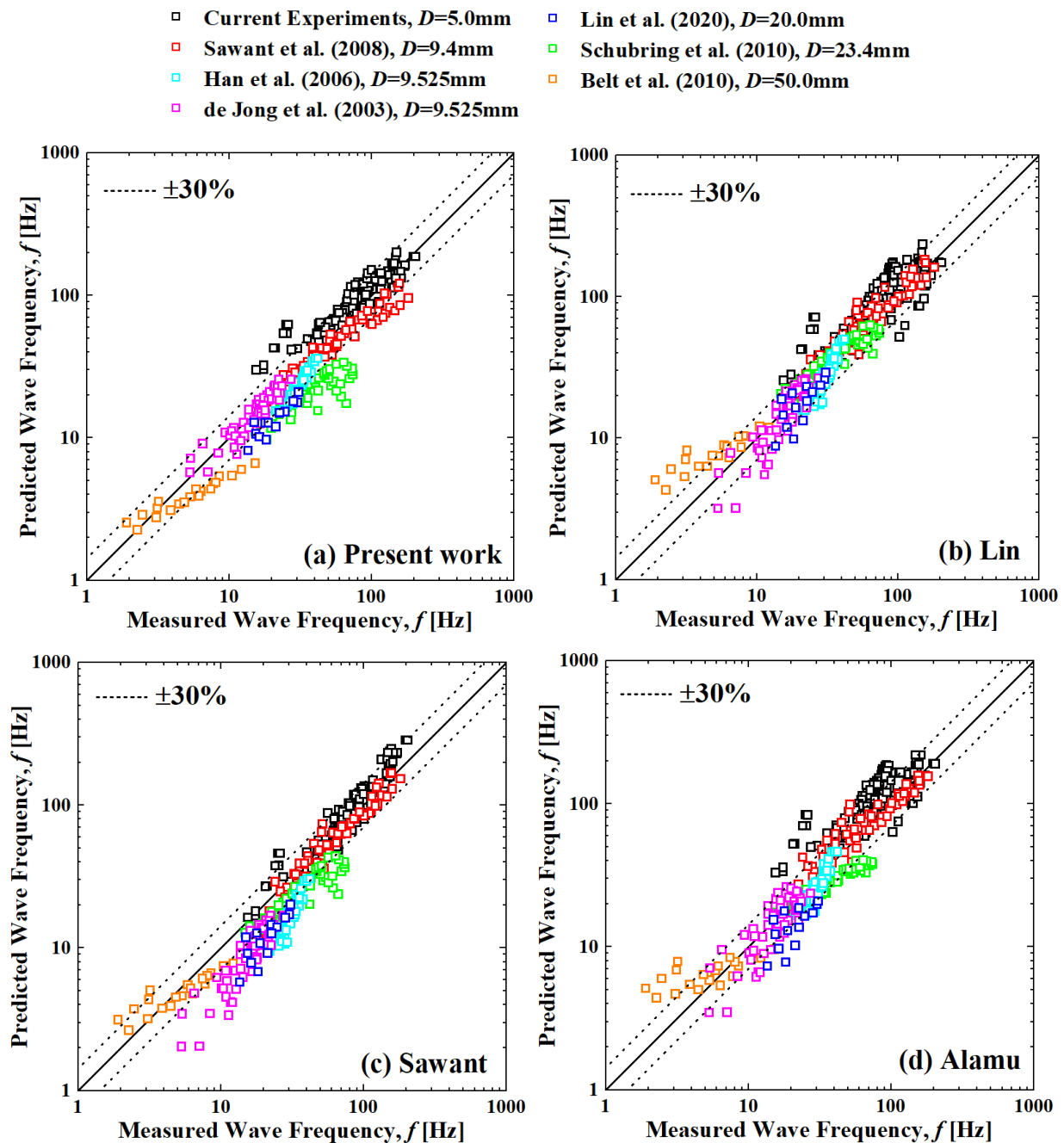


Fig. 3.18 Comparison of the measured frequency of [35], [51], [49], [48], [37], and [50] with the frequency predicted by correlations of (a) this work, (b) [48], (c) [35], (d)[45], (e) [38], and (f)[47].

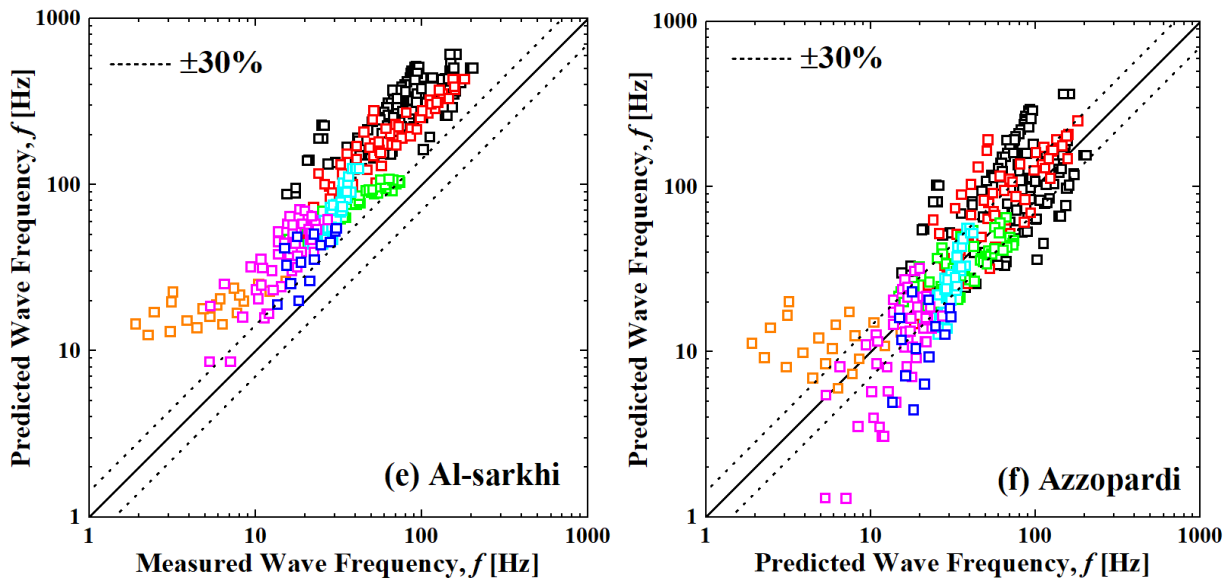


Fig. 3.18 (Continued)

Table 3.3 Summary of the experimental conditions of the databases employed.

Reference	Inner diameter (mm)	Superficial liquid velocity range (m/s)	Corresponding data range	Density ratio range	Surface tension range (N/m)
Current experiments	5.0	0.1, 0.4, and 0.8	Nitrogen–water (0.2 and 0.4 MPa), Nitrogen–95% aqueous ethanol solution (0.2 MPa), and HFC134a–water (0.7 MPa)	32–434	30.7–67.4
Belt et al. (2010)	50.0	0.01, 0.02, 0.04, and 0.08	Air–water near atmospheric pressure	819	73.3
de Jong (2003)	9.525	0.07, 0.15, and 0.31	Air–water near atmospheric pressure under normal and microgravity	832	73.0

Table 3.3 (continued)

Han (2006)	9.525	0.11, 0.13, 0.15, and 0.16	Air–water near atmospheric pressure	832	73.0
Lin (2020)	20.0	0.12, 0.22, and 0.39	Air–water near atmospheric pressure	832	73.0
Sawant et al. (2008)	9.4	0.05, 0.1, 0.15, 0.3, and 0.54	Air–water 0.12, 0.4, and 0.58 MPa	147–712	72.3
Schubring et al. (2010a)	23.4	0.04, 0.06, 0.08, 0.12, 0.15, 0.19, 0.23, 0.27, 0.35, and 0.39	Air–water near atmospheric pressure	832	73.0
Vasques et al. (2018)	11.7	0.013, 0.021, 0.029, and 0.038	Air–water near atmospheric pressure	819	73.3

Table 3.4 Previous models of wave frequency.

Reference	Correlation
Alamu and Azzopardi (2011)	$Sr_L = 0.4292X^{-0.908}$
Al-sarkhi et al. (2012)	$Sr_L = 1.1X^{-0.93}$
Azzopardi et al. (2006)	$Sr_L = 0.25X^{-1.2}$
Lin et al. (2020)	$Sr_G = 0.047Re_L^{EX0.177} \left(\frac{\rho_L}{\rho_G}\right)^{-0.37}, \text{ where } Re_L^{EX} = Re_L - Re_L^{on},$ $Re_L^{on} = \left(\frac{30}{0.347}\right)^{3/2} \left(\frac{\rho_L}{\rho_G}\right)^{3/4} \left(\frac{\mu_G}{\mu_L}\right)^{3/2}.$
Sawant et al. (2008)	$Sr_G = 0.086Re_L^{0.27} \left(\frac{\rho_L}{\rho_G}\right)^{-0.64}$

3.4 Conclusion

Upward annular flow experiments employing HFC134a and nitrogen gas as the working gas and water and 95% aqueous ethanol solution as the working liquid at the pressures of 0.2, 0.4, and 0.7 MPa were conducted. On the basis of the current experimental results, I investigated the effect of density ratio, and surface tension on wave velocity, wave pitch, wavelength, intermittency and wave frequency. Predictive models for wave velocity and frequency were developed and evaluated by using multiple previous databases. The derived correlations are compared with the correlations available in the literature. The main conclusions are as follows:

- (1) In general, the wave velocity increases with the increase of superficial liquid velocity and superficial gas velocity and decreases as the surface tension decreases. However, when both superficial liquid velocity and superficial liquid velocity are low, the effect of surface tension is not obvious in the current experiments. A wave velocity model based on the simple shear stress balance on the liquid film is developed.
- (2) The wave pitch is found to decrease with the decrease of density ratio and weakly increase with decreasing surface tension. It is also shown that a unique relationship exists between wave pitch and wave height under the same flow condition. The disturbance wave wavelength is found to decrease with the increase of the density ratio. Under a low liquid flow rate, the wavelength also decreases as the surface tension increases while the effect of surface tension is indistinctive under a high liquid flow rate. The wave intermittency increases with the increase of density ratio, albeit the effect of surface tension is not obvious in current experiments.
- (3) The wave frequency increases with the increase of superficial gas velocity and superficial liquid velocity while it also increases with the decrease of density ratio. A new correlation is developed for the prediction of disturbance wave frequency in the form of gas Strouhal number. The new correlation can predict most of the data with an error of about 25%.

References

- [1] A. Wolf, S. Jayanti, G.F. Hewitt, Flow development in vertical annular flow, *Chem. Eng. Sci.* 56 (2001) 3221–3235. [https://doi.org/10.1016/S0009-2509\(00\)00546-7](https://doi.org/10.1016/S0009-2509(00)00546-7).
- [2] R. Kumar, M. Gottmann, K.R. Sridhar, Film thickness and wave velocity measurements in a vertical duct, *J. Fluids Eng. Trans. ASME.* 124 (2002) 634–642. <https://doi.org/10.1115/1.1493808>.
- [3] H. Han, Z. Zhu, K. Gabriel, A study on the effect of gas flow rate on the wave characteristics in two-phase gas-liquid annular flow, *Nucl. Eng. Des.* 236 (2006) 2580–2588. <https://doi.org/10.1016/j.nucengdes.2006.03.015>.
- [4] P. Sawant, M. Ishii, T. Hazuku, T. Takamasa, M. Mori, Properties of disturbance waves in vertical annular two-phase flow, *Nucl. Eng. Des.* 238 (2008) 3528–3541. <https://doi.org/10.1016/j.nucengdes.2008.06.013>.
- [5] C. Berna, A. Escrivá, J.L. Muñoz-Cobo, L.E. Herranz, Review of droplet entrainment in annular flow: Interfacial waves and onset of entrainment, *Prog. Nucl. Energy.* 74 (2014) 14–43. <https://doi.org/10.1016/j.pnucene.2014.01.018>.
- [6] M. Ishii, M.A. Grolmes, Inception criteria for droplet entrainment in two-phase concurrent film flow, *AIChE J.* 21 (1975) 308–318. <https://doi.org/10.1002/aic.690210212>.
- [7] P. Ju, Y. Liu, X. Yang, M. Ishii, Wave characteristics of vertical upward adiabatic annular flow in pipes, *Int. J. Heat Mass Transf.* 145 (2019) 1–10. <https://doi.org/10.1016/j.ijheatmasstransfer.2019.118701>.
- [8] Barry Azzopardi, Disturbance wave frequencies, velocities and spacing in vertical annular two-phase flow, *Nucl. Eng. Des.* 92 (1986) 121–133.
- [9] A. Al-Sarkhi, C. Sarica, K. Magrini, Inclination effects on wave characteristics in annular gas-liquid flows, *AIChE J.* 58 (2012) 1018–1029. <https://doi.org/10.1002/aic.12653>.
- [10] A. Dasgupta, D.K. Chandraker, S. Kshirasagar, B.R. Reddy, R. Rajalakshmi, A.K. Nayak, S.P. Walker, P.K. Vijayan, G.F. Hewitt, Experimental investigation on dominant waves in upward air-water two-phase flow in churn and annular regime, *Exp. Therm. Fluid Sci.* 81 (2017) 147–163. <https://doi.org/10.1016/j.expthermflusci.2016.10.012>.
- [11] K. SEKOGUCHI, T. UENO, O. TANAKA, An investigation of the flow characteristics in the disturbance wave region of annular flow (2nd report, On correlation of principal flow parameters), *Trans. Jpn. Soc. Mech. Eng. Ser. B.* 51 (1985) 1798–1806. <https://doi.org/10.1299/kikaib.51.1798>.
- [12] G. Wang, Z. Dang, M. Ishii, Wave structure and velocity in vertical upward annular two-phase flow, *Exp. Therm. Fluid Sci.* 120 (2021). <https://doi.org/10.1016/j.expthermflusci.2020.110205>.

- [13] L.M. Pan, H. He, P. Ju, T. Hibiki, M. Ishii, The influences of gas-liquid interfacial properties on interfacial shear stress for vertical annular flow, *Int. J. Heat Mass Transf.* 89 (2015) 1172–1183. <https://doi.org/10.1016/j.ijheatmasstransfer.2015.06.022>.
- [14] D. Schubring, T.A. Shedd, A model for pressure loss, film thickness, and entrained fraction for gas-liquid annular flow, *Int. J. Heat Fluid Flow.* 32 (2011) 730–739. <https://doi.org/10.1016/j.ijheatfluidflow.2011.02.010>.
- [15] D. Schubring, T.A. Shedd, E.T. Hurlburt, Studying disturbance waves in vertical annular flow with high-speed video, *Int. J. Multiph. Flow.* 36 (2010) 385–396. <https://doi.org/10.1016/j.ijmultiphaseflow.2010.01.003>.
- [16] S. V. Alekseenko, A. V. Cherdantsev, O.M. Heinz, S.M. Kharlamov, D.M. Markovich, Analysis of spatial and temporal evolution of disturbance waves and ripples in annular gas-liquid flow, *Int. J. Multiph. Flow.* 67 (2014) 122–134. <https://doi.org/10.1016/j.ijmultiphaseflow.2014.07.009>.
- [17] J. Vasques, A. Cherdantsev, M. Cherdantsev, S. Isaenkov, D. Hann, Comparison of disturbance wave parameters with flow orientation in vertical annular gas-liquid flows in a small pipe, *Exp. Therm. Fluid Sci.* 97 (2018) 484–501. <https://doi.org/10.1016/j.expthermflusci.2018.03.020>.
- [18] I. Kataoka, M. Ishii, Mechanism and correlation of droplet entrainment and deposition in annular two-phase flow., (1982).
- [19] N.B. Vargaftik, Handbook of physical properties of liquids and gases-pure substances and mixtures, (1975).
- [20] G.F. Hewitt, D.N. Roberts, Studies of two-phase flow patterns by simultaneous x-ray and flash photography, *Aere-M* 2159. (1969) 28.
- [21] K. Mishima, M. Ishii, Flow regime transition criteria for upward two-phase flow in vertical tubes, *Int. J. Heat Mass Transf.* 27 (1984) 723–737. [https://doi.org/10.1016/0017-9310\(84\)90142-X](https://doi.org/10.1016/0017-9310(84)90142-X).
- [22] A.H. Govan, G.F. Hewitt, D.G. Owen, G. Burnett, Wall shear stress measurements in vertical air-water annular two-phase flow, *Int. J. Multiph. Flow.* 15 (1989) 307–325. [https://doi.org/10.1016/0301-9322\(89\)90003-7](https://doi.org/10.1016/0301-9322(89)90003-7).
- [23] T. Okawa, T. Kitahara, K. Yoshida, T. Matsumoto, I. Kataoka, New entrainment rate correlation in annular two-phase flow applicable to wide range of flow condition, *Int. J. Heat Mass Transf.* 45 (2001) 87–98. [https://doi.org/10.1016/S0017-9310\(01\)00111-9](https://doi.org/10.1016/S0017-9310(01)00111-9).
- [24] A. Wolf, S. Jayanti, G.F. Hewitt, Flow development in vertical annular flow, *Chem. Eng. Sci.* 56 (2001) 3221–3235. [https://doi.org/10.1016/S0009-2509\(00\)00546-7](https://doi.org/10.1016/S0009-2509(00)00546-7).
- [25] P. Ju, Y. Liu, X. Yang, M. Ishii, Wave characteristics of vertical upward adiabatic annular flow

- in pipes, *Int. J. Heat Mass Transf.* 145 (2019) 1–10. <https://doi.org/10.1016/j.ijheatmasstransfer.2019.118701>.
- [26] G.H. Anderson, B.G. Mantzouranis, Two-phase (gas-liquid) flow phenomena-I Pressure drop and hold-up for two-phase flow in vertical tubes, *Chem. Eng. Sci.* 12 (1960) 109–126. [https://doi.org/10.1016/0009-2509\(60\)87004-2](https://doi.org/10.1016/0009-2509(60)87004-2).
- [27] E.M. Aydin, H.J. Leutheusser, Plane-Couette flow between smooth and rough walls, *Exp. Fluids.* 11 (1991) 302–312. <https://doi.org/10.1007/BF00194862>.
- [28] C. Wang, N. Zhao, Y. Feng, H. Sun, L. Fang, Interfacial wave velocity of vertical gas-liquid annular flow at different system pressures, *Exp. Therm. Fluid Sci.* 92 (2018) 20–32. <https://doi.org/10.1016/j.expthermflusci.2017.09.007>.
- [29] R. Kumar, M. Gottmann, K.R. Sridhar, Film thickness and wave velocity measurements in a vertical duct, *J. Fluids Eng. Trans. ASME.* 124 (2002) 634–642. <https://doi.org/10.1115/1.1493808>.
- [30] G.B. Wallis, One-dimensional two-phase flow, Courier Dover Publications, 1969.
- [31] R.J. Belt, J.M.C. Van't Westende, L.M. Portela, Prediction of the interfacial shear-stress in vertical annular flow, *Int. J. Multiph. Flow.* 35 (2009) 689–697. <https://doi.org/10.1016/j.ijmultiphaseflow.2008.12.003>.
- [32] P. Ju, Y. Liu, C.S. Brooks, M. Ishii, Prediction of interfacial shear stress of vertical upward adiabatic annular flow in pipes, *Int. J. Heat Mass Transf.* 133 (2019) 500–509. <https://doi.org/10.1016/j.ijheatmasstransfer.2018.12.057>.
- [33] H. Zhang, S. Mori, T. Hisano, H. Yoshida, Effect of gas density and surface tension on liquid film thickness in vertical upward disturbance wave flow, *Int. J. Multiph. Flow.* 159 (2023) 104342. <https://doi.org/10.1016/j.ijmultiphaseflow.2022.104342>.
- [34] D. Schubring, T.A. Shedd, E.T. Hurlburt, Planar laser-induced fluorescence (PLIF) measurements of liquid film thickness in annular flow. Part II: Analysis and comparison to models, *Int. J. Multiph. Flow.* 36 (2010) 825–835. <https://doi.org/10.1016/j.ijmultiphaseflow.2010.02.002>.
- [35] P. Sawant, M. Ishii, T. Hazuku, T. Takamasa, M. Mori, Properties of disturbance waves in vertical annular two-phase flow, *Nucl. Eng. Des.* 238 (2008) 3528–3541. <https://doi.org/10.1016/j.nucengdes.2008.06.013>.
- [36] J. Vasques, A. Cherdantsev, M. Cherdantsev, S. Isaenkov, D. Hann, Comparison of disturbance wave parameters with flow orientation in vertical annular gas-liquid flows in a small pipe, *Exp. Therm. Fluid Sci.* 97 (2018) 484–501. <https://doi.org/10.1016/j.expthermflusci.2018.03.020>.
- [37] D. Schubring, T.A. Shedd, E.T. Hurlburt, Studying disturbance waves in vertical annular flow with high-speed video, *Int. J. Multiph. Flow.* 36 (2010) 385–396.

<https://doi.org/10.1016/j.ijmultiphaseflow.2010.01.003>.

- [38] A. Al-Sarkhi, C. Sarica, K. Magrini, Inclination effects on wave characteristics in annular gas-liquid flows, *AIChE J.* 58 (2012) 1018–1029. <https://doi.org/10.1002/aic.12653>.
- [39] C. Berna, A. Escrivá, J.L. Muñoz-Cobo, L.E. Herranz, Review of droplet entrainment in annular flow: Interfacial waves and onset of entrainment, *Prog. Nucl. Energy.* 74 (2014) 14–43. <https://doi.org/10.1016/j.pnucene.2014.01.018>.
- [40] P. Sawant, M. Ishii, T. Hazuku, T. Takamasa, M. Mori, Properties of disturbance waves in vertical annular two-phase flow, *Nucl. Eng. Des.* 238 (2008) 3528–3541. <https://doi.org/10.1016/j.nucengdes.2008.06.013>.
- [41] D. Schubring, T.A.A. Shedd, E.T.T. Hurlburt, A.C. Ashwood, T.A.A. Shedd, E.T.T. Hurlburt, A.C. Ashwood, T.A.A. Shedd, E.T.T. Hurlburt, Planar laser-induced fluorescence (PLIF) measurements of liquid film thickness in annular flow. Part II: Analysis and comparison to models, *Int. J. Multiph. Flow.* 36 (2010) 825–835. <https://doi.org/10.1016/j.ijmultiphaseflow.2010.02.002>.
- [42] G.F. Hewitt, B. Nicholls, FILM THICKNESS MEASUREMENT IN ANNULAR TWO-PHASE FLOW USING A FLUORESCENCE SPECTROMETER TECHNIQUE. PART II. STUDIES OF THE SHAPE OF DISTURBANCE WAVES., United Kingdom, 1969.
- [43] J. Wurtz, An experimental and theoretical investigation of annular steam-water flow in tubes and annuli at 30 to 90bar, *Riso Rep.* (1978) 141.
- [44] B.J. Azzopardi, Drops in annular two-phase flow, *Int. J. Multiph. Flow.* 23 (1997) 1–53. [https://doi.org/10.1016/S0301-9322\(97\)90087-2](https://doi.org/10.1016/S0301-9322(97)90087-2).
- [45] M.B. Alamu, B.J. Azzopardi, Wave and drop periodicity in transient annular flow, *Nucl. Eng. Des.* 241 (2011) 5079–5092. <https://doi.org/10.1016/j.nucengdes.2011.08.015>.
- [46] A. Dasgupta, D.K. Chandraker, S. Kshirasagar, B.R. Reddy, R. Rajalakshmi, A.K. Nayak, S.P. Walker, P.K. Vijayan, G.F. Hewitt, Experimental investigation on dominant waves in upward air-water two-phase flow in churn and annular regime, *Exp. Therm. Fluid Sci.* 81 (2017) 147–163. <https://doi.org/10.1016/j.expthermflusci.2016.10.012>.
- [47] B.J. Azzopardi, *Gas-liquid flows*, Begell house New York, 2006.
- [48] R. Lin, K. Wang, L. Liu, Y. Zhang, S. Dong, Application of the image analysis on the investigation of disturbance waves in vertical upward annular two-phase flow, *Exp. Therm. Fluid Sci.* 114 (2020). <https://doi.org/10.1016/j.expthermflusci.2020.110062>.
- [49] P. de Jong, K.S. Gabriel, A preliminary study of two-phase annular flow at microgravity: Experimental data of film thickness, *Int. J. Multiph. Flow.* 29 (2003) 1203–1220. [https://doi.org/10.1016/S0301-9322\(03\)00085-5](https://doi.org/10.1016/S0301-9322(03)00085-5).

- [50] R.J. Belt, J.M.C. Van't Westende, H.M. Prasser, L.M. Portela, Time and spatially resolved measurements of interfacial waves in vertical annular flow, *Int. J. Multiph. Flow.* 36 (2010) 570–587. <https://doi.org/10.1016/j.ijmultiphaseflow.2010.03.004>.
- [51] H. Han, Z. Zhu, K. Gabriel, A study on the effect of gas flow rate on the wave characteristics in two-phase gas-liquid annular flow, *Nucl. Eng. Des.* 236 (2006) 2580–2588. <https://doi.org/10.1016/j.nucengdes.2006.03.015>.
- [52] G. Wang, Z. Dang, M. Ishii, Wave structure and velocity in vertical upward annular two-phase flow, *Exp. Therm. Fluid Sci.* 120 (2021). <https://doi.org/10.1016/j.expthermflusci.2020.110205>.

CHAPTER 4

Effect of density ratio and surface tension on interfacial shear stress and pressure drop

The interfacial shear stress and pressure drop of upward vertical Nitrogen-Water, HFC134a-Water, and Nitrogen-95% Ethanol annular flows are comprehensively investigated with considering the effect of liquid-gas density ratio and surface tension. A direct link between disturbance wave height and the equivalent sand-grain roughness is found through the analogy to the famous Moody chart for single-phase turbulent flow. A predictive model of interfacial friction factor is developed based on this finding. To predict the pressure drop of annular flow, another model is proposed which shows good predictive performance for annular flow with various working fluids including steam-water annular flow under 7MPa.

4.1 Introduction

Annular flow is a two-phase flow regime that is encountered in many industries, such as nuclear reactors and refrigeration systems. It consists of a continuously flowing gas core, liquid film attaching to the tube wall, and intermittent disturbance waves at the gas-liquid interface. In many industrial applications especially energy facilities, it is critical to provide accurate prediction of pressure drop of two-phase flow system for increasing energy conversion efficiency. Meanwhile, accompanied by the wavy structure of the gas-liquid interface, the gas at the core flows upward with a larger frictional pressure drop than it in a smooth wall tube as a single-phase flow due to the higher interfacial shear stress, τ_i , induced by the roughened interface. Considering that interfacial shear stress can make a critical contribution to the pressure drop of two-phase annular flow, interfere with force balances of both gas core and liquid film, and be coupled with liquid film characteristics, accurate prediction of interfacial shear stress has received huge attention and attracted numerous researchers.

Conventionally, the interfacial shear stress is expressed by the equation involving gas density, gas velocity, and interfacial friction factor which is denoted by C_{fi} . Wallis [1] derived the correlations for the interfacial friction factor considering the liquid film as a type of wall roughness of single phase flow. Since then, a large amount of correlations of interfacial friction factor were proposed. To the author's best knowledge, these correlations can be roughly divided into 4 types based on the derivation method. The first type of C_{fi} correlations are the Wallis-type correlations which are mostly arithmetic modifications of Wallis correlation. For example, Moeck raised the exponent of the dimensionless average film thickness and altered other coefficients [2]. Fukano and Furukawa

introduced the liquid kinetic viscosity to account for the effect of the change in the working fluids viscosity [3]. Fore et al. added gas Reynolds number to Wallis correlation to better predict C_{fi} over a wide range of gas Reynolds numbers and liquid film thicknesses [4]. Ju et al. derived C_{fi} correlation by introducing Weber numbers and viscosity number which are related to the dimensionless average film thickness into Wallis correlation [5]. The second type of C_{fi} correlations relate the interfacial friction factor to the sand-grain roughness of turbulent single-phase flow in rough pipes. Oliemans et al. [6] obtained the correlation for interface roughness employing gas Weber number and combined it with the phenomenological Colebrook equation [7], which expresses the Darcy friction factor as a function of Reynolds number and wall roughness, to predict C_{fi} . Belt et al. found the relationship between the average film thickness and equivalent sand-grain roughness, which is obtained from the Churchill equation, which is a famous approximation of Colebrook equation, and derived the empirical correlation for C_{fi} [8]. The third type of C_{fi} correlations can be treated as the modification of Wallis equation by using a computed single-phase gas friction factor for a smooth walled tube, C_{fs} , in replace of the constant 0.005 in Wallis equation, represented by Henstock [9], Asali [10], Hajiloo [11], and Aliyu [12,13]. Last but not least, the fourth type of C_{fi} correlations is based on the dimensional analysis on the experimental data as derived by Cioncolini et al. [14].

Although interfacial shear stress of annular flow has been investigated extensively [14–17], most experimental investigations available in the literature were conducted by using air and water under nearly atmospheric pressure, whereas the variety of fluid properties was limited. The present authors have already reported on the effect of density ratio and surface tension on the liquid film thickness and disturbance wave height [18], and velocity, pitch, and frequency of disturbance waves [19]. In this work, the effect of density ratio and surface tension on interfacial shear stress will be experimentally studied by using nitrogen gas, HFC134a gas, water, and 95% (v/v) aqueous ethanol solution as working fluids under the pressure from 0.2 MPa to 0.7 MPa in a 5.0 mm inner diameter tube. New models will be proposed for predicting interfacial shear stress and pressure drop for vertical upward annular flow.

4.2 Experimental apparatus and procedures

In this chapter, same experimental facility as described in Chapter 2 is employed. However, to measure the pressure drop, a Kyowa PD-A differential pressure transducer was installed to measure the differential pressure over 0.5 m from 0.105 m downstream the inlet of the test section as shown

in Fig 4.1. The uncertainty of the differential pressure measurement was estimated at 10%. As summarized in Table 1.2, the experimental conditions in this study were the same as those in Chapter 2 & 3. The properties of the working liquid and gas are listed in Table 1.2. Gas density, liquid density, surface tension, gas viscosity, and liquid viscosity are denoted as ρ_G , ρ_L , σ , μ_G , and μ_L , respectively and obtained in the same way as previous chapters.

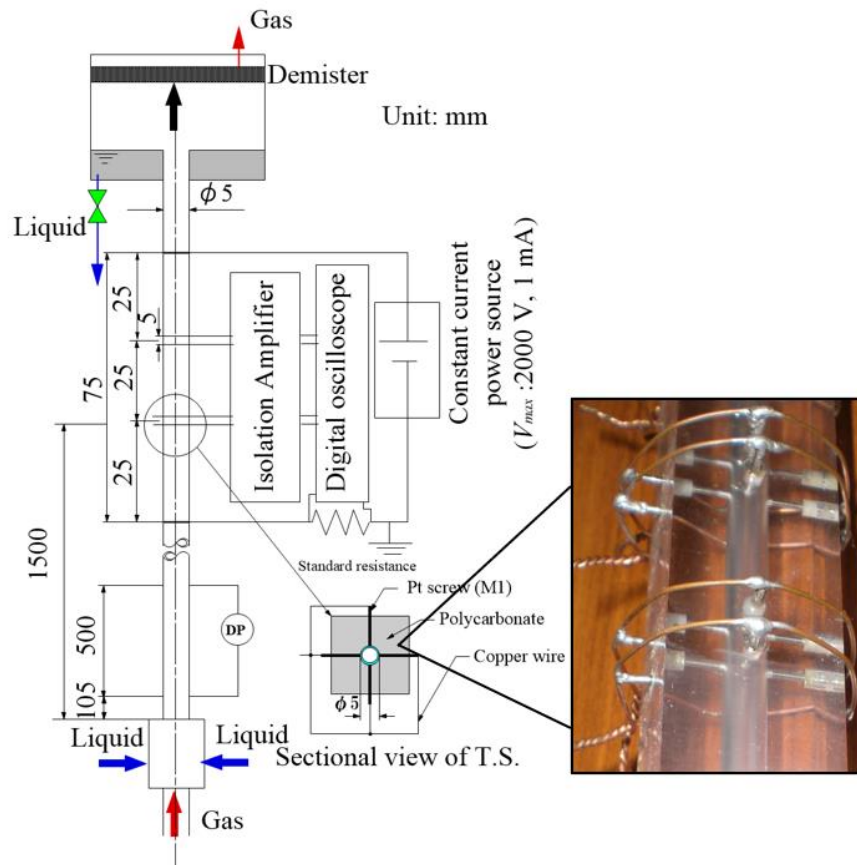


Fig. 4.1 Schematic of the test section.

4.3 Results and discussion

4.3.1 Pressure gradient and interfacial shear stress

The measured average pressure gradient, dP/dz , over 0.5 m is presented in Fig. 4.2. It is shown that the pressure gradient increases with the increase of superficial gas velocity, j_G , and the decrease in density ratio. Moreover, the pressure gradient tends to decrease as the surface tension decreases when j_L is 0.4 m/s and 0.8 m/s.

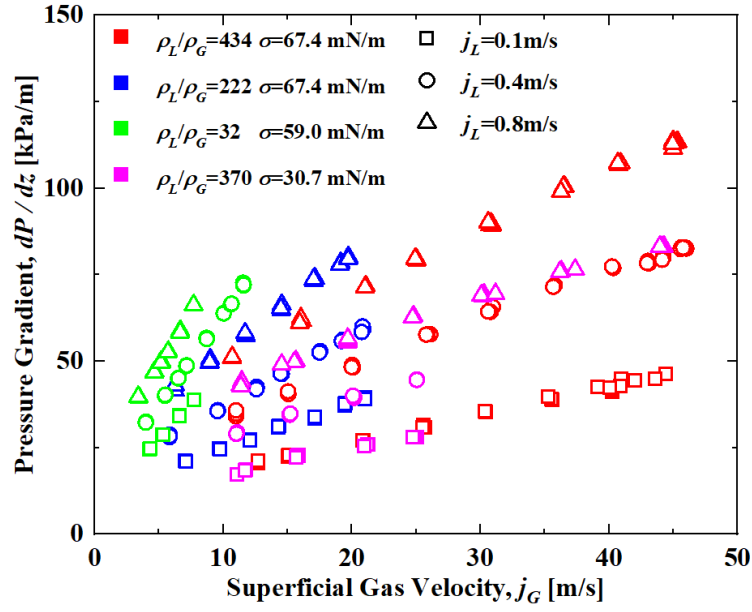


Fig. 4.2. Measured pressure gradient over 0.5 m.

Conventionally, for the equilibrium annular flow, the interfacial shear stress can be expressed as [4,5,8,20,21]

$$\tau_i = -\frac{D-2t_{Fave}}{4} \left[\frac{dP}{dz} \left(1 - \frac{\rho_c j_G^2}{P} \right) + \rho_c g \right] - R_D (u_D - u_E). \quad (4.1)$$

where $\frac{dP}{dz}$ is the pressure gradient, t_{Fave} the average film thickness, ρ_c the core mixture density, P the system pressure, R_D the deposition rate, u_D the mean axial velocity of depositing drops and u_E the mean axial velocity of entraining drops. Here, ρ_c can be expressed by using droplet volume fraction inside gas core, α_d , and entrainment rate (E) from the model of Sawant [22]:

$$\rho_c = (1 - \alpha_d)\rho_G + \alpha_d\rho_L, \quad (4.2)$$

$$\alpha_d = \frac{Ej_L}{Ej_L + j_G}. \quad (4.3)$$

However, considering the maximum entrainment rate in current experiments is less than 0.05 as calculated by Eq. (2.14) and the difference between ρ_c and ρ_G is less than 10%, $\rho_c \approx \rho_G$ is adopted in this study. This assumption has also been adopted by Ju et al. [5] since it can avoid bringing extra errors. R_D is estimated using the correlation from Ishii and Mishima [23] as suggested by Schubring et al [20]. u_E and u_D are roughly estimated by the disturbance wave velocity and actual gas velocity for simplicity, which is consistent with previous studies [8,20]. Considering gas flow rate in current experiments is relatively low and the entrainment and deposition rates are small, the contribution of the frictional pressure drop into the total pressure drop is expected to be the most significant over the

gravity force, axial momentum change, and momentum change due to droplet deposition and entrainment. Therefore, as suggested by previous studies [3,21], the interfacial shear can be roughly expressed as:

$$\tau_i = -\frac{D-2t_{Fave}}{4} \frac{dP}{dz}. \quad (4.4)$$

The interfacial shear calculated using Eqs. (4.1) and (4.4) are compared in Fig. 4.2 and the maximum deviation between them is 5.7%. For the simplicity, the τ_i in this study will be obtained by Eq. (4.4) in this work.

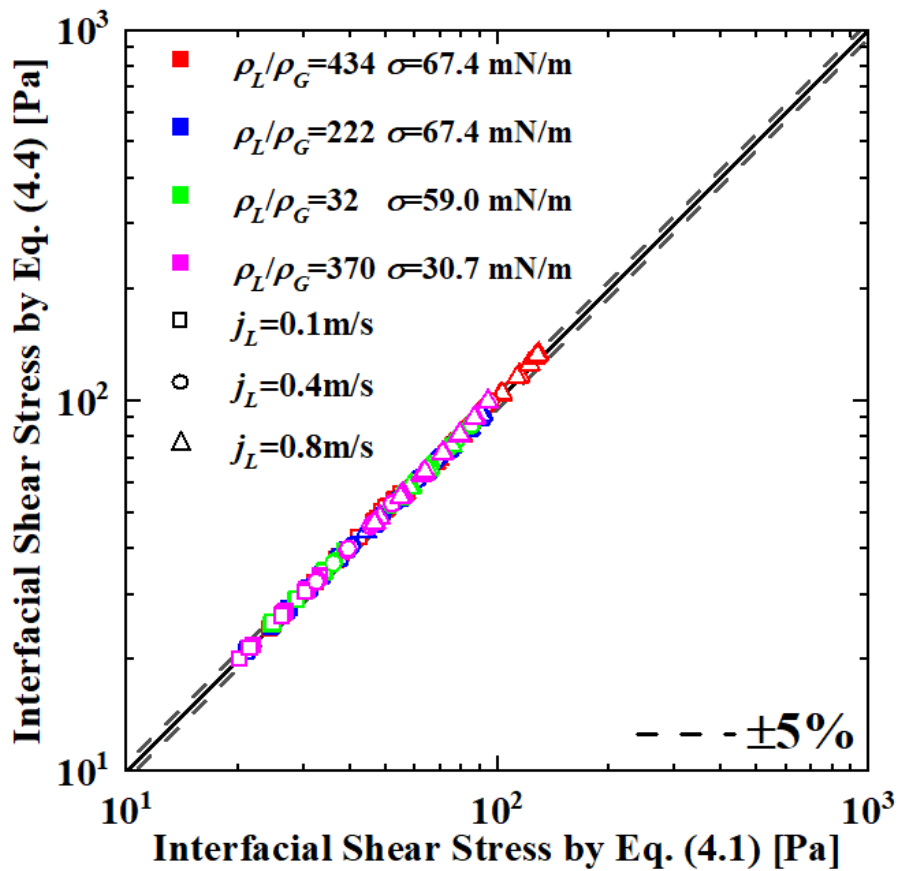


Fig. 4.3. Comparison of the interfacial shear stress calculated by Eqs. (4.1) and (4.4).

The τ_i calculated from Eq. (4.4) is plotted against j_G as shown in the Fig. 4.5. It is shown that the tendency is quite similar with it for the $\frac{dP}{dz}$. τ_i increases with the increase of j_G and the decrease in density ratio. When j_L is 0.4 m/s and 0.8 m/s, τ_i also decreases as the surface tension decreases.

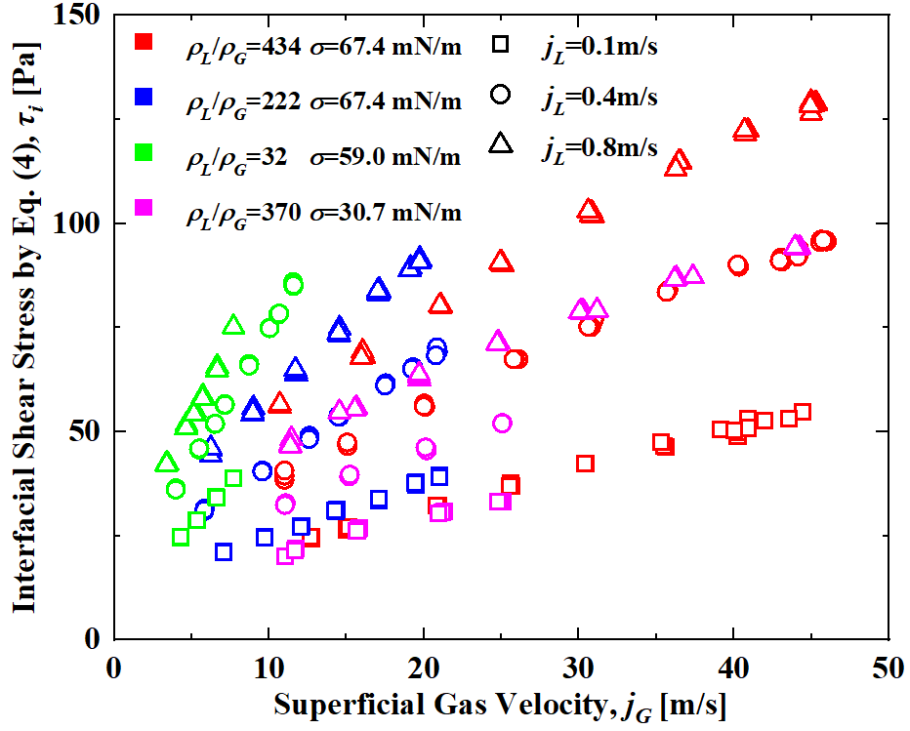


Fig. 4.4. Interfacial shear stress calculated by Eq. (4.4).

4.3.2 Interfacial friction factor

Considering t_{Fave} is negligible compared to the tube diameter and the difference between the gas core and the liquid film is usually small, the following relationship is chosen to calculate the interfacial friction factor in this study for the simplicity and avoiding introducing errors from the measurement:

$$\tau_i = \frac{C_{fi}\rho_G j_G^2}{2}. \quad (4.5)$$

Since this typical form of C_{fi} is simple to calculate the interfacial shear stress, it has been widely adopted by previous studies [4,5,8,12,21]. Physically, the interfacial shear stress is described using the relative velocity between two phases, $j_G - u_L$. However, the uncertainty of t_{Fave} can introduce large error in the u_L that is expressed as $u_L = \frac{Dj_L}{4t_{Fave}}$. Besides, u_L is about 16% the j_G on average except experiments of HFC134a-water annular flow under high liquid flow rate and the potential error could be accounted for by the empirical coefficients in the C_{fi} correlation. Therefore, to simplify the computation of interfacial shear stress and proposing an easy-to-use correlation of C_{fi} for predicting interfacial shear stress, j_G is used. Meanwhile, it is shown in a later discussion that, when the relationship between C_{fi} and τ_i is given by Eq. (4.5), it is available to predict C_{fi} with good

predictive performance.

From Wang et al. [24] and Wang et al. [25], the interfacial friction factor in annular flow is closely related to the interfacial roughness, which is similar to the case in single-phase flow and the interfacial roughness is dependence on the disturbance wave height, H . Since interfacial friction factor is usually related to the Reynolds number, the normalized wave height and interfacial friction factor are plotted against gas Reynolds number for comparison in Fig. 4.6. The gas Reynolds number is expressed as:

$$Re_G = \frac{\rho_G j_G D}{\mu_G}. \quad (4.6)$$

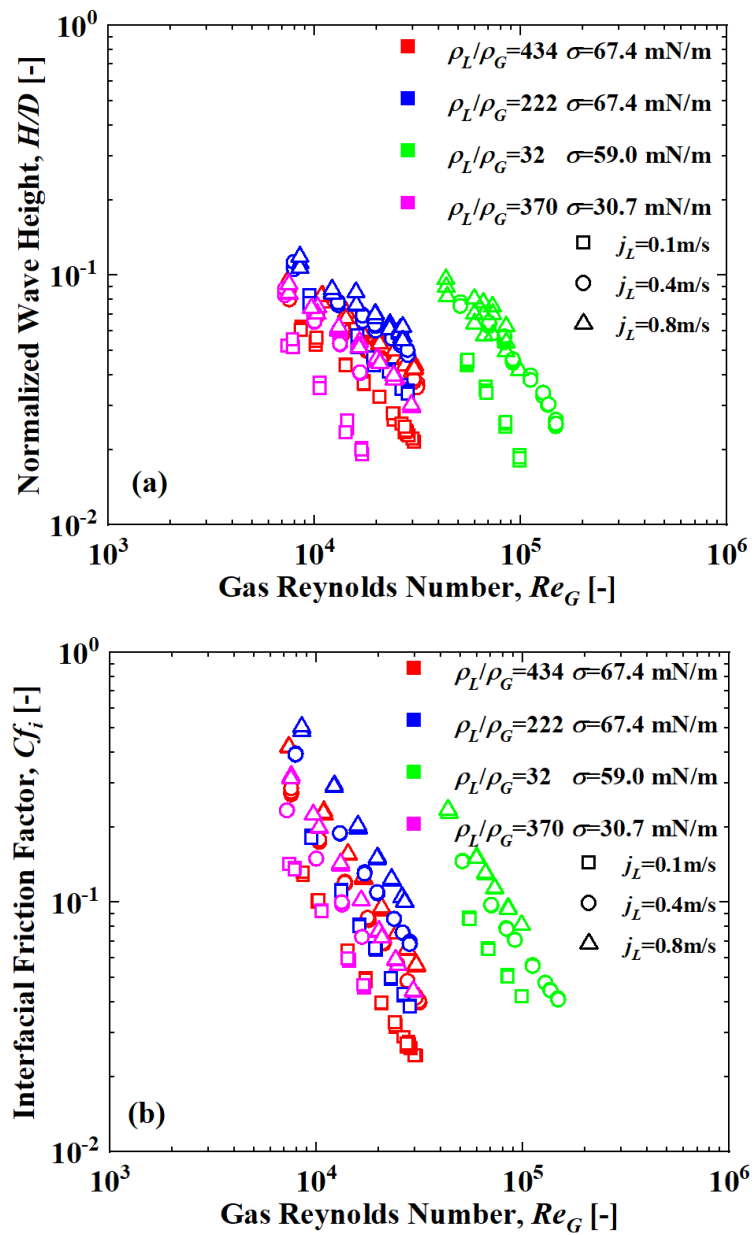


Fig. 4.5. Comparison between Re_G and (a) H/D , and (b) C_{fi} .

Similar with the findings by Wang et al. [24], both interfacial friction factor and disturbance wave height decrease with the increase of Re_G under the same liquid flow rate, density ratio, and surface tension. It is also shown that the decrease in the interfacial friction factor is usually accompanied by the decrease in the normalized wave height under the same condition, indicating that the interfacial friction factor is closely related to the disturbance wave height. However, the physical explanation for this is still missing.

From Belt et al. [8], a physical approach is proposed to predict the interfacial shear stress based on the theory of equivalent sand-grain roughness for single-phase turbulent flow. It is found that the equivalent sand-grain roughness of annular flow is proportional to the wave height, instead of four times the mean film thickness as assumed by Wallis et al. [1]. However, the authors did not show the relationship between the sand-grain roughness and the wave height. Instead, a C_{fi} correlation is proposed based on the linear dependency between the interfacial friction factor and average film thickness rather than wave height. As described in [8,16], the normalized equivalent sand-grain roughness, k_S/D , can be obtained from the Churchill equation expressed as [26]:

$$\frac{1}{\sqrt{C_{fi}}} = 8.1 \ln \left[\frac{1}{\left(\frac{7}{Re_G}\right)^{0.9} + 0.27 \frac{k_S}{D}} \right]. \quad (4.7)$$

The comparison between k_S/D and H/D and t_{Fave}/D is presented in Fig. 4.6. It is readily apparent that, for most of the data, the single unifying relationship between k_S/D and H/D exists even the experimental condition and flow rate is different. However, when plotted against the t_{Fave}/D , the deviation becomes larger. This indicates that the interface roughness tends to be related to the H/D and its estimation by using t_{Fave}/D could lead to larger error. Based on current experimental data, this relationship between k_S/D and H/D is concluded as the Eq. (4.8) and is indicated by the solid line with the error range of 25% as shown in Fig. 4.6.

$$\frac{k_S}{D} = 20 \left(\frac{H}{D}\right)^{1.05}. \quad (4.8)$$

As shown in Fig. 4.7, the single unifying relationship also exists between the C_{fi} and H/D rather than t_{Fave}/D . This indicates that, even for the annular flow, the equivalent sand-grain roughness which is characterized by the disturbance wave height, is still the key factor for the interfacial friction factor as it in the single-phase turbulent flow, which is described by the famous Moody chart [27]. This could also be extended to explain that the pressure drop and interfacial stress become relatively small when surface tension is reduced. When under the same flow rate and density ratio, smaller surface tension will result in the wave crest to be easier for shearing by the gas core. Then, the interface roughness, characterized by the wave height will be reduced causing the decrease in the

interfacial friction factor. Considering the wave height is a function of liquid and gas Weber number in Eq. (2.27) [18], the $\frac{1}{\sqrt{C_{fi}}}$ in the Eq. (4.6) should also be a function of gas Reynolds number together with liquid and gas Weber number. Thus, the term $\frac{1}{(\frac{7}{Re_G})^{0.9} + 0.27 \frac{k_S}{D}}$ in Eq. (4.7) is reduced to a function of a dimensionless number group consisting of the gas Reynolds number, liquid Weber number, and gas Weber number, considering that k_S/D is related to H/D . Here, the liquid and gas Weber number are expressed by:

$$We_L = \frac{\rho_L j_L^2 D}{\sigma}, \quad (4.9)$$

$$We_G = \frac{\rho_G j_G^2 D}{\sigma}. \quad (4.10)$$

Eq. (4.7) can then be simplified as the following form coefficients $A-F$:

$$\frac{1}{\sqrt{C_{fi}}} = A \ln[B + C Re_G^D We_L^E We_G^F]. \quad (4.11)$$

After employing current experimental data and previous databases by Fukano and Furukawa [3], Sawant et al. [28] and Wang et al. [21] (summarized in Table 4.2) for including the effect of tube diameter, a new model is derived based on the Eq. (4.11) as:

$$\frac{1}{\sqrt{C_{fi}}} = 8.1 \ln[1.1 + 0.08 Re_G^{0.11} We_L^{-0.24} We_G^{0.52}]. \quad (4.12)$$

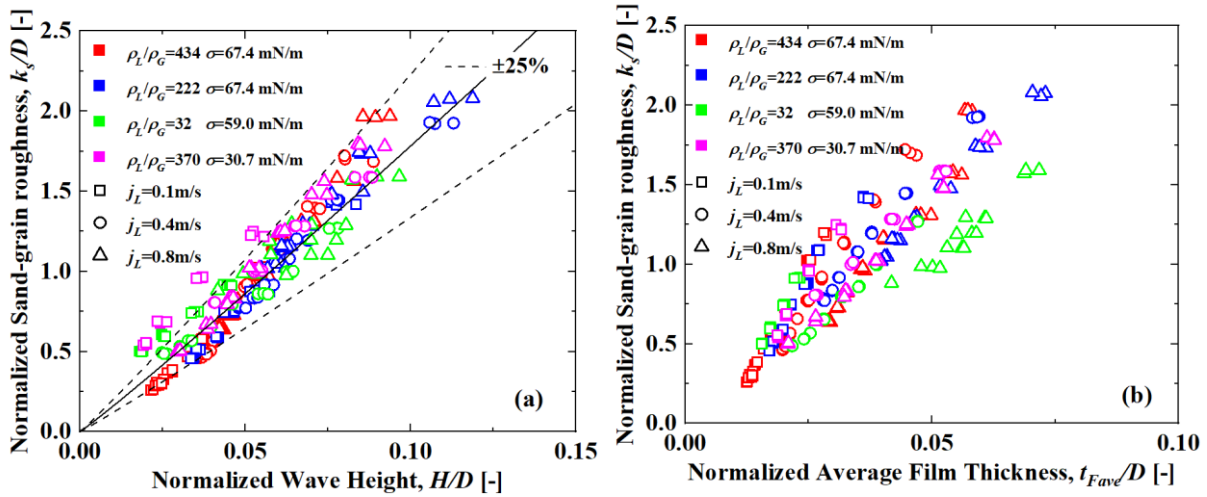


Fig. 4.6. Comparison between k_s/D and (a) H/D ; (b) t_{Fave}/D

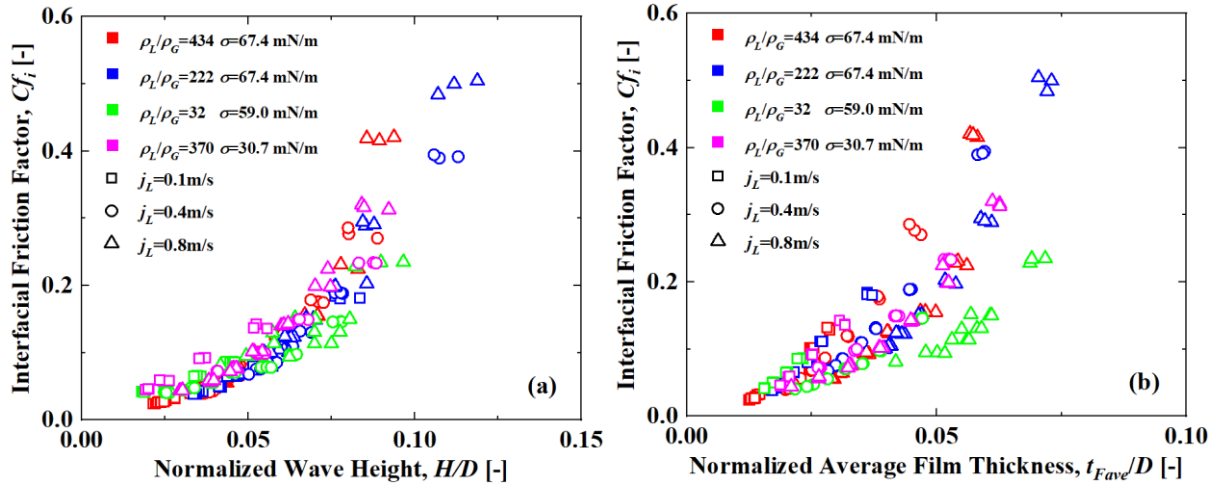


Fig. 4.7. Comparison between C_{fi} and (a) H/D ; (b) t_{Fave}/D .

The newly proposed model in this work, which is expressed by Eq. (4.12), is evaluated by using the current and previous databases together with several existing correlations on C_{fi} as summarized in Table 4.3. The comparison between the measured and predicted C_{fi} is presented in Fig. 4.9. It is shown that the correlation from present work and Ju et al. [5] can provide the best prediction performance with an error of ca. 25%. However, some data under low liquid flow rate from present work are underestimated by the correlation of Ju et al.

Table 4.1 Summary of the experimental conditions of the employed databases.

Reference	Inner diameter (mm)	Superficial liquid velocity range (m/s)	Corresponding data range	Density ratio range	Surface tension range (N/m)
Current experiments		5.0	0.1, 0.4, and 0.8	Nitrogen-Water (0.2 and 0.4 MPa), nitrogen-95% aqueous ethanol solution (0.2 MPa), and HFC134a-water (0.7 MPa)	32–434 30.7–67.4

Table 4.1 (continued)

Sawant et al. [28]	9.4	0.05, 0.1, 0.15, 0.3, and 0.54	Air-Water 0.12, 0.4, and 0.58 MPa	147– 712	72.3
Wang et al. [21]	25.4	0.06, 0.15, 0.3, and 0.5	Air-water near atmospheric pressure	874	73.0
Fukano and Furukawa [3]	26	0.04, 0.06, and 0.1	Air-Water and 45 wt% Glycerol solution 0.1.3-0.117 MPa	786-876	72.0 and 65.0
Würtz [29]	10 and 20	0.06 – 2.49	Steam-Water 7 MPa	20	17.7

Table 4.2 Previous models of interfacial friction factor.

Reference	Correlation
Moeck [2]	$C_{fi} = 0.005 \left(1 + 1090 \frac{t_{Fave}^{1.42}}{D} \right)$
Fore et al. [4]	$C_{fi} = 0.005 \left[1 + 300 \left(1 + \frac{17500}{Re_G} \right) \frac{t_{Fave}}{D} - 0.0015 \right].$

Table 4.2 (continued)

Ju et al. [5]	$C_{fi} = 0.0028 + 4.28 We_L^{0.28} We_G''^{-0.53} N_{\mu L}^{0.25},$
Belt et al. [8]	$C_{fi} = 2 \left(1.158 \frac{t_{Fave}}{D} + 0.0003413 \right).$
Henstock and Hanratty [9]	$C_{fi} = C_{fs} (1 + 1400F), C_{fs} = \frac{0.046}{Re_G^{0.2}}, F = \frac{1}{\sqrt{2} Re_G^{0.4}} \frac{Re_L^{0.5} \mu_L \rho_G^{0.5}}{Re_G^{0.5} \mu_G \rho_L^{0.5}}, \text{ for } Re_L < 1000, Re_G > 1000; F = \frac{0.0379 Re_L^{0.9} \mu_L \rho_G^{0.5}}{Re_G^{0.9} \mu_G \rho_L^{0.5}}, \text{ for } Re_L > 1000, Re_G > 1000.$

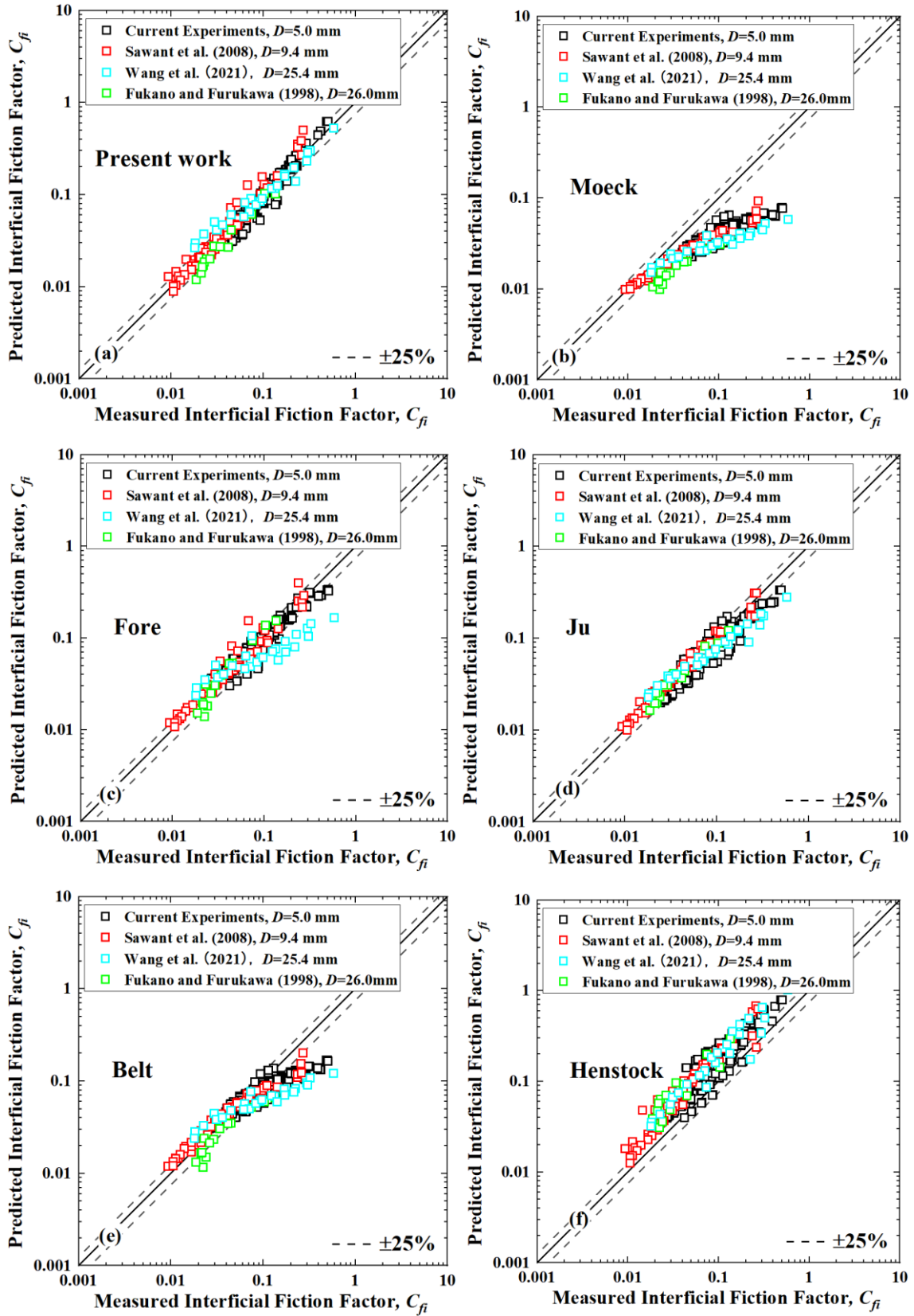


Fig. 4.8 Comparison of measured and predicted interfacial friction factor by correlations of (a) present work; (b) Moeck [2]; (c) Fore et al. [4]; (d) Ju et al. [5]; (e) Belt et al. [8]; (f) Henstock and Hanratty [9].

4.3.3 Pressure drop prediction

Substituting Eqs. (2.23), Eq. (4.5), and (4.12) into Eq. (4.4), the pressure gradient dP/dz can be roughly predicted by the following equation when considering the frictional pressure drop is the dominant component of the total pressure drop:

$$\frac{dp}{dz} = - \frac{2\rho_G j_G^2}{D(1-0.56Re_L^{-0.14}We_L^{0.25}We_G^{-0.36})(8.1 \ln[1.1+0.08Re_G^{0.11}We_L^{-0.24}We_G^{0.52}])^2}. \quad (4.13)$$

Conventionally, the frictional pressure drop of gas-liquid annular flow, is predicted by homogeneous and separated flow models. In the homogeneous flow model, the liquid and gas phases are assumed as a mixed single-phase flow with the same velocity. The density of the two-phase homogeneous flow is expressed as:

$$\rho_{TP} = \frac{1}{\left(\frac{x}{\rho_G} + \frac{1-x}{\rho_L}\right)}, \quad (4.14)$$

where x denotes the vapor quality. Then, the frictional pressure gradient of two-phase homogeneous flow model is given as:

$$-\left(\frac{dP}{dz}\right)_{TP} = \frac{2C_{fTP}G^2}{D\rho_{TP}}. \quad (4.15)$$

Here, G is the mass flux and C_{fTP} is the friction factor of the two-phase homogeneous flow which is expressed as:

$$C_{fTP} = \begin{cases} 16/Re_{TP}, & Re_{TP} < 2000 \\ 0.079Re_{TP}^{-0.25}, & 2000 \leq Re_{TP} < 20000. \\ 0.046Re_{TP}^{-0.2}, & Re_{TP} \geq 20000 \end{cases} \quad (4.16)$$

$$Re_{TP} = \frac{GD}{\mu_{TP}}. \quad (4.17)$$

To calculate the friction factor, the two-phase homogeneous viscosity, μ_{TP} , should be given appropriately to get the two-phase Reynolds number (Re_{TP}). In this work, two typical correlations for μ_{TP} [30,31] as summarized in the Table 4.4 are employed for comparison.

For the separated flow model, Lockhart-Martinelli method [32] is usually employed to predict the two-phase pressure drop. In this method, the two-phase pressure gradient can be obtained by single-phase flow pressure gradient of liquid phase $\left(\frac{dP}{dz}\right)_L$ and two-phase frictional multiplier of liquid phase ϕ_L as

$$\left(\frac{dP}{dz}\right)_{TP} = \phi_L^2 \left(\frac{dP}{dz}\right)_L. \quad (4.18)$$

The correlation by Chisholm [33] is employed to calculate the two-phase frictional multiplier as

$$\phi_L^2 = 1 + \frac{C}{X} + \frac{1}{X^2}. \quad (4.19)$$

where C is the Chisholm parameter to characterize the interaction effect between phases and X is the Lockhart-Martinelli multiplier defined as

$$X^2 = \left(\frac{dP}{dz}\right)_L / \left(\frac{dP}{dz}\right)_G. \quad (4.20)$$

$$-\left(\frac{dP}{dz}\right)_{L(G)} = \frac{2C_{fL(G)}\rho_{L(G)}j_{L(G)}^2}{D}. \quad (4.21)$$

Here, the single-phase friction factor of liquid and gas phase is obtained by Eq. (4.17) with the single-phase Reynolds number defined by Eq. (4.6). Correlations of C proposed by previous works by Sun and Mishima [34] and Kim and Mudawar [35] are employed in this work as summarized in Table 4.4.

Table 4.3 Previous correlations for predicting two-phase pressure drop.

Reference	Correlation
Homogeneous- Cicchitti et al. [30]	$\mu_{TP} = x\mu_G + (1-x)\mu_L.$
Homogeneous-Awad and Muzychka. [31]	$\mu_{TP} = \mu_G \frac{2\mu_G + \mu_L - 2(\mu_G - \mu_L)(1-x)}{2\mu_G + \mu_L + (\mu_G - \mu_L)(1-x)}.$

Table 4.3 (continued)

Sun and Mishima [34]	$C = 26 \left(1 + \frac{Re_L}{1000}\right) \left[1 - e^{\frac{-0.153}{0.27 \times La + 0.8}}\right] \text{ for } Re_L \text{ and } Re_G < 2000;$ $\phi_L^2 = 1 + \frac{C}{X^{1.19}} + \frac{1}{X^2}, C = 1.79 \left(\frac{Re_G}{Re_L}\right)^{0.4} \left(\frac{1-x}{x}\right)^{0.5} \text{ for } Re_L \geq 2000 \text{ or } Re_G \geq 2000, \text{ where } La = \frac{\sigma}{g(\rho_L - \rho_G)}.$
Kim and Mudawar [35]	$C = \begin{cases} 3.5 \times 10^{-5} Re_L^{0.44} Su_G^{0.5} (\rho_L/\rho_G)^{0.48}, & Re_L < 2000, Re_G < 2000 \\ 0.0015 Re_L^{0.59} Su_G^{0.19} (\rho_L/\rho_G)^{0.36}, & Re_L < 2000, Re_G \geq 2000 \\ 8.7 \times 10^{-4} Re_L^{0.17} Su_G^{0.5} (\rho_L/\rho_G)^{0.14}, & Re_L \geq 2000, Re_G < 2000 \\ 0.39 Re_L^{0.03} Su_G^{0.1} (\rho_L/\rho_G)^{0.35}, & Re_L \geq 2000, Re_G \geq 2000 \end{cases}$

In Fig. 4.9, I compare the pressure gradient prediction results by present model and previous models [30,31,34,35] employing databases of Wang et al.[21] and Würtz [29]. The adiabatic experiments conducted by Würtz are steam-water annular flow under 7 MPa and 286 °C which is similar with the experimental condition in BWRs. It is readily apparent that this model can provide

the best prediction with the error around 25% for most experimental data. The other correlations might provide good predictions for the Air-water annular flow, but the deviation becomes large when it comes to the steam-water annular flow under high pressure and temperature.

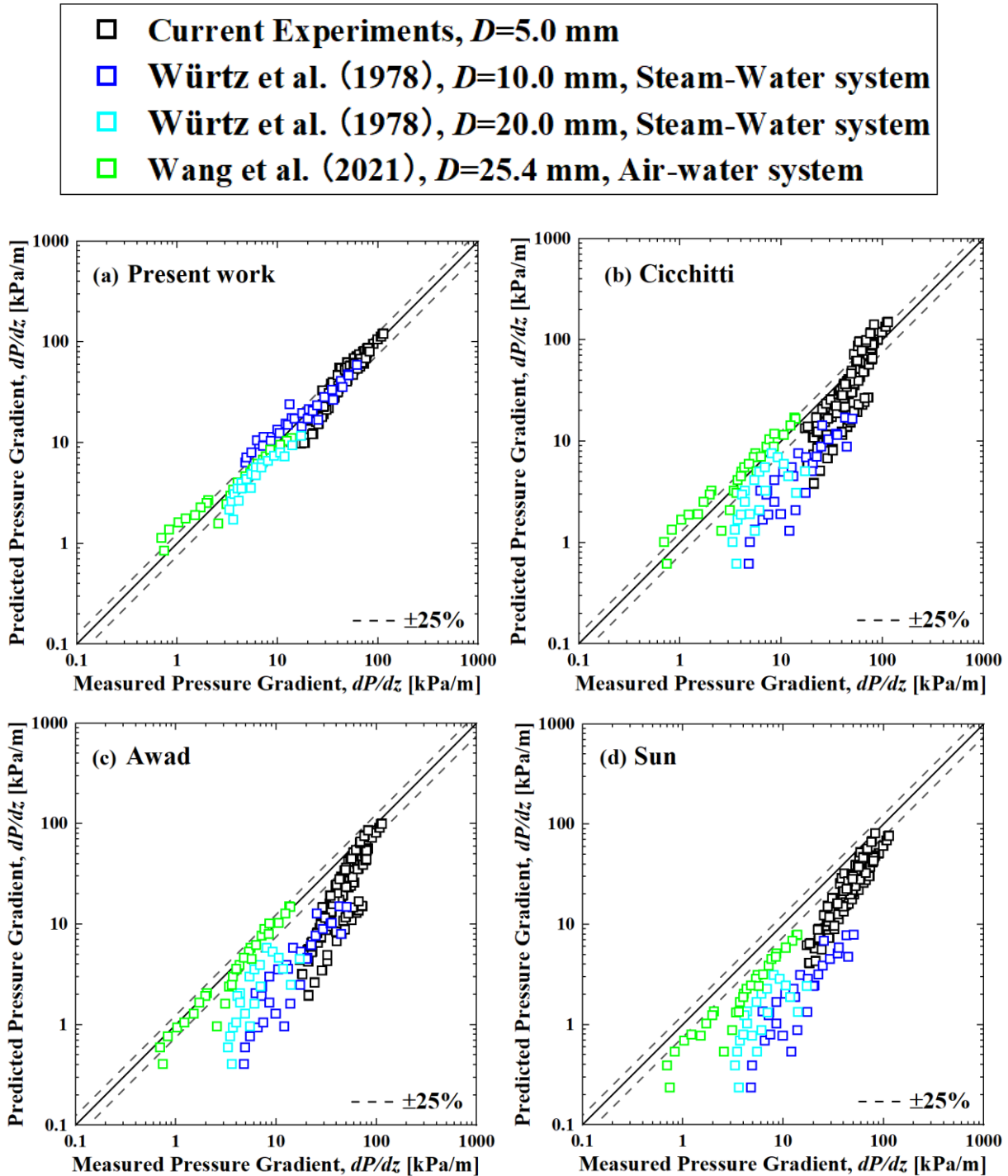


Fig. 4.9 Comparison of measured and predicted pressure gradient by correlations of (a) present work; (b) Cicchitti [30]; (c) Awad and Muzychka [31]; (d) Sun and Mishima [34]; (e) Kim and Mudwar [35].

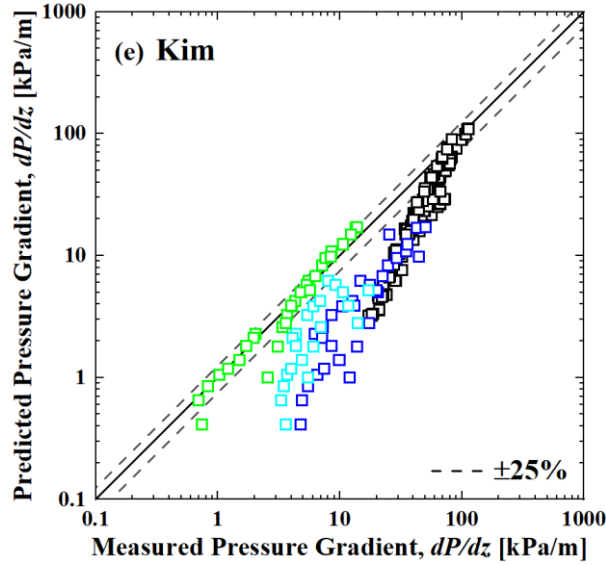


Fig. 4.9 (Continued)

4.4 Conclusion

Based on the upward annular flow experimental of Nitrogen-Water, HFC134a-Water, and Nitrogen-95% Ethanol systems, theoretical analysis on the interfacial shear stress is performed. Models are developed for predicting interfacial shear stress and pressure drop for the upward annular flow. The main conclusions are as follows:

- (1) Based on present experimental results, it is found that the interfacial shear stress increases with the decrease in density ratio and decreases with the decrease in the surface tension which could be attributed to the reduced interface roughness which is characterized as disturbance wave height.
- (2) It is confirmed by current experimental data that the equivalent sand-grain roughness, as employed in the Moody chart, is directly related with the wave height for the annular flow. A correlation is proposed in the form of Churchill equation for predicting interfacial friction factor and shows relatively good predictive performance. The proposed correlation is

$$\frac{1}{\sqrt{c_{fi}}} = 8.1 \ln[1.1 + 0.08Re_G^{0.11}We_L^{-0.24}We_G^{0.52}]. \quad (4.21)$$

- (3) A model is proposed to predict the pressure drop for upward annular flow. It is compared with some typical models and valuated by previous databases including steam-water annular flow under similar condition with BWR showing good prediction accuracy. The proposed correlation is

$$\frac{dp}{dz} = - \frac{2\rho_G j_G^2}{D(1-0.56Re_L^{-0.14}We_L^{0.25}We_G^{-0.36})(8.1 \ln[1.1+0.08Re_G^{0.11}We_L^{-0.24}We_G^{0.52}])^2}. \quad (4.22)$$

References

- [1] G.B. Wallis, One-dimensional two-phase flow, McGraw-Hill, New York, 1969.
- [2] E.O. Moeck, Annular-dispersed two-phase flow and critical heat flux, Canada, 1970. http://inis.iaea.org/search/search.aspx?orig_q=RN:01002083.
- [3] T. Fukano, T. Furukawa, Prediction of the effects of liquid viscosity on interfacial shear stress and frictional pressure drop in vertical upward gas–liquid annular flow, *Int. J. Multiph. Flow.* 24 (1998) 587–603. [https://doi.org/10.1016/S0301-9322\(97\)00070-0](https://doi.org/10.1016/S0301-9322(97)00070-0).
- [4] L.B. Fore, S.G. Beus, R.C. Bauer, Interfacial friction in gas–liquid annular flow: analogies to full and transition roughness, *Int. J. Multiph. Flow.* 26 (2000) 1755–1769. [https://doi.org/10.1016/S0301-9322\(99\)00114-7](https://doi.org/10.1016/S0301-9322(99)00114-7).
- [5] P. Ju, Y. Liu, C.S. Brooks, M. Ishii, Prediction of interfacial shear stress of vertical upward adiabatic annular flow in pipes, *Int. J. Heat Mass Transf.* 133 (2019) 500–509. <https://doi.org/10.1016/j.ijheatmasstransfer.2018.12.057>.
- [6] R.V.A. Oliemans, B.F.M. Pots, N. Trompé, Modelling of annular dispersed two-phase flow in vertical pipes, *Int. J. Multiph. Flow.* 12 (1986) 711–732. [https://doi.org/10.1016/0301-9322\(86\)90047-9](https://doi.org/10.1016/0301-9322(86)90047-9).
- [7] C.F. Colebrook, TURBULENT FLOW IN PIPES, WITH PARTICULAR REFERENCE TO THE TRANSITION REGION BETWEEN THE SMOOTH AND ROUGH PIPE LAWS., *J. Inst. Civ. Eng.* 11 (1939) 133–156. <https://doi.org/10.1680/ijoti.1939.14509>.
- [8] R.J. Belt, J.M.C. Van't Westende, L.M. Portela, Prediction of the interfacial shear-stress in vertical annular flow, *Int. J. Multiph. Flow.* 35 (2009) 689–697. <https://doi.org/10.1016/j.ijmultiphaseflow.2008.12.003>.
- [9] W.H. Henstock, T.J. Hanratty, The interfacial drag and the height of the wall layer in annular flows, *AIChE J.* 22 (1976) 990–1000. <https://doi.org/10.1002/aic.690220607>.
- [10] J.C. Asali, T.J. Hanratty, P. Andreussi, Interfacial drag and film height for vertical annular flow, *AIChE J.* 31 (1985) 895–902. <https://doi.org/10.1002/aic.690310604>.
- [11] M. Hajiloo, B.H. Chang, A.F. Mills, Interfacial shear in downward two-phase annular co-current flow, *Int. J. Multiph. Flow.* 27 (2001) 1095–1108. [https://doi.org/10.1016/S0301-9322\(00\)00065-3](https://doi.org/10.1016/S0301-9322(00)00065-3).
- [12] A.M. Aliyu, L. Lao, A.A. Almagbrok, H. Yeung, Interfacial shear in adiabatic downward gas/liquid co-current annular flow in pipes, *Exp. Therm. Fluid Sci.* 72 (2016) 75–87. <https://doi.org/10.1016/j.expthermflusci.2015.10.025>.

- [13] A.M. Aliyu, Y.D. Baba, L. Lao, H. Yeung, K.C. Kim, Interfacial friction in upward annular gas–liquid two-phase flow in pipes, *Exp. Therm. Fluid Sci.* 84 (2017) 90–109. <https://doi.org/10.1016/j.expthermflusci.2017.02.006>.
- [14] A. Cioncolini, J.R. Thome, C. Lombardi, Unified macro-to-microscale method to predict two-phase frictional pressure drops of annular flows, *Int. J. Multiph. Flow.* 35 (2009) 1138–1148. <https://doi.org/10.1016/j.ijmultiphaseflow.2009.07.005>.
- [15] A. Kawahara, M.H. Mansour, M. Sadatomi, W.Z. Law, H. Kurihara, H. Kusumaningsih, Characteristics of gas–liquid two-phase flows through a sudden contraction in rectangular microchannels, *Exp. Therm. Fluid Sci.* 66 (2015) 243–253. <https://doi.org/10.1016/j.expthermflusci.2015.03.030>.
- [16] T.S. Zhao, Q.C. Bi, Pressure drop characteristics of gas–liquid two-phase flow in vertical miniature triangular channels, *Int. J. Heat Mass Transf.* 44 (2001) 2523–2534. [https://doi.org/10.1016/S0017-9310\(00\)00282-9](https://doi.org/10.1016/S0017-9310(00)00282-9).
- [17] R. Goda, R. Kurimoto, K. Hayashi, M. Murase, A. Tomiyama, Effects of fluid properties on interfacial and wall friction factors under counter-current flow limitation in a vertical pipe with sharp-edged lower end, *Nucl. Eng. Des.* 373 (2021) 111020. <https://doi.org/10.1016/j.nucengdes.2020.111020>.
- [18] H. Zhang, S. Mori, T. Hisano, H. Yoshida, Effect of gas density and surface tension on liquid film thickness in vertical upward disturbance wave flow, *Int. J. Multiph. Flow.* 159 (2023) 104342. <https://doi.org/10.1016/j.ijmultiphaseflow.2022.104342>.
- [19] H. Zhang, Y. Umehara, H. Yoshida, S. Mori, On the velocity and frequency of disturbance waves in vertical annular flow with different surface tension and gas–liquid density ratio, *Int. J. Heat Mass Transf.* 211 (2023) 124253. <https://doi.org/10.1016/j.ijheatmasstransfer.2023.124253>.
- [20] D. Schubring, T.A. Shedd, E.T. Hurlburt, Planar laser-induced fluorescence (PLIF) measurements of liquid film thickness in annular flow. Part II: Analysis and comparison to models, *Int. J. Multiph. Flow.* 36 (2010) 825–835. <https://doi.org/10.1016/j.ijmultiphaseflow.2010.02.002>.
- [21] G. Wang, Z. Dang, M. Ishii, Wave structure and velocity in vertical upward annular two-phase flow, *Exp. Therm. Fluid Sci.* 120 (2021) 110205. <https://doi.org/10.1016/j.expthermflusci.2020.110205>.
- [22] P. Sawant, M. Ishii, M. Mori, Droplet entrainment correlation in vertical upward co-current annular two-phase flow, *Nucl. Eng. Des.* 238 (2008) 1342–1352. <https://doi.org/10.1016/j.nucengdes.2007.10.005>.
- [23] M. Ishii, K. Mishima, Correlation for liquid entrainment in annular two-phase flow of viscous

fluid, 1981. <https://doi.org/10.2172/12038509>.

- [24] Z. Wang, K.S. Gabriel, D.L. Manz, The influences of wave height on the interfacial friction in annular gas–liquid flow under normal and microgravity conditions, *Int. J. Multiph. Flow.* 30 (2004) 1193–1211. <https://doi.org/10.1016/j.ijmultiphaseflow.2004.06.003>.
- [25] C. Wang, N. Zhao, Y. Feng, H. Sun, L. Fang, Interfacial wave velocity of vertical gas-liquid annular flow at different system pressures, *Exp. Therm. Fluid Sci.* 92 (2018) 20–32. <https://doi.org/10.1016/j.expthermflusci.2017.09.007>.
- [26] S.W. Churchill, Friction-factor equation spans all fluid-flow regimes., *Chem. Eng. J.* 84 (1977) 91–92.
- [27] L.F. Moody, Friction Factors for Pipe Flow, *J. Fluids Eng.* 66 (1944) 671–678. <https://doi.org/10.1115/1.4018140>.
- [28] P.H. Sawant, Dynamics of annular two-phase flow, Ph Thesis. (2008).
- [29] J. Würtz, An experimental and theoretical investigation of annular steam-water flow in tubes and annuli at 30 to 90 bar, Risø National Laboratory Roskilde, 1978.
- [30] A. Cicchitti, C. Lombardi, M. Silvestri, Two-phase cooling experiments: pressure drop, heat transfer and burnout measurements., *Energ. Nucl.* 7 (1960) 417–425.
- [31] M.M. Awad, Y.S. Muzychka, Effective property models for homogeneous two-phase flows, *Exp. Therm. Fluid Sci.* 33 (2008) 106–113. <https://doi.org/10.1016/j.expthermflusci.2008.07.006>.
- [32] W. Lockhart, R.C. Martinelli, Proposed correlation of data for isothermal two-phase, two-component flow in pipes, *Chem. Eng. Prog.* 45 (1949) 39–48.
- [33] D. Chisholm, Pressure gradients due to friction during the flow of evaporating two-phase mixtures in smooth tubes and channels, *Int. J. Heat Mass Transf.* 16 (1973) 347–358. [https://doi.org/10.1016/0017-9310\(73\)90063-X](https://doi.org/10.1016/0017-9310(73)90063-X).
- [34] L. Sun, K. Mishima, Evaluation analysis of prediction methods for two-phase flow pressure drop in mini-channels, *Int. J. Multiph. Flow.* (2009). <https://doi.org/10.1016/j.ijmultiphaseflow.2008.08.003>.
- [35] S.-M. Kim, I. Mudawar, Universal approach to predicting two-phase frictional pressure drop for adiabatic and condensing mini/micro-channel flows, *Int. J. Heat Mass Transf.* 55 (2012) 3246–3261. <https://doi.org/10.1016/j.ijheatmasstransfer.2012.02.047>.

CHAPTER 5

Summary and prospect

The final chapter summarizes the research findings of all the above chapters and provides a prospect for future research. In the summary section, the effect of surface tension and liquid-gas density ratio and its analysis on the is introduced one by one. In the prospect section, a proposal, that simulating the steam-water annular flow in boiling water reactors, is proposed to reduce the investment cost of the experiments relating to the boiling water reactor operating.

5.1 Summary

The gas-liquid two-phase annular flow, such as the flow on the fuel rods of boiling water reactors, is a prevalent occurrence in industrial processes such as nuclear reactors, steam boilers, refrigeration system and many other gas-liquid involved applications in chemical industry. The annular flow is characterized by the presence of a liquid film attaching to the tube wall and high velocity gas phase flowing through the center of the tube. The liquid film interface is covered by disturbance waves and interval of these waves is very important because the dry patch always occurs at the base film between the two successive disturbance waves and the interfacial shear stress between gas and liquid phase is strongly linked to the gas-liquid interface structure. Therefore, knowledge of the liquid film and disturbance waves is of great importance for mass transport of liquid film, radial velocity distribution of liquid film, friction pressure drop, momentum transfer of two phases and heat- transfer characteristic of liquid film.

Although properties of the film thickness have been studied by numerous researchers, most of the experimental investigations available in the literature are limited to the near atmospheric condition while the density ratio and surface tension have limited variation. As a result, the effect of density ratio and surface tension on the annular flow characteristics could be not fully understood. In this work, I use the nitrogen gas and water under the system pressure of 0.2MPa and 0.4MPa, and in addition to those, HFC134a gas and water under the system pressure of 0.7MPa. Therefore, the density ratio can be changed from 32 to 434. By using 95% ethanol aqueous solution, the surface tension varies from 30.7 to 67.4 mN/m. Based on current experimental data, the effect of density ratio and surface tension on the liquid film thickness including base, average and maximum film thickness, and disturbance wave height is studied first. Then, the behavior of disturbance waves are investigated in details including

the velocity, wave length, intermittency, and frequency of the waves. Finally, I measured the pressure drop in the test section during two-phase flow experiments. The interfacial shear stress at the gas-liquid interface is obtained and studied. Multiple models for predicting the characteristics mentioned above are proposed, evaluated with previous databases and compared with previous models. The main achievements of the thesis are listed as follows.

1. It is found that the base film thickness, average film thickness, maximum film thickness, and wave height collapse onto a single curve when plotted with the gas Weber number under the same liquid flow rate condition. This could be interpreted by the fact that the gas Weber number includes the effect of drag force of the gas phase and the surface tension force, which codetermine the shape of the interface. Through employing current experimental data, a theoretical model is derived based on the Von Karman's universal velocity profile and Anderson's model with considering the droplet entrainment to predict the average film thickness. In addition, through the analytical investigation and multiple regression, another easy-to-use model expressed in terms of dimensionless numbers is proposed for the average film thickness prediction. Both models are evaluated by previous databases. Finally, it is found that, when plotted with gas Weber number, the average, base, and maximum film thicknesses are the same under the same gas Weber number and liquid flow rate regardless of density ratio and surface tension. Further data analysis of the disturbance wave height reveals that when wave height is plotted against a group of dimensionless numbers, $We_L^{-0.15}We_G^{0.45}$, the wave height tends to collapse onto a single curve even the experimental condition differs. Then, to estimate the disturbance wave height, I propose another simple theoretical model based on Ishii's study, which can explain the dependence of wave height on gas Weber number. Three previous databases are employed to evaluate the proposed model, and the model can predict the wave height satisfactorily within the error range.
2. In general, the wave velocity increases with the increase of superficial liquid velocity and superficial gas velocity and decreases as the surface tension decreases. However, when both superficial liquid velocity and superficial liquid velocity are low, the effect of surface tension is not obvious in the current experiments. Based on the universal velocity profile, the wave velocity can be expressed using the single and double profiles as introduced by Anderson under different experimental conditions analogy to the Couette flow for single-phase turbulent flow. Two wave velocity models based on the simple shear stress models on liquid film and gas-liquid interface are developed. After being evaluated by multiple previous databases and compared with previous models, the model proposed by this work show

satisfactory prediction performance ϵ with an error of about 20%. The wave pitch is found to decrease with the decrease of density ratio and weakly increase with decreasing surface tension. It is also shown that a unique relationship exists between wave pitch and wave height under the same flow condition. The disturbance wave wavelength is found to decrease with the increase of the density ratio. Under a low liquid flow rate, the wavelength also decreases as the surface tension increases while the effect of surface tension is indistinctive under a high liquid flow rate. The wave intermittency increases with the increase of density ratio, albeit the effect of surface tension is not obvious in current experiments. It is also found that the wave frequency increases with the increase of superficial gas velocity and superficial liquid velocity while it also increases with the decrease of density ratio and only slightly decreases with the decreasing surface tension. Generally, when wave velocity increases, the wavelength decreases, and the wave frequency increases. From the physical perspective, the wave frequency can be described based on the mass conservation between disturbance wave, base liquid film, and entrained droplets. Moreover, a new correlation is developed for the prediction of disturbance wave frequency in the form of gas Strouhal number. The new correlation can predict most of the data with an error of about 25%.

3. When it comes to the pressure drop and interfacial shear stress, it is found that the interfacial shear stress increases with the decrease in density ratio and decreases with the decrease in the surface tension which could be attributed to the reduced interface roughness as is characterized as disturbance wave height. It is confirmed by current experimental data that the equivalent sand-grain roughness, as employed in the Moody chart, is directly related with the wave height for the annular flow. A correlation is proposed in the form of Churchill equation for predicting interfacial friction factor and shows relatively good predictive performance. Then, a model is proposed to predict the pressure drop for upward annular flow. It is compared with some typical models and valuated by previous databases including steam-water annular flow under similar condition with BWR showing good prediction accuracy.

5.2 Prospect

The above results give the detailed information and explanations on the annular flow characteristics. However, the investigation on the effect of viscosity on these characteristics is still in demand and proposed correlations needs to be verified by the experiments under boiling water reactor condition. Therefore, the following recommendations for further works are suggested to advance

further on the achievement of this thesis:

1. This study has shown that the Anderson model [1] can predict the average liquid film thickness through the universal velocity profile [2] under the low liquid flow rate accurately. However, under the high liquid flow rate, the deviation of the prediction becomes larger. This could be attributed to the velocity profile becomes deviated when liquid flow rate increases. Attempts have been made to modify the velocity distribution in my experiments based on previous studies [3–6], however failed. Therefore, it is recommended to detect the actual velocity distribution using optical visualization such as particle imaging velocimetry (PIV) [3] and laser-induced fluorescence (LIF) [6]. Besides, based on my calculation, it is found that the velocity at the maximum film thickness is related to the universal velocity profile similar with Couette flow and divided into two profiles: single profile and double profile based on experimental condition. However, the criteria are still not clear. Therefore, more experiments are needed to find these criteria.
2. Expansion of experimental condition to cover and extend present experiments is strongly recommended. For example, the liquid viscosity can be altered by using glycerol solution and raising working liquid temperature. Steam-water annular flow under 7MPa is also recommended to perform for evaluating proposed correlations.
3. It is shown that the ratio of wave height and wave pitch is related to a dimensionless number group, $\frac{\rho_G Re_L}{\rho_L We_G}$. However, I believe there could be some physics beneath this phenomenon. The explanation of this relationship would be worthy of seeking. Besides, the intermittency also shows relating to the average film thickness and the explanation of this is also in need. The proposed correlation of intermittency also needed to be verified by databases, however, there are not many experimental data on intermittency and the measure methods are not the same.
4. It is observed by high-speed camera in my experiments that bubbles exist in the liquid film during experiments though its volume fraction is negligible. It is also found that the volume fraction of bubbles in liquid film would increase as liquid and gas flow rate increase. It is also found that volume fraction of bubbles is related to the volume fraction of ethanol when it comes to the ethanol aqueous solution. It is recommended to investigate the mechanism behind this.

References

- [1] G.H. Anderson, B.G. Mantzouranis, Two-phase (gas—liquid) flow phenomena—I Pressure drop and hold-up for two-phase flow in vertical tubes, *Chem. Eng. Sci.* 12 (1960) 109–126. [https://doi.org/10.1016/0009-2509\(60\)87004-2](https://doi.org/10.1016/0009-2509(60)87004-2).
- [2] Th. Von Kármán, The Analogy Between Fluid Friction and Heat Transfer, *J. Fluids Eng.* 61 (1939) 705–710. <https://doi.org/10.1115/1.4021298>.
- [3] A.C. Ashwood, S.J. Vanden Hogen, M.A. Rodarte, C.R. Kopplin, D.J. Rodríguez, E.T. Hurlburt, T.A. Shedd, A multiphase, micro-scale PIV measurement technique for liquid film velocity measurements in annular two-phase flow, *Int. J. Multiph. Flow.* 68 (2015) 27–39. <https://doi.org/10.1016/j.ijmultiphaseflow.2014.09.003>.
- [4] T.A. Shedd, Two-Phase Internal Flow: Toward a Theory of Everything, *Heat Transf. Eng.* 34 (2013) 420–433. <https://doi.org/10.1080/01457632.2012.721315>.
- [5] B.J. Cantwell, A universal velocity profile for smooth wall pipe flow, *J. Fluid Mech.* 878 (2019) 834–874. <https://doi.org/10.1017/jfm.2019.669>.
- [6] D.B. Hann, A.V. Cherdantsev, B.J. Azzopardi, Study of bubbles entrapped into a gas-sheared liquid film, *Int. J. Multiph. Flow.* 108 (2018) 181–201. <https://doi.org/10.1016/j.ijmultiphaseflow.2018.07.001>.

Acknowledgement

As Ph.D. graduation approaches, I decided to write acknowledgments to wrap up my dissertation. Over the past three years, many people have provided vital help and encouragement along the path of my doctoral research. Here, I will express my gratitude.

My supervisor, Professor Mori, provided me with the most help in both scientific research and life. The knowledgeable Prof. Mori strictly guided my research and paper writing with a rigorous scientific research attitude. During discussions on the research, Mori-sensei has always patiently introduces and explains the thoughts and ideas and respects my views as well. While I feel academic freedom, I am constantly discovering the truth in the process of debate. Prof. Mori also shows emphasis on the instructions on my writing and critical thinking. These trainings have helped me a lot in dealing with the details of other things. Prof. Mori also actively helped me with the problems I encountered during my research and in my life. In particular, when the experimental instrument was not working, he didn't hesitate to borrow another instrument from other lab and buy another one. Here, I would like to express my sincere gratitude to my supervisor, Prof. Mori, again. However, short words are still not enough to express my gratitude to him.

In addition, I would also like to thank Prof. Umehara for his help with my research. Prof. Umehara is always enthusiastic and supportive to help me with my problems during experiments and paper writing. He helped me buy instruments in the case I am poor in Japanese. He even helped me to review the research proposal and also provided key advice and assistance on my future career.

Special thank goes to the laboratory staffs, Mr. Eto and Ms. Yamashita. for their supportive roles in the laboratory. Without them, I could not conduct my experiments smoothly.

Special gratitude Prof. Takata for introducing me to my supervisor Prof. Mori and give me a chance to pursue my academic dream. I learn a lot when talking with Prof. Takata on the velocity profile and encouraged to work harder on the research.

I like to thank to Prof. Watanabe and Prof. Tsuda for letting me join their lab meeting and explaining their research to me in details. This benefit me a lot by increasing my knowledge on fluid dynamics including cavitation and molecular dynamics. I am also grateful Prof. Watanabe lend me the differential pressure transmitter which help me conducting me experiments successfully.

Next, I would also like to thank my family. During my Ph.D., I never had the opportunity to return to my nation to reunite with my parents because the COVID-19 continues to this day. Thanks for their concern and encouragement. Family is forever and I love them.

Finally, I like to express my sincere appreciation to Prof. Wang, Prof. Li, Prof. Kita, Prof. Shen for giving me valuable advices. I would also like to thank my friends: Wu Feifei, Wei Xuesong, Zhao

Junyu, Fu Yan, Chen Baichuan, Wu Zeyu, Wei Zuming and others. They provided help for my troubles in life and studying.

Appendix A. Circuit design of film thickness measurement sensor

Fig. A1 show the circuit diagram of each sensor. The liquid film in the annular flow is very thin and ranges from tens to hundreds of micrometers as measured in my experiments. Therefore, the electrical resistance of the liquid film between two electrodes of each sensor R_1 could be very high reaching the same order of the magnitude as that of the internal resistance of the oscilloscope, denoted as R_4 . To avoid excessively low output voltage, protect the oscilloscope, and minimize errors, the circuit as depicted in Fig. A1 is proposed. The resistance R_2 and R_3 are decided by the preliminary calculations based on the follow equations:

$$I = i_1 + i_2, \quad (\text{A.1})$$

$$i_2 = i_3 + i_4, \quad (\text{A.2})$$

$$i_2 R_2 + i_3 R_3 - i_1 R_1 = 0, \quad (\text{A.3})$$

$$i_4 R_4 - i_3 R_3 = 0. \quad (\text{A.4})$$

Here, i_1 , i_2 , i_3 , and i_4 are the current on R_1 , R_2 , R_3 , and R_4 and I is the current of the main circuit.

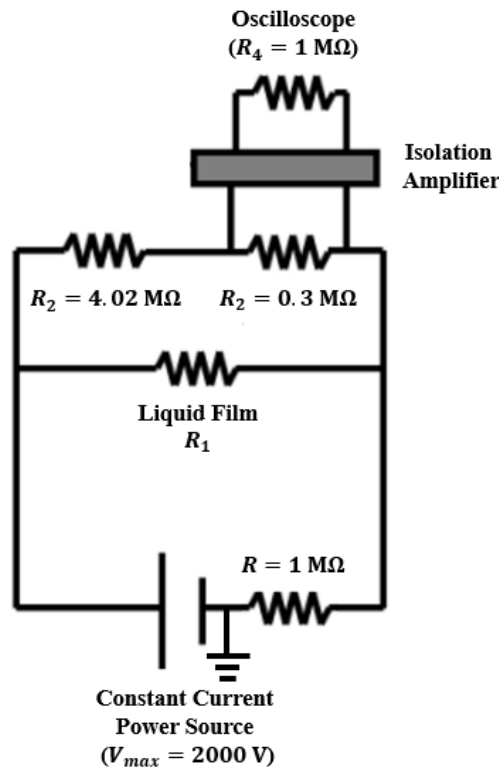


Fig. A1. Circuit diagram of each sensor.

To find the most appropriate electrical conductivity ρ , R_2 and R_3 , assumed values are given to liquid film thickness and calibration rod diameter. Then, the measured film thickness can be obtained by Eqs. (2.3), (A.1), (A.2), (A.3), and (A.4) whereas R_1 is calculated by Eq. (2.2). When the deviation between the assumed and measured film thickness becomes the smallest, ρ , R_2 and R_3 are decided.

Appendix B. Preparation of working fluids

In order to measure the voltage difference in the liquid film between two electrodes of each sensor and ensure that the voltage required by the circuit does not exceed the maximum voltage that the power supply can provide, it is necessary to add salt (e.g., sodium chloride) into the liquid to increase the electrical conductivity.

It is worth noting that, when making the 95% ethanol aqueous solution, the salt is added into the water firstly. Then the salt water is mixed with 99.5% ethanol. Considering the electrical conductivity of the liquid is very sensitive to the temperature, it is checked before each experiment. In this work, the electrical conductivity is set as 1000 $\mu\text{S}/\text{cm}$. The added salt is apparently 0.03-wt% for salt water and 0.8-wt% for 95% ethanol aqueous solution at the temperature of 20 °C.

Appendix C. Dynamic performance of the film thickness measurement sensors

As described in the section 2.2.4, the static calibration using the PTFE rod shows that the film thickness measurement sensors have a good static performance with an error around 5%. Considering the gas-liquid interface is rather wavy and local liquid film thickness may vary abruptly in the actual annular flow, the electric current density in the liquid film could be altered and not uniform. To check the dynamic performance of the film thickness measurement sensors, a rod with valleys and troughs is made by 3D printing as shown in Fig. C1.

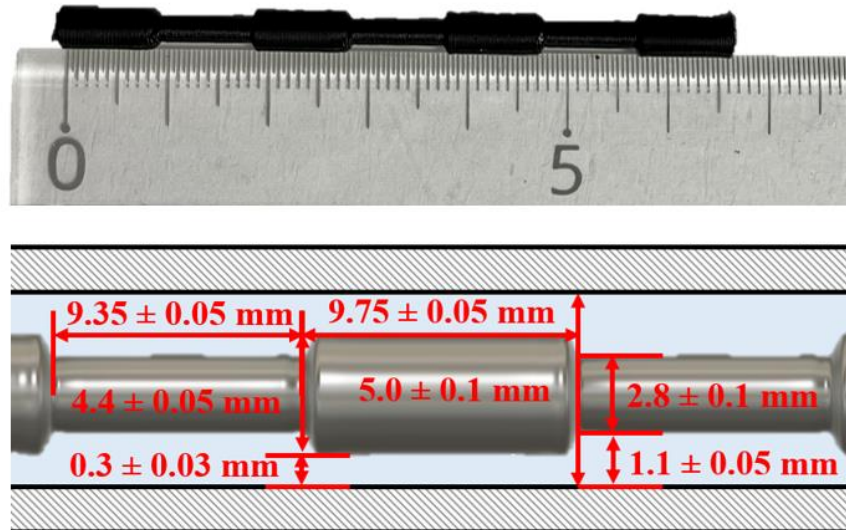


Fig. C1. Schematic illustration of printed calibration rod with dimensional information.

In the dynamic calibration, the printed rod is carried upward with water. The liquid film thickness when printed rod passing through the sensors is shown in Fig. C2. One example of the measured film thickness by S1 and S2 is plotted against the displacement of the printed rod as indicated by the red and black solid lines whereas the blue line indicates the actual size of the printed rod. It is readily apparent that the film thickness can be measured accurately. However, it is found that the maximum film thickness could be overestimated by 10% sometimes when repeating calibration. The accuracy of the wave pitch measurement is about 10% on average based on the calibration using the 3D-printed rod.

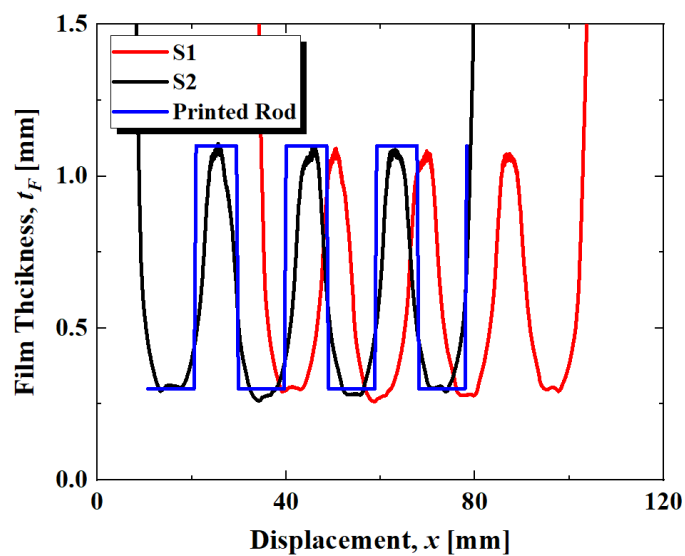


Fig. C2. Schematic illustration of printed calibration rod with dimensional information.

(別紙様式4)

承 諾 書

下記論文の全部または一部の内容を、Zhang Huacheng氏が学位論文のなかで使用することを承諾いたします。

また、私はその内容を学位申請用として使用する(した)こともありません。

記

1. Measurement of Liquid Film Thickness for Annular HFC134a Gas-Liquid Ethanol Flow in the Vertical Tube
Proceedings of 28th International Conference on Nuclear Engineering (ICONE-28), Vol. 4, 2021, ICONE28-63488. (令和3年8月)
共著者 Huacheng Zhang, Tutomu Hisano, Shoji Mori, Hiroyuki Yoshida.
2. Effect of gas density and surface tension on liquid film thickness in vertical upward disturbance wave flow
International Journal of Multiphase Flow, Vol.159, 2023, pp. 104342.
(令和4年12月)
共著者 Huacheng Zhang, Shoji Mori, Tutomu Hisano, Hiroyuki Yoshida.
3. On the velocity and frequency of disturbance waves in vertical annular flow with different surface tension and gas-liquid density ratio
International Journal of Heat and Mass Transfer, Vol.211, 2023, pp. 104342.
(令和5年4月)
共著者 Huacheng Zhang, Yutaro Umehara, Hiroyuki Yoshida, Shoji Mori.

以下、同じ

令和5年6月26日

共著者

森

昌司



(注) 本人が署名、押印のこと。

(別紙様式4)

承 諾 書

下記論文の全部または一部の内容を、Zhang Huacheng氏が学位論文のなかで使用することを承諾いたします。

また、私はその内容を学位申請用として使用する(した)こともありません。


記

1. Measurement of Liquid Film Thickness for Annular HFC134a Gas-Liquid Ethanol Flow in the Vertical Tube
Proceedings of 28th International Conference on Nuclear Engineering (ICONE-28), Vol. 4, 2021, ICONE28-63488. (令和3年8月)
共著者 Huacheng Zhang, Tutomu Hisano, Shoji Mori, Hiroyuki Yoshida.
2. Effect of gas density and surface tension on liquid film thickness in vertical upward disturbance wave flow
International Journal of Multiphase Flow, Vol.159, 2023, pp. 104342.
(令和4年12月)
共著者 Huacheng Zhang, Shoji Mori, Tutomu Hisano, Hiroyuki Yoshida.
3. On the velocity and frequency of disturbance waves in vertical annular flow with different surface tension and gas-liquid density ratio
International Journal of Heat and Mass Transfer, Vol.211, 2023, pp. 104342.
(令和5年4月)
共著者 Huacheng Zhang, Yutaro Umehara, Hiroyuki Yoshida, Shoji Mori.

以下、同じ

令和5年6月26日

共著者

吉田啓之 

(注) 本人が署名、押印のこと。

(別紙様式4)

承 諾 書

下記論文の全部または一部の内容を、Zhang Huacheng氏が学位論文のなかで使用することを承諾いたします。

また、私はその内容を学位申請用として使用する(した)こともありません。

記

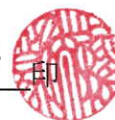
1. On the velocity and frequency of disturbance waves in vertical annular flow with different surface tension and gas-liquid density ratio
International Journal of Heat and Mass Transfer, Vol.211, 2023, pp. 104342.
(令和5年4月)
共著者 Huacheng Zhang, Yutaro Umehara, Hiroyuki Yoshida, Shoji Mori.

以下、同じ

令和5年6月26日

共著者

梅原 裕太郎



(注) 本人が署名、押印のこと。

(別紙様式4)

承 諾 書

下記論文の全部または一部の内容を、Zhang Huacheng氏が学位論文のなかで使用することを承諾いたします。

また、私はその内容を学位申請用として使用する(した)こともありません。

記

1. Measurement of Liquid Film Thickness for Annular HFC134a Gas-Liquid Ethanol Flow in the Vertical Tube
Proceedings of 28th International Conference on Nuclear Engineering (ICONE-28), Vol. 4, 2021, ICONE28-63488. (令和3年8月)
共著者 Huacheng Zhang, Tutomu Hisano, Shoji Mori, Hiroyuki Yoshida.
2. Effect of gas density and surface tension on liquid film thickness in vertical upward disturbance wave flow
International Journal of Multiphase Flow, Vol.159, 2023, pp. 104342.
(令和4年12月)
共著者 Huacheng Zhang, Shoji Mori, Tutomu Hisano, Hiroyuki Yoshida.

以下、同じ

令和5年6月26日

共著者

久野 裕 (印)

(注) 本人が署名、押印のこと。